SENSITIVITY ANALYSIS AND MULTI CONTRAST IMAGING OF MAGNETIC RESONANCE MAGNETOHYDRODYNAMIC FLOW VELOCIMETRY AT 3 TESLA

A THESIS SUBMITTED TO
THE GRADUATE SCHOOL OF NATURAL AND APPLIED SCIENCES
OF
MIDDLE EAST TECHNICAL UNIVERSITY

BY

MERT ŞİŞMAN

IN PARTIAL FULFILLMENT OF THE REQUIREMENTS
FOR
THE DEGREE OF MASTER OF SCIENCE
IN
ELECTRICAL AND ELECTRONICS ENGINEERING

JUNE 2021

Approval of the thesis:

SENSITIVITY ANALYSIS AND MULTI CONTRAST IMAGING OF MAGNETIC RESONANCE MAGNETOHYDRODYNAMIC FLOW VELOCIMETRY AT 3 TESLA

submitted by **MERT ŞİŞMAN** in partial fulfillment of the requirements for the degree of **Master of Science in Electrical and Electronics Engineering Department, Middle East Technical University** by,

Prof. Dr. Halil Kalıpçılar
Dean, Graduate School of **Natural and Applied Sciences** _____

Prof. Dr. İlkay Ulusoy
Head of Department, **Electrical and Electronics Engineering** _____

Prof. Dr. Murat Eyüboğlu
Supervisor, **Electrical and Electronics Engineering, METU** _____

Examining Committee Members:

Prof. Dr. Nevzat Güneri Gençer
Electrical and Electronics Engineering, METU _____

Prof. Dr. Murat Eyüboğlu
Electrical and Electronics Engineering, METU _____

Assoc. Prof. Dr. Yeşim Serinağaoğlu Doğrusöz
Electrical and Electronics Engineering, METU _____

Assoc. Prof. Dr. Elif Vural
Electrical and Electronics Engineering, METU _____

Prof. Dr. Ergin Atalar
Electrical and Electronics Engineering, Bilkent University _____

Date: 22.06.2021

I hereby declare that all information in this document has been obtained and presented in accordance with academic rules and ethical conduct. I also declare that, as required by these rules and conduct, I have fully cited and referenced all material and results that are not original to this work.

Name, Surname: Mert Şişman

Signature :

ABSTRACT

SENSITIVITY ANALYSIS AND MULTI CONTRAST IMAGING OF MAGNETIC RESONANCE MAGNETOHYDRODYNAMIC FLOW VELOCIMETRY AT 3 TESLA

Şişman, Mert
M.S., Department of Electrical and Electronics Engineering
Supervisor: Prof. Dr. Murat Eyüboğlu

June 2021, 111 pages

The magnetohydrodynamic (MHD) effect is a result of the interaction between orthogonal electric and magnetic fields in low viscosity media. Fluids inside such media start to form flow patterns in accordance with the Lorentz force density distributions caused by these orthogonal fields. In Magnetic Resonance Current Density Imaging (MRCDI) and Electrocardiogram (ECG) triggered Magnetic Resonance Imaging (MRI) applications, the MHD effect is observed and classified as artifacts that distort the measured signals. However, recently, the MHD flow velocity imaging is proposed as a novel imaging modality that may become an alternative to the blood oxygenation level-dependent functional Magnetic Resonance Imaging (fMRI). The aim of this thesis study is to realize MHD flow velocity imaging using a Spin Echo-based pulse sequence, to analyze the sensitivity of the obtained MHD flow velocity images on the current injection and MR image acquisition parameters, and to propose image acquisition and reconstruction techniques for multi-contrast imaging that contains MHD flow velocity imaging.

As the result of the MR experiments conducted with a cylindrical phantom, it is de-

termined that the magnitude of the MHD flow velocity distribution inside a homogeneous medium is increasing with the increasing area of the injected current pulse with an approximate power of 2.3. Moreover, it is observed that the MHD flow can reach higher velocity values in the horizontal flow direction than the vertical flow direction under the effect of the same current pulse because of the gravitational force. Lastly, with semi-analytical analyses of the relations between the SNR levels of the MHD flow velocity images and the parameters of the flow encoding gradients, it is derived that a b-value of 224 s/mm^2 is optimal for the water at room temperature.

Finally, a flow encoding gradient set is proposed for the simultaneous image acquisition of the imaging modalities MRCDI, Diffusion Tensor Imaging (DTI), and MHD flow velocity imaging. With the utilization of the proposed flow encoding gradient set, the data required for the reconstruction of all three contrast distributions can be collected with a total of 14 acquisitions. This provides a 50% decrease in the total image acquisition time in comparison with the separate acquisitions of all three imaging modalities. Furthermore, the proposed image acquisition technique is 100% efficient since all the acquired MR magnitude and phase images are utilized for the image reconstruction. The image reconstruction methods to obtain all three contrast distributions from the data acquired with the proposed multi-contrast imaging technique are also provided in this thesis. Finally, a numerical analysis is conducted in order to estimate the minimum required injected current amplitudes to obtain detectable MHD flow velocity signals. For the homogeneous cylindrical phantom and with the MR image acquisition parameters utilized during the sensitivity analysis, the minimum required current amplitude values are estimated as 1.43 mA and 1.94 mA for two different flow encoding gradient sets.

Keywords: magnetohydrodynamic flow velocity imaging, current density imaging, diffusion tensor imaging, multi-contrast imaging, sensitivity analysis

ÖZ

3 TESLADA MANYETİK REZONANS MANYETOHİDRODİNAMİK AKIŞ HIZI ÖLÇÜMÜNÜN DUYARLILIK ANALİZİ VE ÇOKLU KONTRAST GÖRÜNTÜLENMESİ

Şişman, Mert
Yüksek Lisans, Elektrik ve Elektronik Mühendisliği Bölümü
Tez Yöneticisi: Prof. Dr. Murat Eyüboğlu

Haziran 2021 , 111 sayfa

Manyetohidrodinamik (MHD) etki, düşük viskoziteli ortamlarda dikey elektrik ve manyetik alanlar arasındaki etkileşimin bir sonucudur. Bu tür ortamların içindeki sıvılar, bu dikey alanların neden olduğu Lorentz kuvvet yoğunluğu dağılımlarına göre akış hatları oluşturmaya başlar. Manyetik Rezonans Akım Yoğunluğu Görüntüleme (MRAYG) ve Elektrokardiyogram (EKG) tetiklemeli Manyetik Rezonans Görüntüleme (MRG) uygulamalarında, MHD etkisi gözlemlenmiş ve ölçülen sinyalleri bozan bir artefakt olarak sınıflandırılmıştır. Bununla birlikte, son zamanlarda, MHD akış hızı görüntülemesi, kan oksijenasyon seviyesine bağlı fonksiyonel Manyetik Rezonans Görüntülemeye (fMRG) bir alternatif olabilecek yeni bir görüntüleme yöntemi olarak önerilmiştir. Bu tez çalışmasının amacı, Dönüş Yankısı temelli bir darbe dizisi kullanarak MHD akış hızı görüntülemesini gerçekleştirmek, elde edilen MHD akış hızı görüntülerinin akım uygulama ve MR görüntü elde etme parametrelerine olan hassasiyetini analiz etmek ve MHD akış hızı görüntüleme yöntemini de içeren çoklu kontrast görüntüleme için edinim ve görüntü geriçatım teknikleri önermektir.

Silindirik bir fantom ile yapılan MR deneyleri sonucunda, homojen bir ortam içindeki MHD akış hızı dağılımının büyüklüğünün, uygulanan akım darbesinin lineer artan alanı ile yaklaşık 2.3'lük bir üstel kuvvetle arttığı tespit edilmiştir. Ayrıca yerçekimi kuvveti nedeniyle aynı akım darbesinin etkisi altında MHD akışının yatay akış yönünde düşey akış yönüne göre daha yüksek hız değerlerine ulaşabildiği görülmüştür. Son olarak, MHD akış hızı görüntülerinin SGO seviyeleri ile akış kodlama gradyanlarının parametreleri arasındaki ilişkilerin yarı analitik analizleri ile 224 s/mm^2'lik bir b-değerinin oda sıcaklığındaki su için optimal olduğu türetilmiştir.

Son olarak, "MRAYG", "Difüzyon Tensör Görüntüleme (DTG)" ve "MHD akış hızı görüntüleme" görüntüleme yöntemlerinin eş zamanlı edinimi için bir akış kodlama gradyan seti önerilmiştir. Önerilen akış kodlama gradyan setinin kullanılmasıyla, üç kontrast dağılımının tamamının yeniden yapılandırılması için gerekli veriler toplam 14 edinimle toplanabilir. Bu, üç görüntüleme yönteminin ayrı ayrı edinimlerine kıyasla toplam görüntü elde etme süresinde %50'lik bir azalma sağlar. Ayrıca, elde edilen tüm MR büyüklük ve faz görüntüleri görüntü geriçatımı için kullanıldığından, önerilen görüntü edinme tekniği %100 verimlidir. Önerilen çoklu kontrast görüntüleme tekniği ile elde edilen verilerden üç kontrast dağılımının tümünü elde etmek için kullanılan görüntü geriçatım yöntemleri de bu tezde sunulmuştur. Son olarak, saptanabilir MHD akış hızı sinyalleri elde etmek için uygulanması gereken en düşük akım genliklerini tahmin etmek için sayısal bir analiz gerçekleştirilmiştir. Homojen silindirik fantom için duyarlılık analizi sırasında kullanılan MR görüntü edinim parametreleri ile elde edilen gerekli en düşük akım genlik değerleri, iki farklı akış kodlama gradyan seti için 1,43 mA ve 1,94 mA olarak tahmin edilmiştir.

Anahtar Kelimeler: manyetohidrodinamik hız görüntüleme, akım yoğunluğu görüntüleme, difüzyon tensörü görüntüleme, çoklu kontrast görüntüleme, hassaslık analizi

To my mother

ACKNOWLEDGMENTS

I would like to express my deep gratitude to my supervisor Prof. Dr. Murat Eyüboğlu for his great guidance, encouragement, and support. I am thankful for his insightful critiques and advice during my studies.

I would like to thank Dr. Mehdi Sadighi for his huge contributions, friendship, and support during the whole process. It has been a great opportunity for me to work with him during my Master's studies since I learned a lot not just about technical issues but how to do research in general. He participated in all parts of the experiments. He also contributed to my thesis by discussing the results after each experiment. Without his valuable help and support, I could not finish this thesis.

I want to express my gratitude to my family and friends who were always there for me for their support and encouragement during this period.

I would also like to thank Dr. Hasan Hüseyin Eroğlu for his valuable guidance during my thesis study.

I would like to express my gratitude to Prof. Dr. Nevzat Güneri Gençer, Assoc. Prof. Dr. Yeşim Serinağaoğlu Doğrusöz, Assoc. Prof. Dr. Elif Vural, and Prof. Dr. Ergin Atalar for accepting to be a member of my thesis jury and evaluate my thesis.

I would like to thank my lab mate Berk Can Açıkgöz for his kindness and friendship.

Experimental data were acquired using the facilities of UMRAM (National Magnetic Resonance Research Center), Bilkent University, Ankara, Turkey. I want to thank UMRAM for providing this opportunity.

I have received a research scholarship from the Scientific and Technological Research Council of Turkey (TÜBİTAK) under Grant 116E157 by participating in the project work.

TABLE OF CONTENTS

LIST OF TABLES

TABLES

LIST OF FIGURES

FIGURES

LIST OF ABBREVIATIONS

2D	2 Dimensional
3D	3 Dimensional
AC	Alternating Current
BOLD	Blood Oxygenation Level-Dependent
BW	Bandwidth
CSF	Cerebrospinal Fluid
DC	Direct Current
DW	Diffusion-Weighted
DWI	Diffusion-Weighted Imaging
DTI	Diffusion Tensor Imaging
DT-MREIT	Diffusion Tensor - Magnetic Resonance Electrical Impedance Imaging
ECG	Electrocardiogram
EEG	Electroencephalography
EPI	Echo Planar Imaging
FE	Finite Element
FEM	Finite Element Model
fMRI	Functional Magnetic Resonance Imaging
FOV	Field of View
GE	Gradient Echo
ICNE	Injection Current Nonlinear Encoding
LEI	Lorentz Effect Imaging
MEG	Magnetoencephalography
MESE	Multi Echo Spin Echo

MHD	Magnetohydrodynamic
MR	Magnetic Resonance
MRCDI	Magnetic Resonance Current Density Imaging
MREIT	Magnetic Resonance Electrical Impedance Imaging
MRI	Magnetic Resonance Imaging
NMR	Nuclear Magnetic Resonance
SE	Spin Echo
SNR	Signal-to-Noise Ratio
SSFP-FID	Steady-State Free Precession Free Induction Decay
RF	Radio Frequency
RMS	Root Mean Square
RMSE	Root Mean Square Error
PCA	Principal Component Analysis
PET	Positron Emission Tomography
tACS	Transcranial Alternating Current Stimulation
tDCS	Transcranial Direct Current Stimulation
WM	White Matter

CHAPTER 1

INTRODUCTION

1.1 Motivation

Magnetohydrodynamic (MHD) flow is a phenomenon that takes place inside low viscosity media due to the interaction of the orthogonal electric and magnetic field distributions. For instance, during Magnetic Resonance Current Density Imaging (MRCDI) experiments, the electric field that the externally injected currents create and the static magnetic field of the MR scanner (B_0) produces a Lorentz force density distribution inside the medium. The ions inside the medium get affected by this force and start to form a flow. Consequently, these ions act as an internal mixer and make their solvent shells follow the flow as well [1]. The flow of water molecules that is caused by this process is called MHD flow.

In MRCDI, MHD flow is identified as an imaging artifact that distorts the obtained induced magnetic field distributions due to the externally injected currents (B_z). MHD flow is observed to cause phase shifts stemmed from the movement of water molecules. It was reported by Scott et al. [2] that these phase shift artifacts change sign with the changing polarity of injected currents. Hence, they assumed to be caused by the MHD flow. Furthermore, during an electrocardiogram (ECG) triggered Magnetic Resonance Imaging (MRI) scan, the flow of the electrically conductive blood interacts with B_0, and induces a voltage difference perpendicular to both B_0 and the blood flow direction. The induced voltage distorts the measured ECG signal by increasing the amplitude of the T-wave and inhibits the successful determination of R-peaks [3–5]. Especially, in ECG-triggered ultra-high field MRI, it is reported that the MHD effect significantly impacts the ECG signal [6].

In this thesis study, the MHD flow velocity distribution is considered as a unique contrast image which is a recent approach in the literature that has the potential to provide information about the flow of fluids inside the human body due to the induced Lorentz Force distributions during clinical applications of MRCDI and Magnetic Resonance Electrical Impedance Tomography (MREIT) [1, 7–10]. The measurement of the MHD flow velocity distribution is realized with a Spin Echo (SE)-based pulse sequence. The velocity distribution is encoded into the MR phase images using special gradients called flow encoding gradients.

To optimize the current injection and MR image acquisition parameters during the MHD flow velocity imaging, a semi-analytical sensitivity analysis is conducted. The dependency of the signal and noise levels of the MHD flow velocity images on the current injection parameters are determined empirically with the phantom experiments. Furthermore, the relations between the Signal-to-Noise Ratio (SNR) levels of the MHD flow velocity images and the parameters of the flow encoding gradients are derived analytically and optimal values are proposed. The mechanisms that each parameter affects the SNR level of the obtained images are explained. The work carried out in this section has the potential to form a baseline for future studies of the MHD flow velocity imaging.

In addition, to merge the image acquisition and reconstruction procedures of the imaging modalities MRCDI, DTI, and MHD flow velocity imaging, a flow encoding gradient set and image reconstruction procedures are proposed. In this way, a multi-contrast imaging scheme is constructed. Multi-contrast imaging provides multiple unique contrast images with a minimum number of image acquisition procedures by exploiting the similarities between the image acquisition procedures of different imaging modalities. For instance, both B_z and MHD flow velocity distributions are obtained from the data collected with external current injections. Similarly, during the data acquisition procedure of both DTI and MHD flow velocity imaging, motion-sensitizing gradients are utilized. By providing these multiple contrasts with the minimum image acquisitions, multi-contrast imaging has the potential to increase the clinical feasibility of these imaging modalities by decreasing the valuable acquisition time during MRI procedures. Moreover, each contrast image can be employed for separate clinical procedures since each of them originated from different physical

phenomena that provide unique information.

1.2 Magnetic Resonance Current Density Imaging

MRCDI is a novel imaging modality that provides cross-sectional current density ($\boldsymbol{J}$) distributions inside a conductor with nuclear magnetic resonance (NMR) active nuclei [11]. The externally injected current pulses are applied synchronously with an MRI pulse sequence to produce quasi-static magnetic fields. The components of the produced magnetic fields which are parallel to the B_0 are encoded into the MR phase images. MRCDI is applicable with both SE and gradient echo (GE)-based pulse sequences. Although SE-based pulse sequences are preferred for longer possible current injection durations and higher SNR values, GE-based sequences are also practical for shorter image acquisition times.

Knowledge of $\boldsymbol{J}$ is crucial in several medical applications such as transcranial direct current stimulation (tDCS) and transcranial alternating current stimulation (tACS) [12, 13] and source localization in electroencephalography (EEG) and magnetoencephalography (MEG) [14]. Moreover, the current density distribution is also required for algorithms such as MREIT and Diffusion Tensor-MREIT (DT-MREIT) that aim to obtain the conductivity distribution of the imaging object.

In the literature, there are numerous studies that provide a single, double, or all three components of the $\boldsymbol{J}$ distribution using direct current (DC), alternating current (AC), or radio frequency (RF) frequencies [2, 15–22]. One of the prior forms of these algorithms that provide all three components requires the imaging object to be rotated [2]. In this way, it is possible to obtain one orthogonal component of the induced magnetic field distribution which is the one parallel to B_0 in that orientation. After obtaining three components of the induced magnetic field distribution, it is possible to obtain the current density distribution via Ampere's law as:

$$\boldsymbol{J} = \frac{1}{\mu_0} \nabla \times \boldsymbol{B} \tag{1.1}$$

where μ_0 is the permeability of the free space and $\boldsymbol{B}$ is the induced magnetic field. This approach is impractical for clinical applications since it is almost always impossible to change the orientation of the patient during the imaging procedure.

To overcome this problem, Park et al. [23] proved that a two-dimensional current distribution can be uniquely determined using only a single component of the induced magnetic field (B_z). The projected current density ($\boldsymbol{J}_P$) distribution is the summation of two components: one of which is the current density distribution inside an object with homogeneous conductivity, identical geometry and boundary conditions, and the second component can be solved from the measured B_z. Moreover, it is shown that $\boldsymbol{J}_P$ provides a very good estimate of two-dimensional dominating current distribution (the orthogonal component is negligible) without accumulating noise effects in three-dimensional current densities.

In MRCDI, the distribution of the B_z is dependent solely on the injected current amplitude and the conductivity distribution of the domain. However, the current injection duration directly affects the SNR of the obtained B_z images. In order to achieve longer current injection durations, Park et al. [24] proposed the Injection Current Nonlinear Encoding (ICNE) method. With the ICNE, the current is injected during slice selection and phase encoding gradients. However, due to the induced magnetic fields, the linearity of the gradients is disturbed so a novel image reconstruction method instead of the standard inverse Fourier transform technique is proposed.

Later, Oh et al. [25] combined ICNE with a spoiled multi gradient echo sequence (SPMGE) to decrease total imaging time. This pulse sequence yielded an increase in the SNR of the acquired B_z images since it is possible to obtain B_z distribution multiple times and utilize a weighted averaging to enhance SNR. They provided optimal weights for this averaging procedure and utilized the standard inverse Fourier transform for image reconstruction since the current injection amplitudes employed in clinical applications are very low and the resulting distortion with standard image reconstructions is negligible most of the time.

Göksu et al. [26] conducted human in vivo brain MRCDI and demonstrated that it is possible to obtain qualified B_z images even with current injection with very low amplitudes such as 1 mA. Results obtained with multi echo spin echo (MESE) and steady-state free precession free induction decay (SSFP-FID) pulse sequences are presented. It is observed that the more efficient (timewise) SSFP-FID sequence is especially vulnerable to the magnetic stray fields that are caused by non-ideal placements

of the current injection cable and electrodes. A finite element (FE)-based method to correct the errors caused by these stray fields in B_z images is proposed and validated.

1.3 Diffusion Tensor Imaging

Water molecules make a random translational motion called Brownian motion even under no concentration gradient due to the thermal internal energy they possess. The principles of diffusion NMR are based on this motion mechanism. Under the effect of magnetic field gradients, this random motion of water molecules induces phase components in the NMR signal. Due to the randomness of the process, these phase shifts result in a phase dispersion in the transversal magnetization and, consequently, a decay in the magnitude of the acquired NMR signal [27, 28].

In the light of these observations, diffusion MRI techniques are proposed. The amount of the MR signal decay during diffusion MRI procedures is dependent on both the anatomical structure and the physiological state of the tissues. Utilizing special motion-sensitizing gradients called diffusion encoding gradients, these diffusion events can be encoded into magnitude images as local signal decays. The amount of the total diffusion and corresponding phase dispersion, and the parameters of the utilized diffusion encoding gradients determine the measure of the decay in the MR magnitude signal [29, 30]. The magnitude images obtained with this encoding mechanism are called diffusion-weighted (DW) images and the modality is called diffusion-weighted imaging (DWI). In DW images, the regions with unrestricted diffusion such as cerebrospinal fluid (CSF) appear darker, while the regions with restricted diffusion such as brain white matter (WM) appear brighter due to lower signal decay. DW images are utilized in the diagnostic processes of vascular strokes such as brain ischemia [31,32]. Moreover, it has the potential to replace Positron Emission Tomography (PET) for the diagnostics of non–small cell lung cancer since it has equal sensitivity or specificity [33].

DTI, on the other hand, is the imaging procedure of the space-dependent diffusion coefficient, or the diffusion tensor for anisotropic media, distributions of the imaging region using the DW images. In diffusion tensor images, the isotropic regions

where unrestricted diffusion exists, such as CSF, appear brighter since higher diffusion values are obtained in those regions. On the other hand, the anisotropic regions where restricted diffusion exists, such as brain WM, appear darker since lower diffusion values are obtained. In order to obtain the six independent elements of the diffusion tensor in each voxel, it is required to acquire six DW images with different diffusion encoding directions. Moreover, a T_2-weighted image is also required as a baseline distribution where no signal decay due to diffusion is observed. DTI is most commonly utilized for the imaging of highly anisotropic regions such as brain WM that contains fiber bundles and myelin sheaths that strongly restrict the diffusion directions [30, 34]. Furthermore, DTI is employed during brain connectivity studies as a quantitative analysis method for brain fiber tracking [34]. In clinics, DTI is utilized for the detection of neurodegenerative diseases such as Alzheimer's disease [35] and psychiatric disorders such as schizophrenia [36].

1.4 Magnetohydrodynamic Flow Velocity Imaging

As mentioned before, with the interaction of orthogonal electric and magnetic fields, the Lorentz force density distribution is formed inside a medium. In 2008, Truong et al. [37] proposed an imaging modality called Lorentz Effect Imaging (LEI), as an alternate to the blood oxygenation level-dependent (BOLD) functional MRI (fMRI), by increasing the signal detectability. LEI is claimed to be able to detect spatially incoherent but temporally synchronized electrical activity under the effect of a strong magnetic field. The proposed method was to acquire magnitude images via a GE-based pulse sequence with oscillating phase and frequency gradients and synchronous external current injection. Moreover, they prepared numerical simulations of their LEI model to compare with the experimental results. They conducted phantom experiments with a 4T MR scanner and external current injection with levels of 1-5 mA. The experimental results of the phantoms with ionic solutions that contain copper and sulfate ions showed significant decay in the magnitude signal. The signal decay patterns showed consistency with the simulation results of the developed LEI model. However, in 2010, Wijesinghe et al. [38] claimed that the results presented by Truong et al. are not correct due to the utilization of incorrect ionic mobility values in the

proposed LEI model. Wijesinghe et al. argued that with the incorrect ionic mobility values Truong et al. used, the magnetic part of the Lorentz force density distribution is overestimated by more than a factor of a million. Hence, they concluded that it is not possible to detect Lorentz force distributions induced by nerve conduction. Moreover, they pointed out that the observed signal decay in the experimental results shown by Truong et al. may be caused by the MHD flow of the conductive fluids. Finally, in 2013, Pourtaheri [39] et al. improved the LEI model proposed by Truong et al. and showed that the main contrast mechanism in the LEI phantom experiments is the MHD flow by comparing the signal loss patterns of the experimental results of Truong et al. with the simulation results of their new model.

In 2015, Balasubramanian et al. [7] conducted phantom experiments to examine the effect of the MHD flow on both the magnitude and phase images. They utilized a GE-based echo planar imaging (EPI) pulse sequence without any flow encoding gradients on a 3T MR scanner. The experimental phantom is composed of a plastic bottle and capillary tubes that are filled with a saline solution. The current pulse is injected into the medium via chloridized silver electrodes and the capillary tubes. 600 consecutive images are acquired in 450 s. The current pulse with 60 μA is injected constantly during the middle 150 ms time interval. They observed phase components that change sign with the changing polarity of both the injection current and the imaging gradients. Moreover, they showed that the dynamic range of these phase shifts is greater than the expected phase accumulation due to B_z as well. Therefore, they concluded that the MRI phase is sensitive to the fluid flow even without flow encoding gradients and the MHD flow due to such low current injection levels is able to create detectable phase components. Besides, they reported that the observed contrast in the phase images is far greater than the observed contrast in the magnitude images. As the final remark of their study, Balasubramanian et al. proposed that MHD-driven CSF flow may be utilized as a novel fMRI contrast mechanism. They argued that this technique may become useful for the presurgical evaluation of epilepsy patients.

In 2019, Minhas et al. [8] evaluated the MHD flow effects during MREIT experiments on an 18.8T MR scanner via phantom experiments. They utilized an SE-based pulse sequence with flow encoding gradients and bipolar current injection. The cylindrical phantoms had 7.2 mm diameter and 10 mm height. Two phantoms were filled with

gelatin and artificial sea water. The injected current pulses had an amplitude of 200 μA. They observed apparent phase components due to the MHD flow in the phantom with artificial sea water filling but not in the phantom with gelatin filling due to the difference in the viscosity. They concluded that the phase components produced by the MHD flow dominates the phase images at high magnetic field strengths, and consequently, distort the B_z images. Hence, during high field MREIT, the MHD flow effects should be carefully addressed. They argued that further exploration of the MHD effects in MREIT experiments should be conducted with experimental phantoms of different sizes and shapes, and the following optimization of pulse sequences and sequence parameters has the potential to increase clinical applicability of the MREIT.

Later, in 2019, Eroğlu et al. [9] developed a multi-physics model to image the MHD flow inside the ionic solutions. They conducted physical experiments on a 3T MR scanner with a conventional spoiled GE pulse sequence that contains bipolar flow encoding gradients. They injected currents with levels 1-40 mA into a square experimental phantom. They observed that even with 1 mA current injection level, 1.5 radian phase is accumulated for 30 ms current injection duration and 24 mT/m flow encoding gradient amplitude. They also prepared an FE-based simulation model to predict the distribution of the MHD-based phase components using electrical currents, laminar flow, and MRI equations. The contrast distributions of the simulation and experimental results showed significant consistency, hence, they concluded that the MHD-based phase distributions can successfully be imaged using the proposed method. They argued that the proposed imaging modality can be employed during electrical current-based neuromodulation studies to examine CSF flow. Furthermore, in [10], Eroğlu et al. also proposed an SE-based pulse sequence with flow encoding gradients and unipolar current injection to obtain MHD flow velocity distributions and presented simulation results.

In 2020, Benders et al. [1], evaluated the effect of the MHD flow during in-situ electrochemical reactions using MRI. They utilized an SE-based velocity imaging pulse sequence on an 11.7T MRI scanner. They injected currents with the level of 75 mA into a $10\times10\times45$ mm^3 electrochemical cell using copper plates. They observed significant velocity components in the medium and concluded that these components

result from the Lorentz force created by the interaction of B_0 and the injected currents. They argued that the MHD flow induced by the Lorentz Force can be utilized to accelerate electrochemical reactions.

In this thesis study, phantom experiments are conducted on a 3T MR scanner using an SE-based pulse sequence with flow encoding gradients and unipolar current injections with different phantom geometries. The effect of different current injection schemes and patterns are evaluated. A semi-analytical sensitivity analysis is done to obtain and optimize the relations between the current injection and MR image acquisition parameters and the SNR levels of the acquired MHD flow velocity images. Finally, the amplitude of the current injection levels required to obtain detectable MHD flow signals is provided.

1.5 Multi-Contrast Imaging

In the literature, there are several studies that combine the image acquisition and reconstruction procedures of the MRCDI and MREIT. For instance, one of the most famous MREIT algorithms, i.e. harmonic B_z algorithm, is based on the iterative or simultaneous solution of the current density and isotropic conductivity distributions of the imaging slice using the measured B_z distribution [40–43]. Furthermore, the projected current density algorithm proposed by Park et al. [23] also provides the isotropic conductivity distribution as well. In 2010, Nam et al. [44] proposed an algorithm that combines the harmonic B_z and the projected current density algorithms to reconstruct the anisotropic conductivity distributions of the medium.

In addition, DT-MREIT is an imaging modality that utilizes the diffusion tensor and the current density distributions of the medium to reconstruct the anisotropic conductivity tensor distribution [45, 46]. Its clinical applicability is shown by the canine and human brain in vivo experiments [47,48]. In 2021, Sadighi et al. [49] proposed a total variation-based inverse problem solution approach to decrease the required number of the current injection patterns to one during DT-MREIT to decrease the total data acquisition time and increase patient comfort. The simultaneous data acquisition of the diffusion tensor and B_z distributions using a single pulse sequence is also pro-

posed by Sadighi et al. [50] which enhances the performance of the DT-MREIT by decreasing the total acquisition time even further.

As mentioned before the data acquisition procedures of the B_z and MHD flow velocity distributions are quite similar since externally injected currents are utilized to trigger the events that will be encoded into the phase images by the MRI pulse sequences. Moreover, during the data acquisition procedures of both diffusion tensor and MHD flow velocity distributions, motion-sensitizing gradients are employed. Hence, the combination of the data acquisition procedures of these three imaging modalities is reasonable.

In this thesis study, a flow encoding gradient set is proposed to merge the data acquisition procedure of the MRCDI, DTI, and MHD flow velocity imaging. Besides, image reconstruction algorithms of each contrast image from the simultaneously acquired data are provided.

1.6 The Outline of the Thesis

In this thesis study, the conducted work can be classified into three sub-topics: The realization of the MHD flow velocimetry using an SE-based pulse sequence with flow encoding gradients and external current injection, the MHD flow velocity imaging sensitivity analysis, and the multi-contrast imaging of the MRCDI, DTI, and MHD flow velocity imaging.

In Chapter 2, the theory and the mathematical derivations of the proposed methods and conducted analyses are presented. These include the evaluation and comparison of the effects of different current injection schemes and patterns, semi-analytical analysis of the sensitivity of the SNR of the MHD flow velocity images on the current injection and MR image acquisition parameters, and image reconstruction methods of the mentioned multi-contrast imaging modalities.

The simulation model and the experimental phantoms, the current injection and MR image acquisition parameters utilized during MRI experiments, the MRI system, and the single and double current pulse schemes are demonstrated in Chapter 3.

Chapter 4 presents the results obtained from the numerical simulation and the MRI experiments, the mathematical analyses based on the obtained results, and the corresponding discussions.

Finally, in Chapter 5, the conclusion of the thesis study is provided.

In this thesis, vectors are denoted by lowercase or uppercase bold letters (e.g. $\boldsymbol{v}$ or $\boldsymbol{J}$), and matrices are denoted by double over lined uppercase letters (e.g. $\overline{\overline{D}}$).

CHAPTER 2

THEORY AND THE MATHEMATICAL DERIVATIONS OF THE PROPOSED MHD FLOW VELOCITY IMAGING METHODS AND CONDUCTED ANALYSES

2.1 Introduction

In this section, the theory and the mathematical derivations of the proposed image reconstruction methods and conducted analyses are given in detail. Section 2.2 provides the MHD flow velocity measurement technique using MRI. The relation between the MHD flow velocity distribution and the MR phase image obtained via an SE-based pulse sequence is derived. In Section 2.3, an analysis related to the sensitivity of the SNR of the MHD flow velocity images on different MR image acquisition and current injection parameters is conducted. In Figure 2.1, an SE-based pulse sequence with both flow encoding gradients and synchronous current injection pulse is shown that can be utilized for the multi-contrast imaging that includes MHD flow velocity imaging. The image reconstruction methodologies for the current density, diffusion tensor, and MHD flow velocity images using data collected with a single pulse sequence during multi-contrast imaging are derived and given in Section 2.4.

2.2 MHD Flow Velocimetry

In a generic SE experiment without flow encoding and current injection, the MR signal measured can be expressed as:

$$S_0(t,k_x,k_y) = \iiint_V M_0(1-e^{-\frac{T_R}{T_1}})e^{-\frac{T_E}{T_2}}e^{-j\gamma B_0 t}e^{j\phi_0}e^{-j\gamma(k_x x+k_y y)}dV \qquad (2.1)$$

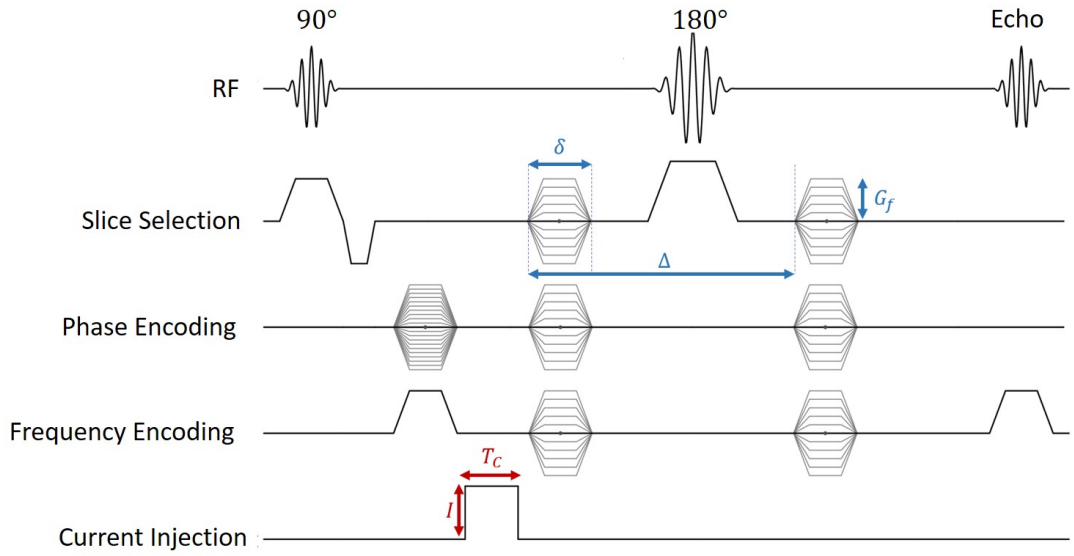

Figure 2.1: An SE-based pulse sequence with both flow encoding gradients and synchronous current injection pulse. δ, Δ, and G_f are the duration, the period and the magnitude of the flow encoding gradients, respectively. Moreover, I and T_C are the strength and the duration of the injected current pulses.

where B_0 is the magnitude of the static magnetic field of the MR scanner, M_0 is the magnitude of the equilibrium bulk magnetization of the proton spins under the effect of B_0 and is proportional to the proton spin density, T_E is echo time, T_R is pulse repetition time and V is the imaged domain. T_1 and T_2 are longitudinal and transverse relaxation time constants of the medium. k_x and k_y are the spatial frequency variables in the x- and y-directions. ϕ_0 is the systematic phase artifact of the MRI scanner including the effects of the RF pulse and the imaging gradients. After demodulating the signal with Larmor frequency, and applying inverse Fourier transform, the space domain signal can be expressed as:

$$S_0(t,x,y) = M_0(1 - e^{-\frac{T_R}{T_1}})e^{-\frac{T_E}{T_2}}e^{j\phi_0} \tag{2.2}$$

If motion-sensitizing (flow or diffusion encoding) gradients are applied, the measured signal can be expressed as [27]:

$$S_k = S_0 e^{-b\boldsymbol{g}_f^{k\,T}\overline{\overline{D}}\boldsymbol{g}_f^k} e^{j\phi_{\boldsymbol{g}_f^k}} \quad for \;\; k = 1, 2, ..., N \tag{2.3}$$

where $\boldsymbol{g}_f^k$ is a 3D unit vector which determines the flow encoding direction and N is the number of the linearly independent diffusion encoding directions. $\phi_{\boldsymbol{g}_f^k}$ is the phase component due to presence of the flow encoding gradients. $\overline{\overline{D}}$ is the diffusion tensor of the domain and b is the b-value which is a tuning parameter that determines the amount of signal decay due to the effective diffusion in the medium and can be computed as [34]:

$$b = \gamma^2 G_f^2 \delta^2 (\Delta - \frac{\delta}{3}) \tag{2.4}$$

where G_f is the magnitude of flow encoding gradients, Δ and δ are specific time intervals in the pulse sequence. All of them are shown in Figure 2.1. Choosing larger b-values increases the diffusion weighting on the flow encoded images (S_k) and consequently decreases the measured MR signal magnitude.

On the other hand, if a current pulse is also injected along with the flow encoding gradients, some additional phase terms are also added to the signal [9]. However, magnitude does not get affected [28]. The new signal can be expressed as:

$$S_k = S_0 e^{-b\boldsymbol{g}_f^{k\,T}\overline{\overline{D}}\boldsymbol{g}_f^k} e^{j\left(\phi_0+\phi_I+\phi_{\boldsymbol{g}_f^k}+\phi_{MHD,\,\boldsymbol{g}_f^k}+\phi_{MHD,\,\boldsymbol{g}_{img}}\right)} \text{ for } k = 1, 2, ..., N \tag{2.5}$$

where ϕ_I is the accumulated phase component due to the injected current. $\phi_{MHD,\,\boldsymbol{g}_f^k}$ and $\phi_{MHD,\,\boldsymbol{g}_{img}}$ are the phase components created by the MHD flow. $\phi_{MHD,\,\boldsymbol{g}_f^k}$ is encoded by the flow encoding gradients and $\phi_{MHD,\,\boldsymbol{g}_{img}}$ is encoded by the imaging gradients.

MHD flow is a physical phenomenon that occurs due to the Lorentz force density distribution that is formed by the interaction of the static magnetic field of the MR scanner and the injected current. The ions and consequently the water molecules start to move according to this force and the velocity distribution created satisfies Navier – Stokes equations in the form [9]:

$$\rho(\frac{\partial \boldsymbol{v}}{\partial t} + \boldsymbol{v} \cdot \nabla \boldsymbol{v}) = \nabla p + \mu \nabla^2 \boldsymbol{v} + \boldsymbol{F}_L \tag{2.6}$$

and

$$\nabla \cdot \boldsymbol{v} = 0 \tag{2.7}$$

where $\boldsymbol{v}$ is the MHD flow velocity, ρ is the density of the fluid, p is the pressure field of the domain, μ is the dynamic viscosity and $\boldsymbol{F}_L$ is the above-mentioned Lorentz

force in the form:

$$\boldsymbol{F}_L = \sigma(\boldsymbol{E} + \boldsymbol{v} \times B_0\boldsymbol{k}) \times B_0\boldsymbol{k} \tag{2.8}$$

Note that $\boldsymbol{k}$ in (2.8) is the unit vector in the z-direction. The nonzero phase ($\phi_{MHD,\,\boldsymbol{g}_f^k}$) formed due to the MHD phenomenon and encoded by the flow encoding gradients can be extracted if 4 different SE experiments are conducted with changing flow encoding gradient and current polarities [9].

Note that the phase of distribution in (2.5) contains:

$$arg(S) = \phi_0 + \phi_I + \phi_{\boldsymbol{g}_f^k} + \phi_{MHD,\,\boldsymbol{g}_f^k} + \phi_{MHD,\,\boldsymbol{g}_{img}} \tag{2.9}$$

$\phi_{MHD,\,\boldsymbol{g}_f^k}$ can be obtained as [9]:

$$\phi_{MHD,\,\boldsymbol{g}_f^k} = \frac{arg(S^{I_+\boldsymbol{g}_{f+}^k}) - arg(S^{I_-\boldsymbol{g}_{f+}^k}) - arg(S^{I_+\boldsymbol{g}_{f-}^k}) + arg(S^{I_-\boldsymbol{g}_{f-}^k})}{4} \tag{2.10}$$

$S^{I_\pm\boldsymbol{g}_{f\pm}^k}$ are space signal distributions obtained using the opposing flow encoding gradient and current injection polarities.

The relation between $\phi_{MHD,\,\boldsymbol{g}_f^k}$ and $\boldsymbol{v}$ can be derived as:

$$\phi_{MHD,\,\boldsymbol{g}_f^k} = -\int_{t_0}^{t_0+\delta} \gamma G_f(\boldsymbol{g}_f^k \cdot \boldsymbol{v})tdt + \int_{t_0+\Delta}^{t_0+\Delta+\delta} \gamma G_f(\boldsymbol{g}_f^k \cdot \boldsymbol{v})tdt = \gamma G_f \delta\Delta(\boldsymbol{g}_f^k \cdot \boldsymbol{v}) \tag{2.11}$$

where t_0 is the time instant that the first flow encoding gradient pulse is applied.

Hence, the component of $\boldsymbol{v}$ in the direction of $\boldsymbol{g}_f^k$ can simply be computed as:

$$\boldsymbol{g}_f^k \cdot \boldsymbol{v} = \frac{\phi_{MHD,\,\boldsymbol{g}_f^k}}{\gamma G_f \delta\Delta} \tag{2.12}$$

Note that MHD flow velocity imaging is based on MR phase images, hence, phase unwrapping is required as an initial step before the MHD flow velocity reconstruction. The quality-guided phase unwrapping method [51] is utilized in this thesis study for this purpose.

2.3 MHD Flow Sensitivity Analysis

2.3.1 Analytical Derivation of the SNR Equation of the MHD Flow Velocity Images

As mentioned, the MHD flow velocity distributions are obtained via phase images. Scott et al. [16] showed that the noise level (standard deviation of the noise distribution, σ_{n_ϕ}) of the phase images are proportional to the SNR of the magnitude images (SNR_M) as:

$$\sigma_{n_\phi} \approx (\sqrt{2} SNR_M)^{-1} \tag{2.13}$$

with high SNR_M assumption (within an error margin of 4% for $SNR_M > 2.8$).

It is well-known that the MR signal magnitude, consequently SNR_M, is proportional for SE-based pulse sequences to:

$$SNR_M \sim M_0(1 - e^{-\frac{T_R}{T_1}})e^{-\frac{T_E}{T_2}} \tag{2.14}$$

Moreover, as seen in (2.3), the MR magnitude signal is also affected by the diffusion when flow encoding gradients are applied as:

$$SNR_M \sim M_0(1 - e^{-\frac{T_R}{T_1}})e^{-\frac{T_E}{T_2}} e^{b\boldsymbol{g}_f^{k\,T}\overline{\overline{D}}\boldsymbol{g}_f^k} \tag{2.15}$$

Since $\phi_{MHD,\,\boldsymbol{g}_f^k}$ is obtained averaging 4 phase images, the noise level of the $\phi_{MHD,\,\boldsymbol{g}_f^k}$ ($\sigma_{n_{\phi,MHD}}$) is proportional to:

$$\sigma_{n_{\phi,MHD}} \sim \left[2\sqrt{2} M_0(1 - e^{-\frac{T_R}{T_1}})e^{-\frac{T_E}{T_2}} e^{b\boldsymbol{g}_f^{k\,T}\overline{\overline{D}}\boldsymbol{g}_f^k}\right]^{-1} \tag{2.16}$$

Finally, the noise level of the MHD flow velocity distribution in the direction of $\boldsymbol{g}_f^k$ is proportional to:

$$\sigma_{n_{\boldsymbol{v},MHD}} \sim \left[2\sqrt{2}(\gamma G_f \delta\Delta) M_0(1 - e^{-\frac{T_R}{T_1}})e^{-\frac{T_E}{T_2}} e^{b\boldsymbol{g}_f^{k\,T}\overline{\overline{D}}\boldsymbol{g}_f^k}\right]^{-1} \tag{2.17}$$

The SNR of the MHD flow velocity distributions can be estimated as:

$$\begin{gathered} SNR_{\boldsymbol{v},MHD} = \frac{S_{\boldsymbol{v},MHD}}{\sigma_{n_{\boldsymbol{v},MHD}}} \sim \\ S_{\boldsymbol{v},MHD}\left[2\sqrt{2}(\gamma G_f \delta\Delta) M_0(1 - e^{-\frac{T_R}{T_1}})e^{-\frac{T_E}{T_2}} e^{b\boldsymbol{g}_f^{k\,T}\overline{\overline{D}}\boldsymbol{g}_f^k}\right] \end{gathered} \tag{2.18}$$

The MHD flow velocity signal depends on the injected current amplitude (I) and duration (T_C) and can be expressed as a function of these:

$$SNR_{\boldsymbol{v},MHD} = \frac{S_{\boldsymbol{v},MHD}(I,T_C)}{\sigma_{n_{\boldsymbol{v},MHD}}} \sim S_{\boldsymbol{v},MHD}(I,T_C)\left[2\sqrt{2}(\gamma G_f \delta \Delta)M_0(1-e^{-\frac{T_R}{T_1}})e^{-\frac{T_E}{T_2}}e^{b\boldsymbol{g}_f^{k\,T}\overline{\overline{D}}\boldsymbol{g}_f^k}\right] \tag{2.19}$$

How $S_{\boldsymbol{v},MHD}(I,T_C)$ depends on I and T_C is non-trivial since it is highly nonlinear due to the nature of Navier-Stokes equations and the domain geometry strongly determines this relation. Hence, this function needs to be estimated empirically for the domain that is imaged.

2.3.2 Optimization of the Acquisition Parameters of the MHD Flow Velocity Images

After achieving an analytic equation that explains the relation between the SNR level of the MHD flow velocity images and image acquisition parameters, it is possible to make some analyses to come up with image acquisition parameters that maximize the SNR level.

2.3.2.1 Optimization of the Flow Encoding Parameters

The flow encoding parameters (G_f, δ, and Δ) appear explicitly in the two terms of (2.19). Firstly, they appear as linear product terms. Secondly, they appear non-linearly in the b-value term as explained in (2.4). Moreover, δ and Δ implicitly affect the T_E term since the following inequality must be satisfied when the SE-based pulse sequence in Figure 2.1 is utilized.

$$2T_C + \Delta + \delta + h < T_E \tag{2.20}$$

where h is time required for the 90° and 180° RF pulses, phase encoding gradient pulse and readout gradient pulse.

Let's assume the imaging medium is a liquid with an isotropic diffusion coefficient distribution (D) such as water and T_E is kept constant at a sufficiently large value that satisfy (2.20). Consequently, the SNR level function in (2.19) is proportional to the

following expression:

$$\gamma G_f \delta \Delta e^{-\gamma^2 G_f^2 \delta^2 (\Delta - \frac{\delta}{3}) D} \tag{2.21}$$

In general, $\Delta >> \frac{\delta}{3}$, so we can define a function F as:

$$F = \frac{\gamma}{2\pi} G_f \delta \Delta e^{-\gamma^2 G_f^2 \delta^2 \Delta D} \tag{2.22}$$

Moreover, the terms G_f and δ appears everywhere as a product with same powers. Hence, they can be merged into a single parameters as:

$$A = G_f \delta \tag{2.23}$$

Note that for arbitrary flow encoding gradient pulse shapes, A can be generalized as the area under a single flow encoding gradient pulse. Consequently, (2.22) becomes:

$$F = \frac{\gamma}{2\pi} A \Delta e^{-\gamma^2 A^2 \Delta D} \tag{2.24}$$

Finally, the task is to find optimal parameters (A, and Δ) that will maximize F. Firstly, one maximum can be found with respect to A:

$$A^* = \arg\max_A \{F\} \tag{2.25}$$

where A^* is the solution of the following equation:

$$\frac{\partial F}{\partial A}|_{A=A^*} = \frac{1}{2\pi}(1 - 2\gamma^2 (A^*)^2 D) \Delta e^{-\gamma^2 A^2 \Delta D} = 0 \tag{2.26}$$

Solution of (2.26) yields:

$$A^* = \frac{1}{\gamma \sqrt{2\Delta D}} \tag{2.27}$$

Secondly, with respect to Δ another maximum of F can be found as:

$$\Delta^* = \arg\max_\Delta \{F\} \tag{2.28}$$

Similarly, Δ^* is the solution of the following equation:

$$\frac{\partial F}{\partial \Delta}|_{\Delta=\Delta^*} = \frac{1}{2\pi}(1 - \Delta^* \gamma^2 A^2 D) e^{-\gamma^2 A^2 \Delta D} = 0 \tag{2.29}$$

Solution of (2.29) yields:

$$\Delta^* = \frac{1}{\gamma^2 A^2 D} \tag{2.30}$$

In summary, (2.27) and (2.30) provides two different relations between the parameters A and Δ. Note that F has no global maximum since (2.27) and (2.30) cannot be satisfied simultaneously. The important task here is to decide which relation provides a higher value of F. It is not possible to give a clear answer to this question due to the characteristics of the curves. Depending on the intervals that A and Δ values are chosen, the answer changes. To visualize this phenomenon, in Figure 2.2, two plots of F as a function of A and Δ are shown. In these plots, the diffusion coefficient of the water at room temperature ($D = 2.23 \times 10^{-3}$ mm^2/s) is utilized [52, 53].

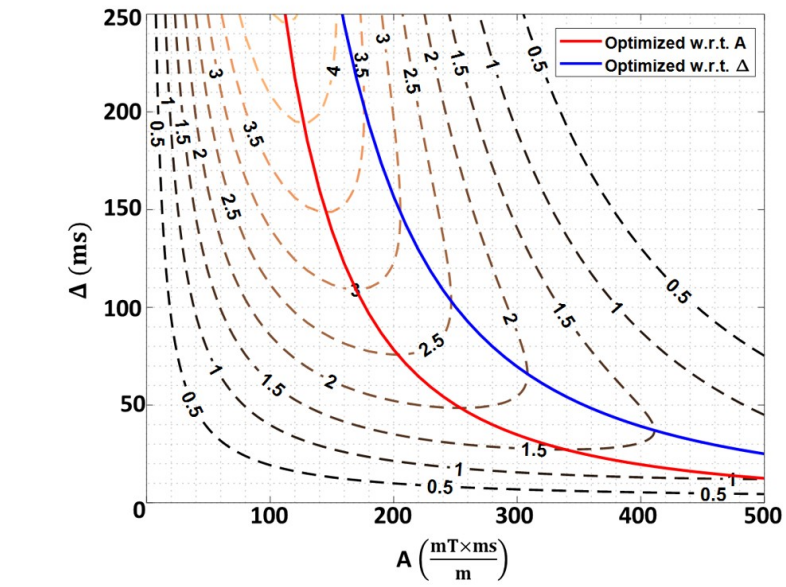

(a)

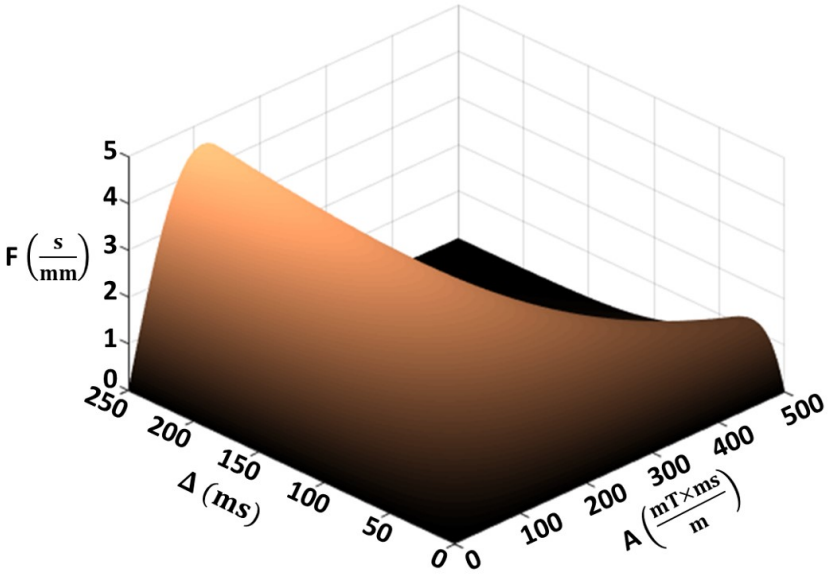

(b)

Figure 2.2: Analytical plots demonstrating F as a function of A and Δ with the diffusion coefficient of water at room temperature (D = 2.23×10^{-3} mm^2/s). (a) Contour plot of F. Dashed contours show the levels where F is constant and the value of F on these contours also provided. The solid red line shows the points where (2.27) (optimized w.r.t. A) is satisfied whereas the blue solid line shows the points where (2.30) (optimized w.r.t. Δ) is satisfied. (b) Surface plot of F.

In Figure 2.2(a), the relations (2.27) and (2.30) are also shown as red and blue solid lines, respectively. Here, it is seen that for large values of Δ, (2.27) provides higher F values whereas for small values of Δ, (2.30) provides higher F values. Moreover, the F values provided with (2.27) and large values of Δ tend to be higher in general. This is expected since F increases linearly both with increasing A and Δ. However, the exponential decrease due to the increasing A is much deteriorating than the exponential decrease due to the increasing Δ because of the order difference.

In conclusion, a basic flow encoding parameter selection procedure to maximize F, and accordingly $SNR_{\boldsymbol{v},MHD}$, can be formed as:

1. Select a reasonably large Δ value considering T_2 of the imaging domain since (2.20) must be satisfied.

2. Compute A from (2.27).

3. Choose G_f as the highest possible value the MR scanner can sustain.

4. Compute δ from (2.23).

Furthermore, (2.27) can be rearranged as:

$$\gamma^2 A^2 \Delta = \gamma^2 G_f^2 \delta^2 \Delta \approx b \approx \frac{1}{2D} \tag{2.31}$$

(2.31) suggests that every point on the red line in Figure 2.2(a) has approximately the same b-value which is approximately $\frac{1}{2D}$. For water at room temperature (D = 2.23$\times$10^{-3} mm^2/s), this value can be computed as b = 224 s/mm^2. Therefore, a simpler rule of thumb can be constructed as choosing a reasonably large Δ value while keeping the b-value at $\frac{1}{2D}$. Also, it is notable so say that every point on the blue line in Figure 2.2(a) has approximately the same b-value which is approximately $\frac{1}{D}$ with a similar derivation from (2.30).

The conducted analysis can be generalized to anisotropic media by utilizing the mean diffusivity ($\frac{Trace(\overline{\overline{D}})}{3}$) [34] instead of the scalar diffusion coefficient.

2.3.2.2 Optimization of the Current Injection Parameters

As mentioned, the dependency of $S_{\boldsymbol{v},MHD}(I,T_C)$, and consequently $SNR_{\boldsymbol{v},MHD}$, on the current injection parameters are non-trivial and will be determined empirically. However, the types of functions can be estimated since the MHD velocity distribution should be positively proportional to these parameters without any extrema. Moreover, for very high and very low values of the current injection parameters, saturation is expected. As a result, it is expected that the dependency of $S_{\boldsymbol{v},MHD}(I,T_C)$ on T_C can be fitted into an m$^{\text{th}}$ degree polynomial with a single term in the form (until saturation):

$$a_1 T_C^m \tag{2.32}$$

where a_1 is an arbitrary constant. Assuming minimum possible value for T_E is chosen in (2.20), $SNR_{\boldsymbol{v},MHD}$ is proportional to the following expression:

$$SNR_{\boldsymbol{v},MHD} \sim T_C^m e^{-\frac{(2T_C+\Delta+\delta+h)}{T_2}} \tag{2.33}$$

Thus, optimum T_C value should be chosen as:

$$T_C^* = \arg\max_{T_C}\{T_C^m e^{-\frac{(2T_C+\Delta+\delta+h)}{T_2}}\} \tag{2.34}$$

where T_C^* is the solution of the following equation:

$$\frac{\partial(T_C^m e^{-\frac{(2T_C+\Delta+\delta+h)}{T_2}})}{\partial T_C}|_{T_C=T_C^*} = -\frac{T_C^{m-1} e^{-\frac{(2T_C+\Delta+\delta+h)}{T_2}}(2T_C - mT_2)}{T_2} = 0 \tag{2.35}$$

(2.35) yields:

$$T_C^* = \frac{mT_2}{2} \tag{2.36}$$

Moreover, similar to T_C, it is expected that the dependency of $S_{\boldsymbol{v},MHD}(I,T_C)$ on I can be fitted into an n$^{\text{th}}$ degree polynomial with a single term in the form (until saturation):

$$a_2 I^n \tag{2.37}$$

where a_2 is an arbitrary constant. However, this is the only dependency of $SNR_{\boldsymbol{v},MHD}$ on I, hence, no analytical optimization of I is possible. Yet, it is also not possible to

increase I without any limit since the current injection amplitudes are considered to be safe up to 2 mA in clinical applications [54].

2.3.3 Empirical SNR Estimation Strategy

To estimate the SNR distributions of the obtained MHD distributions, strong strategies are needed. To estimate the noise levels of the images, a Principal Component Analysis (PCA) based noise level estimation method is utilized [55, 56].

After estimating the noise level ($\sigma_{n_{\boldsymbol{v}},MHD}$), a definition for the signal is also needed. Utilizing directly the mean of the measured signal is a weak approach since the velocity distributions have both positive and negative values. Hence, the Root Mean Square (RMS) value of the distributions provides more meaningful information. One problem is that directly computing the RMS value of the distribution includes the noise level.

Consider the second moment of the noisy MHD flow velocity distribution ($\tilde{\boldsymbol{v}}$):

$$E[\tilde{\boldsymbol{v}}^{\boldsymbol{2}}] = \mu^2_{\boldsymbol{v},MHD} + \sigma^2_{\boldsymbol{v},MHD} + \sigma^2_{n_{\boldsymbol{v}},MHD} \approx \frac{1}{N}\sum_{j=1}^{N} \tilde{\boldsymbol{v}}^2(j) \tag{2.38}$$

$\tilde{\boldsymbol{v}}(j)$ is the noisy MHD flow velocity in the j$^{\text{th}}$ pixel, N is the total number of pixels in the image, $\mu^2_{\boldsymbol{v},MHD}$ and $\sigma^2_{\boldsymbol{v},MHD}$ are the mean and the variance of the noiseless MHD flow velocity distribution, and $\sigma^2_{n_{\boldsymbol{v}},MHD}$ is the noise variance estimated before. Note that noise is assumed to be zero-mean white Gaussian noise. It is also assumed to be independent of the signal distribution. In other words, the second expectation provides the total energy in the image which is the summation of the energies of the noiseless signal itself ($\mu^2_{\boldsymbol{v},MHD} + \sigma^2_{\boldsymbol{v},MHD}$) and the energy of the noise ($\sigma^2_{n_{\boldsymbol{v}},MHD}$). Consequently, the pure signal RMS value can be estimated as:

$$S_{\boldsymbol{v},MHD}(I, T_C) \sim RMS_{\boldsymbol{v},MHD} \approx \sqrt{\frac{1}{N}\sum_{j=1}^{N} \tilde{\boldsymbol{v}}^2(j) - \sigma^2_{n_{\boldsymbol{v}},MHD}} \tag{2.39}$$

Consequently, empirical SNR of the MHD flow velocity images can be defined as:

$$SNR_{\boldsymbol{v},MHD} = \frac{S_{\boldsymbol{v},MHD}(I, T_C)}{\sigma_{n_{\boldsymbol{v},MHD}}} \sim \frac{RMS_{\boldsymbol{v},MHD}}{\sigma_{n_{\boldsymbol{v},MHD}}} \approx \frac{\sqrt{\frac{1}{N}\sum_{j=1}^{N} \tilde{\boldsymbol{v}}^2(j) - \sigma^2_{n_{\boldsymbol{v}},MHD}}}{\sigma_{n_{\boldsymbol{v},MHD}}} \tag{2.40}$$

2.4 Multi-Contrast Imaging

Another objective of the thesis, as mentioned before, is to develop strategies to simultaneously acquire data to reconstruct multiple contrast images with a minimum number of acquisitions. Later, each contrast image should be reconstructed with its unique reconstruction method. The contrast images that are the focus here are the current density, diffusion tensor, and MHD Flow velocity images.

Under the effect of a static magnetic field, the time behavior of proton spins (or bulk magnetization, $\boldsymbol{M}$) is explained by the Bloch equations [30]:

$$\frac{\partial \boldsymbol{M}}{\partial t} = \gamma \boldsymbol{M} \times B_0 \boldsymbol{k} - \frac{M_X \boldsymbol{i} - M_Y \boldsymbol{j}}{T_2} - \frac{(M_Z - M_0)\boldsymbol{k}}{T_1} \tag{2.41}$$

where $\boldsymbol{M} = [M_Z, M_Y, M_X]^T$ is the bulk magnetization vector.

The main assumption of (2.41) is that molecules in the medium are stationary, hence their position does not change in time. However, this is not always the case, and there can be mechanisms that create either incoherent or coherent motions. One example for the former is the self-diffusion of water molecules and a term explaining this phenomenon is added to (2.41) by Torrey in 1956 [27]. Then, the new form of the (2.41) is started to be called Bloch–Torrey equations as:

$$\frac{\partial \boldsymbol{M}}{\partial t} = \gamma \boldsymbol{M} \times B_0 \boldsymbol{k} - \frac{M_X \boldsymbol{i} - M_Y \boldsymbol{j}}{T_2} - \frac{(M_Z - M_0)\boldsymbol{k}}{T_1} + \nabla \cdot (D \nabla (\boldsymbol{M} - \boldsymbol{M_0})) \tag{2.42}$$

$\boldsymbol{M_0}$ is the equilibrium magnetization vector. Note that M_0 is not the magnitude of $\boldsymbol{M_0}$ but the z-component of the equilibrium magnetization as defined previously. Scalar diffusion coefficient in (2.42) can be replaced by the diffusion tensor ($\overline{\overline{D}}$) in the case of an anisotropic medium. The last term can easily be derived using Fick's law and the continuity equation.

The effect of a coherent motion can also be inserted into (2.42) as [28]:

$$\frac{\partial \boldsymbol{M}}{\partial t} = \gamma \boldsymbol{M} \times B_0 \boldsymbol{k} - \frac{M_X \boldsymbol{i} - M_Y \boldsymbol{j}}{T_2} - \frac{(M_Z - M_0)\boldsymbol{k}}{T_1} + \nabla \cdot (D \nabla (\boldsymbol{M} - \boldsymbol{M_0})) - \nabla \cdot (\boldsymbol{v} \boldsymbol{M}) \tag{2.43}$$

where $\boldsymbol{v}$ is the velocity distribution of any coherent motion of NMR active molecules such as the MHD flow in media with homogeneous viscosity. There are 3 important tensor operations appearing in (2.43): The divergence of a tensor field $\overline{\overline{A}}$ can be

defined in Cartesian coordinates as [57]:

$$\nabla \cdot \overline{\overline{A}} = \begin{bmatrix} \frac{\partial A_{xx}}{\partial x} + \frac{\partial A_{xy}}{\partial y} + \frac{\partial A_{xz}}{\partial z} \\ \frac{\partial A_{yx}}{\partial x} + \frac{\partial A_{yy}}{\partial y} + \frac{\partial A_{yz}}{\partial z} \\ \frac{\partial A_{zx}}{\partial x} + \frac{\partial A_{zy}}{\partial y} + \frac{\partial A_{zz}}{\partial z} \end{bmatrix} \tag{2.44}$$

The gradient of a vector field $\boldsymbol{a}$ can be defined in Cartesian coordinates as [57]:

$$\nabla \boldsymbol{a} = \begin{bmatrix} \frac{\partial a_x}{\partial x} & \frac{\partial a_x}{\partial y} & \frac{\partial a_x}{\partial z} \\ \frac{\partial a_y}{\partial x} & \frac{\partial a_y}{\partial y} & \frac{\partial a_y}{\partial z} \\ \frac{\partial a_z}{\partial x} & \frac{\partial a_z}{\partial y} & \frac{\partial a_z}{\partial z} \end{bmatrix} \tag{2.45}$$

The dyadic product of two vector fields $\boldsymbol{a}$ and $\boldsymbol{b}$ can be defined in Cartesian coordinates as [57]:

$$\boldsymbol{ab} = \begin{bmatrix} a_x b_x & a_x b_y & a_x b_z \\ a_y b_x & a_y b_y & a_y b_z \\ a_z b_x & a_z b_y & a_z b_z \end{bmatrix} \tag{2.46}$$

Finally, the current induced magnetic flux density (B_z) distribution can also be included in (2.43) as:

$$\frac{\partial \boldsymbol{M}}{\partial t} = \gamma \boldsymbol{M} \times (B_0 + B_z)\boldsymbol{k} - \frac{M_X \boldsymbol{i} - M_Y \boldsymbol{j}}{T_2} - \frac{(M_Z - M_0)\boldsymbol{k}}{T_1} + \nabla \cdot (D \nabla (\boldsymbol{M} - \boldsymbol{M_0})) - \nabla \cdot (\boldsymbol{v}\boldsymbol{M}) \tag{2.47}$$

The purpose of stating this fact here is to emphasize that the encoding mechanisms of coherent and incoherent motions into MR signal are fundamentally different even with the application of the identical motion-sensitizing (flow or diffusion encoding) gradients [30]. In this thesis study, the flow encoding and diffusion encoding terms are utilized interchangeably and refer to the same gradient pulse scheme in terms of practical aspects as shown in Figure 2.1. The coherent motion is encoded into the measured MR signal phase whereas incoherent motion is implicitly encoded into the measured MR signal magnitude since any incoherence between the proton spins

inside a single voxel causes a decrease in the cumulative magnetization due to the dephasing of the proton spins [28]. This idea is the foundation of the proposed multi-contrast imaging technique. When complex MR data is collected with the application of motion-sensitizing gradients, the magnitude distribution can be utilized to reconstruct incoherent motion based contrast images such as diffusion tensor images while the phase distribution provides coherent motion based contrast images such as MHD flow velocity images. Moreover, these different contrast images can be reconstructed independently, in other words, they do not affect each other as long as perfect coherence (zero-variance) and incoherence (zero-mean) are satisfied.

2.4.1 Current Density Imaging

To reconstruct the distribution of the externally injected current ($\boldsymbol{J}$), the current induced B_z distribution is needed. B_z distribution can simply be obtained by subtracting two phase images obtained with the SE-based pulse sequence shown in Figure 2.1 with the application of two opposing current injection polarities. Note that, to obtain B_z distribution, flow encoding gradients should not be applied. Hence, B_z distribution can be extracted as [11]:

$$B_z = \frac{\phi_I}{2\gamma T_C} = \frac{arg(S^{I+\boldsymbol{g}^k_{f0}}) - arg(S^{I-\boldsymbol{g}^k_{f0}})}{2} \tag{2.48}$$

$S^{I\pm\boldsymbol{g}^k_{f0}}$ are space signal distributions obtained with the application of opposing current injection polarities, and no flow encoding gradients.

The projected current density can be computed using measured magnetic flux density and simulation results of an identical FE model as [23]:

$$\boldsymbol{J}_P = \boldsymbol{J}_0 + \frac{1}{\mu_0}\left(\frac{\partial(B_z - B_{z,0})}{\partial y}, -\frac{\partial(B_z - B_{z,0})}{\partial x}, 0\right) \tag{2.49}$$

where, $\boldsymbol{J}_P$ is the computed projected current density, $\boldsymbol{J}_0$ is current density distribution of the homogeneous simulation model, $B_{z,0}$ is the z-component of magnetic flux density distribution of the homogeneous simulation model. The result of such a simulation is independent of the conductivity value of the material inside the numerical model as long as the amplitude of the injected currents is fixed. μ_0 is the vacuum permeability.

In general, $\boldsymbol{E} >> \boldsymbol{v} \times B_0\boldsymbol{k}$ and (2.8) can be simplified accordingly. Moreover, if $\boldsymbol{J}_P$ is utilized as the estimated current density distribution of the medium, Lorentz force density distribution inside the medium can be estimated as:

$$\boldsymbol{F}_L \approx \boldsymbol{J}_P \times B_0\boldsymbol{k} \tag{2.50}$$

2.4.2 Diffusion Tensor Imaging

In an anisotropic medium, the diffusion is characterized by the diffusion tensor which is a positive definite symmetric matrix in the form

$$\overline{\overline{D}} = \begin{bmatrix} d_{xx} & d_{xy} & d_{xz} \\ d_{xy} & d_{yy} & d_{yz} \\ d_{xz} & d_{yz} & d_{zz} \end{bmatrix} \tag{2.51}$$

instead of scalar distribution. This tensor appears in the Fick's law which describes the diffusion of the molecules under the effect of a concentration gradient as:

$$\boldsymbol{j} = \overline{\overline{D}}\nabla\rho \tag{2.52}$$

where $\boldsymbol{j}$ and ρ are the flux and concentration distributions of the liquid molecules.

However, even when no concentration gradient exists inside the medium, molecular diffusion still continues which is the random translational motion of the molecules. This is called Brownian motion and stems from the internal thermal energy that the molecules possess. This kind of random motion can be classified as a zero-mean, and consequently, incoherent motion. Therefore, to obtain diffusion tensor distribution, the magnitude images should be employed. The imaging technique where the diffusion phenomenon is encoded into the magnitude images via diffusion encoding gradients is called Diffusion-Weighted Imaging (DWI). DWI utilizes the fact that the MR magnitude signal decays under the effect of diffusion encoding gradients as given in (2.3).

$\boldsymbol{g}_f^k$ in (2.3) can be expressed as:

$$\boldsymbol{g}_f^k = \begin{bmatrix} r_k \\ p_k \\ q_k \end{bmatrix} \tag{2.53}$$

where r_k, p_k, and q_k are the direction cosines of the x-, y- and z-directions, respectively.

Combining (2.3), (2.52), and (2.53) following expressions can be obtained:

$$S_k = S_0 exp\left(-b\begin{bmatrix} r_k & p_k & q_k \end{bmatrix}\begin{bmatrix} d_{xx} & d_{xy} & d_{xz} \\ d_{xy} & d_{yy} & d_{yz} \\ d_{xz} & d_{yz} & d_{zz} \end{bmatrix}\begin{bmatrix} r_k \\ p_k \\ q_k \end{bmatrix}\right) \quad \text{for} \;\; k = 1, 2, ..., N \tag{2.54}$$

and

$$\ln\left(\frac{S_0}{S_k}\right) = b\begin{bmatrix} r_k & p_k & q_k \end{bmatrix}\begin{bmatrix} d_{xx} & d_{xy} & d_{xz} \\ d_{xy} & d_{yy} & d_{yz} \\ d_{xz} & d_{yz} & d_{zz} \end{bmatrix}\begin{bmatrix} r_k \\ p_k \\ q_k \end{bmatrix} \quad \text{for} \;\; k = 1, 2, ..., N \tag{2.55}$$

Moreover, (2.55) can be rearranged as:

$$\overline{\overline{R}}\boldsymbol{d} = \begin{bmatrix} r_1^2 & p_1^2 & q_1^2 & 2r_1p_1 & 2r_1q_1 & 2p_1q_1 \\ r_2^2 & p_2^2 & q_2^2 & 2r_2p_2 & 2r_2q_2 & 2p_2q_2 \\ \vdots & \vdots & \vdots & \vdots & \vdots & \vdots \\ r_N^2 & p_N^2 & q_N^2 & 2r_Np_N & 2r_Nq_N & 2p_Nq_N \end{bmatrix}\begin{bmatrix} d_{xx} \\ d_{yy} \\ d_{zz} \\ d_{xy} \\ d_{xz} \\ d_{yz} \end{bmatrix} = \frac{1}{b}\begin{bmatrix} \ln\left(\frac{S_0}{S_1}\right) \\ \ln\left(\frac{S_0}{S_2}\right) \\ \vdots \\ \ln\left(\frac{S_0}{S_N}\right) \end{bmatrix} = \boldsymbol{s} \tag{2.56}$$

As can be seen from (2.56), N must be minimum 6 and $\boldsymbol{g}_f^k$ must be regulated so that $\overline{\overline{R}}$ becomes full column rank. Moreover, one additional image acquisition without any diffusion encoding gradient application must be done to obtain S_0. Thus, a total minimum of 7 image acquisitions are required to reconstruct the diffusion tensor.

Consequently, the six independent element of the diffusion tensor can be found using the least squares solution as:

$$\boldsymbol{d} = \left(\overline{\overline{R}}^T\overline{\overline{R}}\right)^{-1}\overline{\overline{R}}^T\boldsymbol{s} \tag{2.57}$$

Although this solution method is able to provide the result theoretically, there may be some practical considerations due to the existence of noise on the right-hand side in (2.56). One concern is the condition number of the system of equations appearing in (2.56). As can be seen, this condition number depends on the number and the scheme

of the diffusion encoding directions. Although increasing the number of diffusion encoding directions improves the diffusion tensor element calculations, it has been observed that the gain in the image quality becomes gradually less significant when $N = 25$ is exceeded [58]. Moreover, the utilized diffusion encoding scheme determines the structure and, consequently, the condition number of the system matrix in (2.56). Hence, determining the optimal diffusion encoding scheme that will minimize the condition number is an active problem in DTI research since there are infinitely many different noncollinear gradient directions in 3D space for the same N [30]. Finally, different regularization methods can be utilized for the solution of (2.56) instead of basic least squares approach to increase the robustness of the solution to the noise such as multivariate linear regression method [30, 59].

2.4.3 MHD Flow Velocity Imaging

The aim of the MHD flow velocity imaging is to reconstruct the MHD flow velocity as vector distribution in the form:

$$\boldsymbol{v} = \begin{bmatrix} v_x \\ v_y \\ v_z \end{bmatrix} \tag{2.58}$$

where v_x, v_y, and v_z are the components of the MHD flow velocity distribution in the x-, y- and z-directions, respectively.

Substituting (2.53) and (2.58) into (2.12) results in:

$$\begin{bmatrix} r_k & p_k & q_k \end{bmatrix} \begin{bmatrix} v_x \\ v_y \\ v_z \end{bmatrix} = \frac{\phi_{MHD,\boldsymbol{g}_f^k}}{\gamma G_f \delta \Delta} \quad \text{for} \quad k = 1, 2, ..., N \tag{2.59}$$

(2.59) can also be rearranged as a linear system of equations for N measurements as:

$$\begin{bmatrix} r_1 & p_1 & q_1 \\ r_2 & p_2 & q_2 \\ \vdots & \vdots & \vdots \\ r_N & p_N & q_N \end{bmatrix} \begin{bmatrix} v_x \\ v_y \\ v_z \end{bmatrix} = \frac{1}{\gamma G_f \delta \Delta} \begin{bmatrix} \phi_{MHD,\boldsymbol{g}_f^1} \\ \phi_{MHD,\boldsymbol{g}_f^2} \\ \vdots \\ \phi_{MHD,\boldsymbol{g}_f^N} \end{bmatrix} \tag{2.60}$$

Hence, N must be equal to or larger than 3. However, note that $\phi_{MHD,\,\boldsymbol{g}_f^k}$ are obtained as a weighted average of four independent flow encoded phase images with opposing flow encoding and current injection polarities as given in (2.10). Therefore, minimum of 12 image acquisitions must be conducted to reconstruct all three components of the MHD flow velocity distribution without any artifacts.

For instance, the most basic $\boldsymbol{g}_f^k$ set that can be utilized for MHD flow velocity imaging is:

$$\boldsymbol{G}_f^1 = \begin{bmatrix} 1 \\ 0 \\ 0 \end{bmatrix}, \boldsymbol{G}_f^2 = \begin{bmatrix} 0 \\ 1 \\ 0 \end{bmatrix}, \boldsymbol{G}_f^3 = \begin{bmatrix} 0 \\ 0 \\ 1 \end{bmatrix} \tag{2.61}$$

When 12 measurements are taken with $\boldsymbol{g}_f^k = \boldsymbol{G}_f^k$, the system matrix in (2.60) becomes identity. Thus, $\boldsymbol{v}$ can be directly solved from (2.10) and (2.12) which is the most common MHD flow velocity imaging technique in the literature [1, 7–10].

However, this flow encoding set is not the only possible choice to reconstruct the MHD flow velocity distribution. Any set that will make the system matrix in (2.60) full column rank can also be utilized.

The image reconstruction strategy of the MHD flow velocity distribution can be improved by utilizing more complex flow encoding sets and implicitly burying the opposing flow encoding step into the designed flow encoding set. For example, consider the following flow encoding set:

$$\boldsymbol{G}_f^{1^*} = \begin{bmatrix} 1 \\ 0 \\ 1 \end{bmatrix}, \boldsymbol{G}_f^{2^*} = \begin{bmatrix} -1 \\ 0 \\ 1 \end{bmatrix}, \boldsymbol{G}_f^{3^*} = \begin{bmatrix} 1 \\ 1 \\ 0 \end{bmatrix}, \boldsymbol{G}_f^{4^*} = \begin{bmatrix} 1 \\ -1 \\ 0 \end{bmatrix}, \boldsymbol{G}_f^{5^*} = \begin{bmatrix} 0 \\ 1 \\ 1 \end{bmatrix}, \boldsymbol{G}_f^{6^*} = \begin{bmatrix} 0 \\ 1 \\ -1 \end{bmatrix} \tag{2.62}$$

If $\boldsymbol{g}_f^k = \frac{\boldsymbol{G}_f^{k^*}}{\sqrt{2}}$ is utilized as the flow encoding set, no further data acquisition with altering the directions of the flow encoding gradients are required since all the information needed to discard all the artifact terms in (2.9) except $\phi_{\boldsymbol{g}_f^k}$ is collected. The reason is that the vectors in the set are coupled where in each couple a single element of the vector changes sign. Moreover, all the elements change sign at least one time. This way gradients base artifacts in each direction can be uniquely determined and elim-

inated. Yet, in order to discard $\phi_{\boldsymbol{g}_f^k}$ as well, still, another data set must be acquired with an opposing current injection polarity. Again, 12 independent measurements are needed.

A similar system of equations to (2.60) can be constructed with $\boldsymbol{G}_f^{k*}$. However, the right hand side does not need to be in terms of $\phi_{MHD,\,\boldsymbol{g}_f^k}$ anymore. Instead, $arg(S^{I\pm\boldsymbol{G}_f^k}) = \phi^{I\pm\boldsymbol{G}_f^k}$ can be directly utilized as:

$$\overline{\overline{G}}\boldsymbol{v} = \begin{bmatrix} \boldsymbol{G}_f^{1*T} \\ \vdots \\ \boldsymbol{G}_f^{6*T} \\ -\boldsymbol{G}_f^{1*T} \\ \vdots \\ -\boldsymbol{G}_f^{6*T} \end{bmatrix}_{12\times 3} \begin{bmatrix} v_x \\ v_y \\ v_z \end{bmatrix}_{3\times 1} = \frac{1}{\gamma G_f \delta \Delta} \begin{bmatrix} \phi^{I+\boldsymbol{G}_f^{1*}} \\ \vdots \\ \phi^{I+\boldsymbol{G}_f^{6*}} \\ \phi^{I-\boldsymbol{G}_f^{1*}} \\ \vdots \\ \phi^{I-\boldsymbol{G}_f^{6*}} \end{bmatrix}_{12\times 1} = \boldsymbol{p} \tag{2.63}$$

Note that $\overline{\overline{G}}$ is a full column rank matrix, hence, the least squares solution can be obtained as:

$$\boldsymbol{v} = \left(\overline{\overline{G}}^T \overline{\overline{G}}\right)^{-1} \overline{\overline{G}}^T \boldsymbol{p}$$

$$= \frac{1}{8} \begin{bmatrix} 1 & -1 & 1 & 1 & 0 & 0 & -1 & 1 & -1 & -1 & 0 & 0 \\ 0 & 0 & 1 & -1 & 1 & 1 & 0 & 0 & -1 & 1 & -1 & -1 \\ 1 & 1 & 0 & 0 & 1 & -1 & -1 & -1 & 0 & 0 & -1 & 1 \end{bmatrix} \boldsymbol{p} \tag{2.64}$$

Here, the similarity of the new reconstruction method to (2.10) can be seen clearly. In fact, the operation conducted in the 1st row, 1st, 2nd, 7th and 8th columns to extract $\boldsymbol{v}$ is identical to the weighted averaging done in (2.10). In (2.62), it can be seen that the difference of the phase images obtained with $\boldsymbol{G}_f^{1*}$ and $\boldsymbol{G}_f^{2*}$ flow encoding directions provides the MHD flow velocity information in the x-direction. Since the listed columns correspond to these flow encoding vectors, the similarity to (2.10) can be understood. However, the MHD flow velocity information in the x-direction can also be extracted by summing the phase images obtained with $\boldsymbol{G}_f^{3*}$ and $\boldsymbol{G}_f^{4*}$ flow encoding directions. Therefore, 4 other nonzero elements appear in the first row in (2.64). Finally, the average of these is taken to end up with a single estimation of v_x distribution. Due to this final averaging, the coefficient $\frac{1}{8}$ appears in the front instead of $\frac{1}{4}$.

All these observations validate the claim that with the utilization of the gradient set $\boldsymbol{G}_f^{k^*}$, all the artifact terms in (2.9) are eliminated and there is no need to collect additional data with opposing flow encoding directions.

Finally, the advantage of utilizing the flow encoding gradient set $\boldsymbol{G}_f^{k^*}$ instead of $\boldsymbol{G}_f^k$ is the fact that $\boldsymbol{G}_f^{k^*}$ satisfies DTI reconstruction conditions in addition to MHD flow velocity image reconstruction conditions. Namely, if $\boldsymbol{g}_f^k = \frac{\boldsymbol{G}_f^{k^*}}{\sqrt{2}}$ is utilized during the image acquisition, both $\overline{\overline{R}}$ in (2.56) and $\overline{\overline{G}}$ in (2.63) becomes full column rank. Therefore, the targeted multi-contrast simultaneous image acquisition to reconstruct the diffusion tensor and the MHD flow velocity distributions from the complex data can be achieved with $\boldsymbol{G}_f^{k^*}$ whereas $\boldsymbol{G}_f^k$ cannot satisfy the DTI image reconstruction condition.

Moreover, any diffusion encoding gradient set that can be utilized to reconstruct the diffusion tensor can also be utilized instead of $\boldsymbol{G}_f^{k^*}$ with the generalization of the developed image reconstruction technique in (2.62-2.64). The only factor that needs to be taken into consideration is that the image acquisition procedure with any chosen diffusion encoding gradient set must be repeated twice with the opposing current injection polarities.

As mentioned, with the utilization of $\boldsymbol{G}_f^{k^*}$, 12 phase images are enough to extract the MHD flow velocity distribution. Simultaneously, the magnitude images of the same data set can be used in (2.57) as the diffusion-weighted images. However, the magnitude images actually contain 6 pairs where each pair contains the same diffusion-weighted distribution twice since current injection does not affect the magnitude images. On the other hand, to obtain B_z distribution of the same imaging slice with (2.48), 2 additional images are required with current injection and without flow encoding gradient application. The magnitude images of these acquisitions can be utilized as S_0 images in (2.57). In conclusion, 14 complex images (14 magnitude and 14 phase images) obtained in 14 image acquisitions can provide B_z, MHD flow velocity, and diffusion tensor distributions with 100% efficiency, i.e. all the collected data is employed in the image reconstruction of a contrast distribution. In addition, since magnitude images include an implicit averaging factor of 2, the obtained diffusion tensor images have an $\sqrt{2}$ SNR advantage.

If multi-contrast imaging is not utilized, MRCDI requires 2, DTI with the same SNR level requires 14, and MHD flow velocity imaging requires 12 image acquisitions which correspond to 28 image acquisitions in total. Hence, multi-contrast imaging provides a 50% decrease in the total image acquisition time in addition to the perfect efficiency of the utilization of the acquired data during image reconstruction.

CHAPTER 3

SIMULATION MODEL AND EXPERIMENTAL SETUP

3.1 Introduction

In this section, the numerical simulation model, the experimental setup and phantoms, and the MRI scanner are demonstrated and explained. In Section 3.2, the details related to the numerical model and simulation parameters are provided. Three experimental phantoms and experimental data acquisition parameters in different experiments are given in Section 3.3. For each major focus of the thesis, an appropriate phantom is designed and implemented. Section 3.4 presents the image acquisition system. Finally, two employed current injection schemes during experiments are explained in Section 3.5 with the utilized SE-based pulse sequence.

3.2 Numerical Model

In order to validate the formation of the MHD flow due to the interaction of orthogonal magnetic and electrical fields, a Finite Element (FE) numerical model is prepared in COMSOL Multiphysics® software [60] and a time-dependent study is conducted.

The simulation model is composed of a cubic structure of dimension $80\times80\times80$ mm^3 and 4 attached cubic electrodes of dimensions $20\times20\times20$ mm^3. The mesh structure of the simulation model consists of 10906 tetrahedral, 3472 prism, 1624 triangular, 240 edge, and 45 vertex elements. This mesh size is chosen because further decreasing mesh size did not increase the accuracy of the solution but only increased computation time. Figure 3.1 shows the 3D solid and the mesh structure of the phantom. Moreover, in Figure 3.1(a) the direction of the static magnetic field and the current

injection direction are shown.

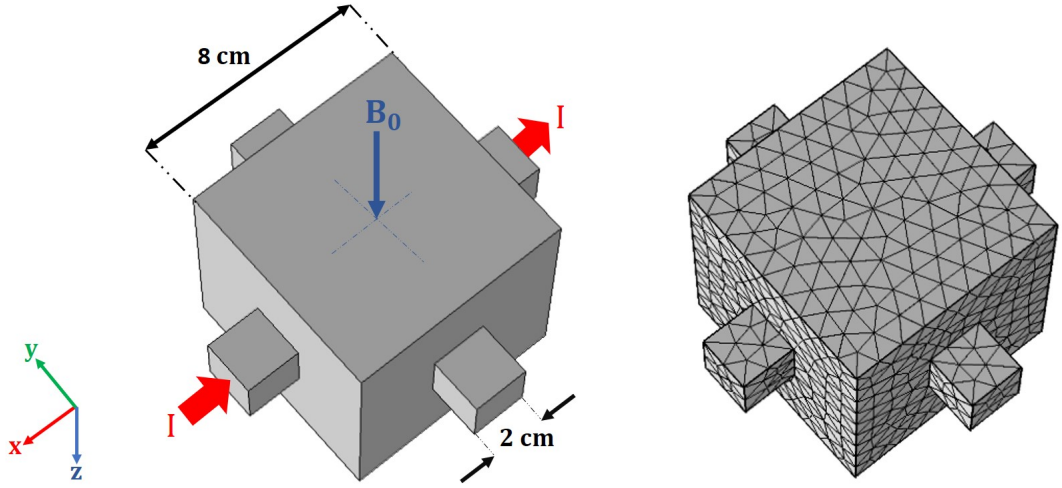

(a) (b)

Figure 3.1: FE simulation model. (a) 3D solid structure, and (b) the mesh structure of the simulation model.

The material of the simulation model is chosen as "Water, liquid" from the material library of the COMSOL Multiphysics®. σ value of the liquid material is overwritten as 1 S/m. B_0 distribution appearing in (2.8) is defined as a constant field in the z-direction with 3T amplitude. Moreover, the E distribution is computed with the *Electrical Currents* interface of the solver by solving the Poisson's equation with Neumann boundary conditions with the current injection configuration shown in Figure 3.1(a) as:

$$\begin{aligned} \nabla \cdot (\nabla V) &= 0 \quad \text{in } \Omega \\ -\sigma \tfrac{\partial V}{\partial \boldsymbol{n}} &= g \quad \text{on } \nabla\Omega \end{aligned} \tag{3.1}$$

where Ω is the domain shown in Figure 3.1(a) and g is the normal current density into the domain on the cubic electrode surfaces due to the injected current with amplitude I.

After obtaining $\boldsymbol{F}_L$ distribution with (2.8), problem in (2.6) and (2.7) is modeled using

the *Laminar Flow* interface of the solver with the following boundary conditions:

$$\begin{aligned} \boldsymbol{v} &= 0 \quad \text{on } \nabla\Omega \\ \boldsymbol{f_0} &= 0 \quad \text{on } \nabla\Omega \end{aligned} \tag{3.2}$$

where $\boldsymbol{f_0}$ is the normal stress on the boundaries. Moreover, open and no-slip boundary conditions are chosen for the top and the other surfaces, respectively. The maximum step size for the time-dependent study is adjusted as 1 ms.

As can be seen from Figure 2.1, the injected current is a monopolar pulse with duration T_C and since it is injected in each T_R interval, it has an injection frequency of $\frac{1}{T_R}$. To simulate this current injection pattern in the simulation model, $\boldsymbol{F}_L$ is defined as a function of time where it has the value (2.8) provides while current injection and 0 otherwise.

The simulated $\boldsymbol{v}$ images are obtained with a very similar technique that is explained in [9]. The $\boldsymbol{v}$ distribution is sampled in each T_R, and transformed into an MR phase distribution via (2.12). An empty rectilinear k-space is filled with the complex data with the phase equal to the obtained distribution and magnitude equal to unity. Namely, the n^{th}-line in the k-space is filled with the data obtained from the n^{th}-cycle of the time-dependent simulation. Finally, a phase image is reconstructed from the filled k-space with the inverse Fourier Transform, and the MHD flow velocity distribution is obtained with (2.11).

3.3 Experimental Phantoms

Different experimental phantoms are prepared to experimentally validate the derived theory and conducted analyses. All experimental phantoms have a Plexiglass container and they are filled with saline solutions that have specific conductivity, T_1 and T_2 values. The phantoms utilized in the MHD flow velocimetry and MHD flow velocity sensitivity analysis are homogeneous structures whereas the phantoms designed for multi-contrast imaging purposes have biological tissue samples as inhomogeneities to provide anisotropy inside the domain. Moreover, both square and cylindrical-shaped phantoms are utilized to obtain MHD flow velocity distributions

to show the applicability of the proposed algorithms in different geometries. The square phantoms have difficult geometries for both MRCDI and MHD flow velocity imaging since current density values in the corners become very low and very low SNR values are obtained in those regions. The cylindrical phantom, on the other hand, has a relatively simpler geometry in terms of the current distributions inside the medium because of the smooth boundaries.

The current pulses are injected into the media via recessed electrode structures that exist on the four sides of the experimental phantoms. The current pulses are generated using a custom-designed current source that is designed and implemented by Eroğlu et al. [61].

3.3.1 Phantom I - Homogeneous Square Phantom

The homogeneous square phantom is shown in Figure 3.2. The phantom is filled with a saline solution that contains 7.5 g/L NaCl and 0.5 g/L $CuSO_4$. The T_1 and T_2 values are 500 ms and 400 ms, respectively [62]. Moreover, the conductivity of the saline solution is 1 S/m.

The current is injected only in the horizontal direction with copper electrodes and cables. This phantom is utilized to show that MHD flow velocity distributions can be obtained via the SE-based pulse sequence given in Figure 2.1. Moreover, this phantom has the same geometry as the numerical model given in Section 3.2, and the same current injection levels and durations are employed.

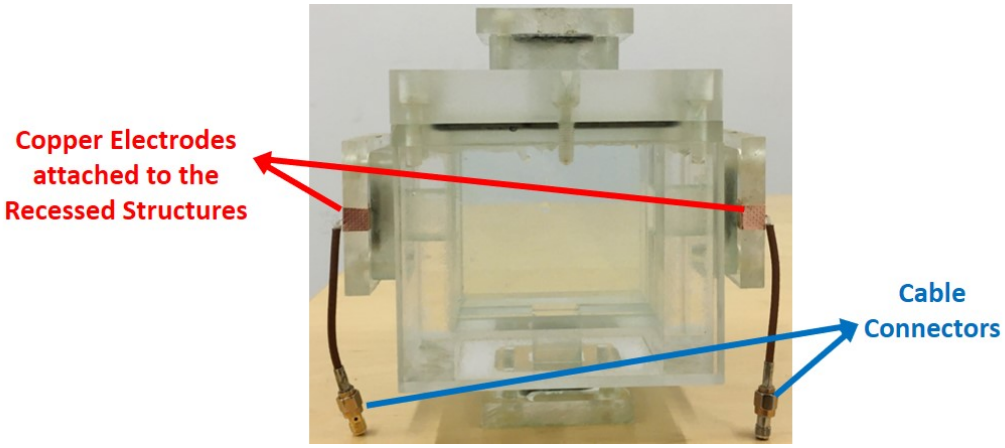

Figure 3.2: Homogeneous square experimental phantom with the dimensions of $80\times80\times80$ mm^3. The copper electrodes attached to the recessed structures and the cable connectors are also shown. The dimensions of all recessed structures are $20\times20\times20$ mm^3.

The image acquisition parameters used during the experiments with the homogeneous square phantom are given in Table 3.1.

Table 3.1: The imaging parameters of the experiments conducted with the homogeneous square phantom.

Parameter	**Value**
T_R	1000 ms
T_E	75 ms
FOV	150×150 mm^2
Matrix Size	64
BW	130 Hz/Pixel
Slice Thickness	5 mm
T_C	5, 10 ms
I	5, 10 mA
G_f	30 mT/m
δ	10 ms
Δ	50 ms

3.3.2 Phantom II - Homogeneous Cylindrical Phantom

The homogeneous cylindrical phantom is shown in Figure 3.3. The phantom is filled with a saline solution that contains 13.5 g/L NaCl and 0.36 g/L $CuSO_4$. The T_1 and T_2 values are 620 ms and 500 ms, respectively [62]. Moreover, the conductivity of the saline solution is 1.8 S/m. The solution has conductivity and T_2 values of the Cerebrospinal Fluid [63, 64].

The current is injected both in the horizontal and vertical directions with copper electrodes and cables. This phantom is utilized during the sensitivity analysis of the MHD flow velocity on the image acquisition parameters.

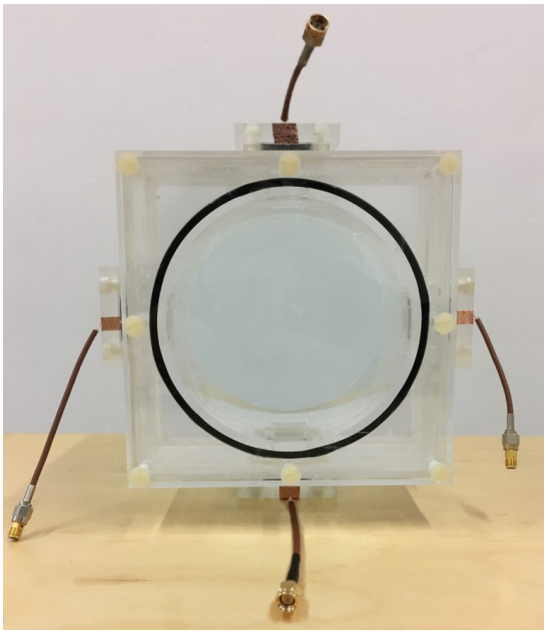

Figure 3.3: Homogeneous cylindrical experimental phantom with 120 mm diameter and 140 mm height. The figure also shows 4 copper electrodes attached to 4 recessed structures and 4 cable connectors. The dimensions of all recessed structures are $20\times20\times20$ mm^3.

The image acquisition parameters used during experiments with the homogeneous cylindrical phantom are given in Table 3.2.

Table 3.2: The imaging parameters of the experiments conducted with the homogeneous cylindrical phantom.

Parameter	**Value**
T_R	500 ms
T_E	75 ms
FOV	256×256 mm^2
Matrix Size	128
BW	130 Hz/Pixel
Slice Thickness	5 mm
T_C	10 ms
I	10 mA
G_f	35 mT/m
δ	14 ms
Δ	34 ms

3.3.3 Phantom III - Inhomogeneous Cubic Phantom

The inhomogeneous cubic phantom is shown in Figure 3.4. The phantom is filled with a saline solution that contains 3.75 g/L NaCl and 6.3 mg/L $MnCl_2$. The T_1 and T_2 values are 1700 ms and 200 ms, respectively [62]. Moreover, the conductivity of the saline solution is 0.5 S/m. The solution has conductivity and T_2 values of human blood [65, 66]. Moreover, two bovine muscle pieces are placed inside the phantom as anisotropic inhomogeneities with the aid of the holder apparatus.

The current is injected both in the horizontal and vertical directions with copper electrodes and cables. During the simultaneous multi-contrast image acquisition experiments, this phantom is utilized since it both includes fluid and biological tissue regions where MHD flow and anisotropic diffusion are observed, respectively.

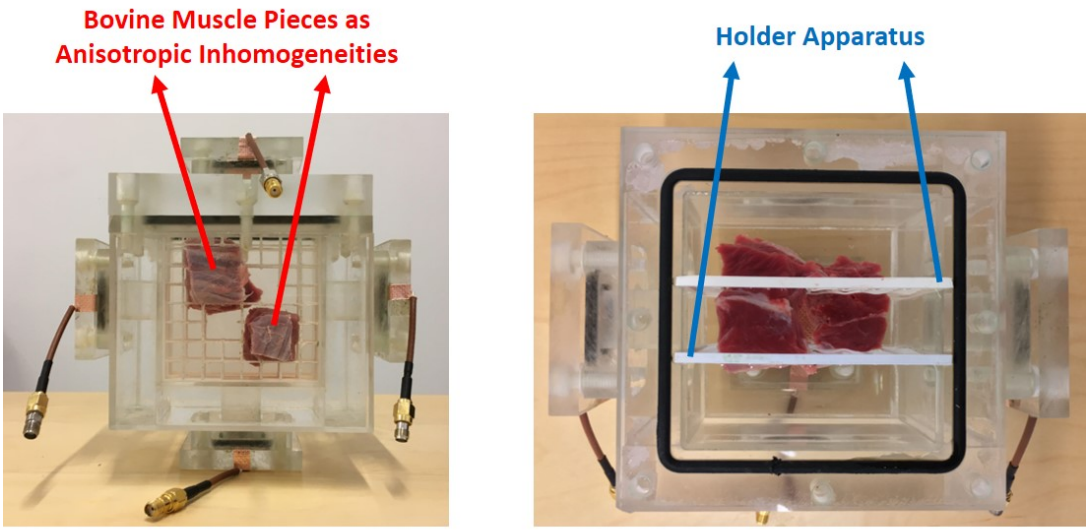

Figure 3.4: Inhomogeneous cubic phantom with dimensions 80×80×80 mm^3 that contains two bovine muscle pieces as anisotropic inhomogeneities that are placed with the aid of the holder apparatus. (a) The front view, and (b) top view.

The image acquisition parameters used during experiments with the inhomogeneous square phantom are given in Table 3.3.

Table 3.3: The imaging parameters of the experiments conducted with the inhomogeneous square phantom.

Parameter	**Value**
T_R	1000 ms
T_E	75 ms
FOV	128×128 mm^2
Matrix Size	64
BW	130 Hz/Pixel
Slice Thickness	5 mm
T_C	10 ms
I	10 mA
G_f	35 mT/m
δ	14 ms
Δ	34 ms

3.4 MRI System

The phantom experiments are performed using a 3T MRI scanner (MAGNETOM Trio, Siemens AG, Erlangen, Germany) in the facilities of UMRAM (National Magnetic Resonance Research Center), Bilkent University, Ankara, Turkey. The MR scanner is shown in Figure 3.5. The copper cables are tried to be placed as parallel as possible with z-direction nearside of the phantom in order to minimize the magnetic stray fields inside the phantom [67]. All data is acquired using the single-channel RF body coil of the MR scanner.

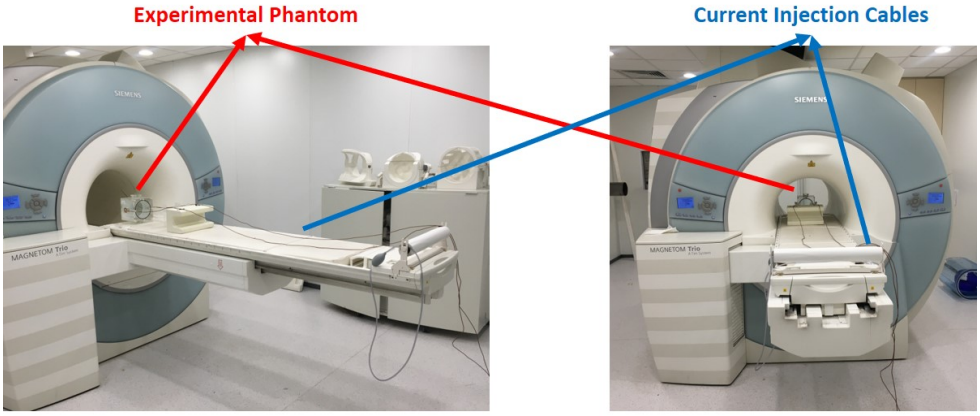

Figure 3.5: Siemens MAGNETOM Trio 3T MR scanner and the experimental setup. (a) Table outside, (b) table inside.

3.5 Single and Double Current Pulse Schemes

The pulse sequence in Figure 3.6 is designed for the simultaneous imaging of multiple contrast distributions (current density, diffusion tensor, and MHD flow velocity). To obtain data that will provide all these contrast distributions, 14 image acquisitions should be conducted (2 with only current injection, 12 with both current injection and flow encoding). One important point here is that there are two schemes with the utilization of the current pulses I and II. The first scheme is to utilize only current pulse I. With this scheme, it is possible to obtain all three contrast distributions directly. How-

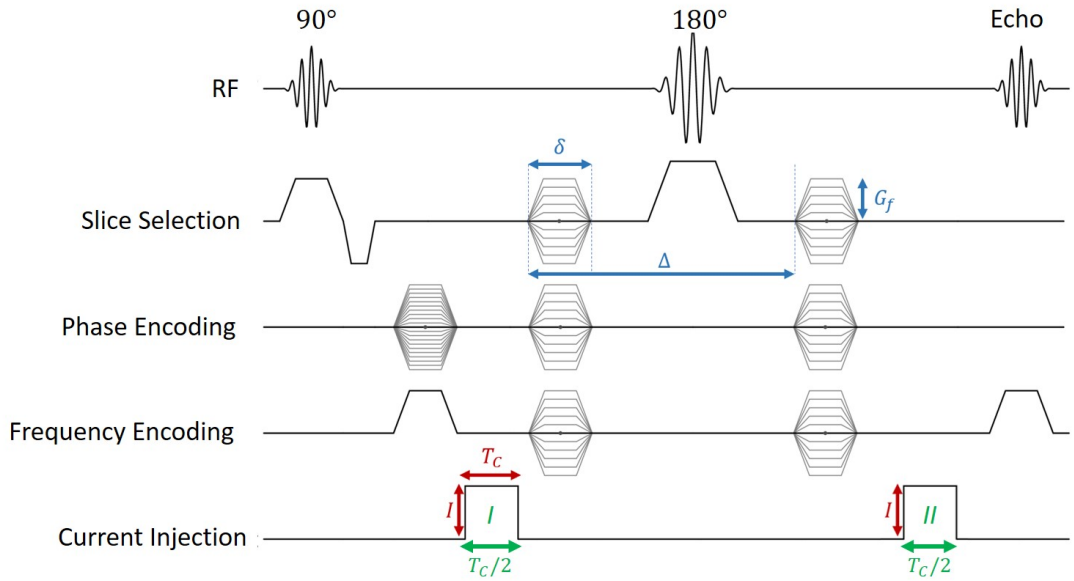

Figure 3.6: The SE-based pulse sequence showing single (red) and double (green) current pulse schemes.

ever, this scheme is sub-optimal because a time interval equal to the current injection duration must be spent blank just before the readout due to the symmetrical nature of the SE-based pulse sequence. The second scheme is to utilize both time intervals for the current injection (both pulses I and II). However, the drawback of this scheme is that reconstructing both MHD flow velocity and B_z distributions directly from the acquired phase images is not possible. To obtain the B_z distribution, pulse II should be inverted. However, pulse II should have the same polarity as pulse I in order not to suspend the MHD flow. This can be achieved with a programmable current source that will inject bipolar current pulses during B_z imaging and unipolar current pulses during the imaging procedures with flow encoding.

Note that the current injection duration (T_C) definitions in Figure 3.6 are different for a single current pulse and double current pulse schemes. For a single pulse injection scheme, T_C corresponds to the duration of this single pulse while for the double pulse scheme, T_C corresponds to the summation of the durations of the two current pulses.

All derivations and analyses conducted in Chapter 2 are still valid with the double

pulse scheme only except (2.20) and (2.36). (2.20) becomes:

$$T_C + \Delta + \delta + h < T_E \tag{3.3}$$

and (2.36) becomes:

$$T_C^* = mT_2 \tag{3.4}$$

with the T_C definition of the double current pulse scheme.

CHAPTER 4

RESULTS AND DISCUSSION

4.1 Introduction

In this chapter, the analytical and experimental results obtained to validate the theory and mathematical derivations of the image reconstruction methods and conducted analyses given in Chapter 2 are presented, and the results are discussed in detail. In Section 4.2, the results obtained with numerical simulations and physical experiments are compared. The effect of single and double current pulse schemes, and horizontal and vertical current injection patterns are inspected in Section 4.3. Section 4.4 presents the results related to the SNR analysis of the MHD flow velocity images. In Section 4.5, the effect of the diffusion and MHD events on the MR magnitude images are evaluated. In Section 4.6, the contrast images obtained using multi-contrast image reconstruction and data acquisition techniques are displayed. Finally, Section 4.7 provides the minimum current amplitudes required for the MHD flow velocity imaging for different imaging parameters.

4.2 Comparison of the Simulated and Experimentally Acquired MHD Flow Velocity Images

To validate the MHD flow velocimetry techniques explained in Section 2.2, MHD flow velocity images are obtained with an FE-based numerical model as explained in Section 3.2. The numerical model is run with 3 different current injection pulses. The obtained results are presented in Figure 4.1.

Moreover, the MHD flow velocity distributions are also experimentally acquired with

the homogeneous cubic phantom shown in Figure 3.2 with the image acquisition parameters given in Table 3.1. The MHD flow velocity images are reconstructed using (2.10) and (2.12). The obtained results are demonstrated in Figure 4.2.

The results presented in this section are presented in [68].

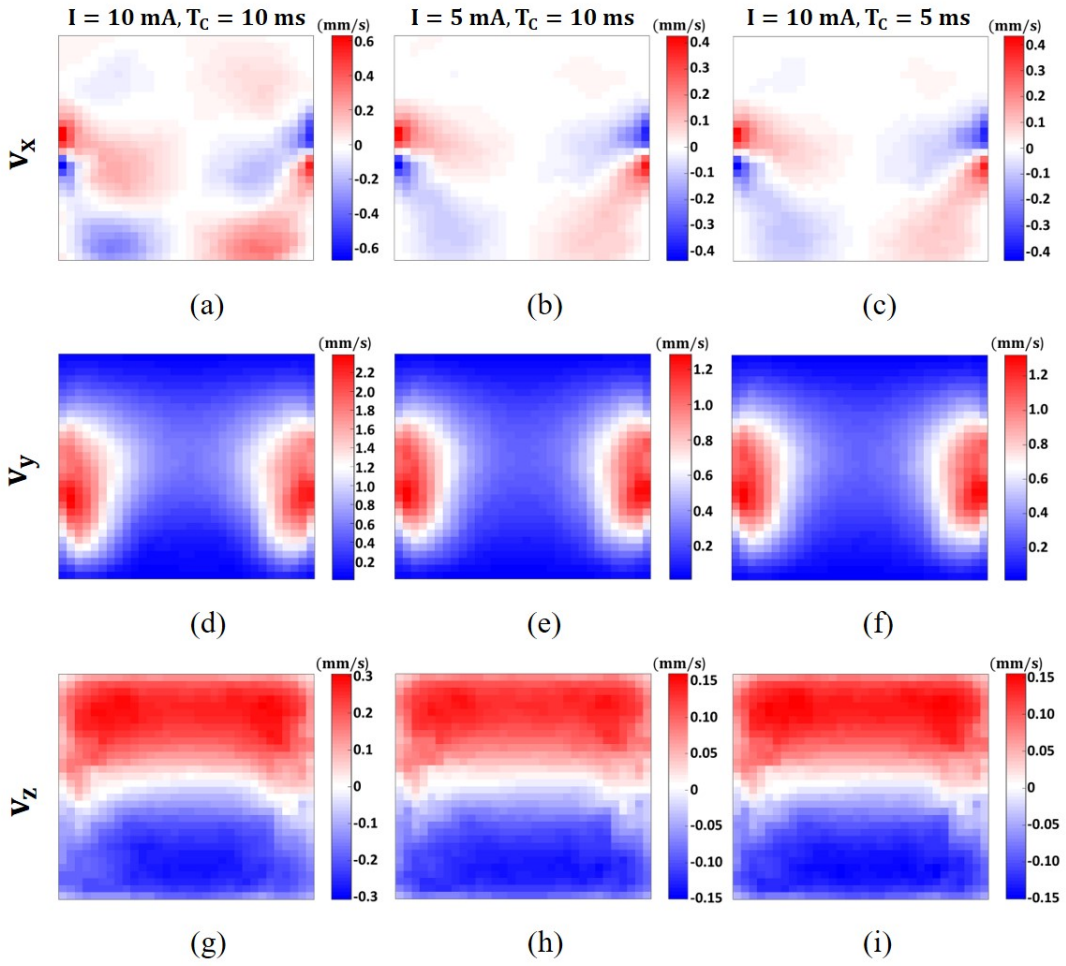

Figure 4.1: Simulated MHD flow velocity distributions using the numerical model: x-component with current injection parameters (a) I=10 mA, T_C=10 ms, (b) I=5 mA, T_C=10 ms, and (c) I=10 mA, T_C=5 ms; y-component with current injection parameters (d) I=10 mA, T_C=10 ms, (e) I=5 mA, T_C=10 ms, and (f) I=10 mA, T_C=5 ms; and z-component with current injection parameters (g) I=10 mA, T_C=10 ms, (h) I=5 mA, T_C=10 ms, and (i) I=10 mA, T_C=5 ms.

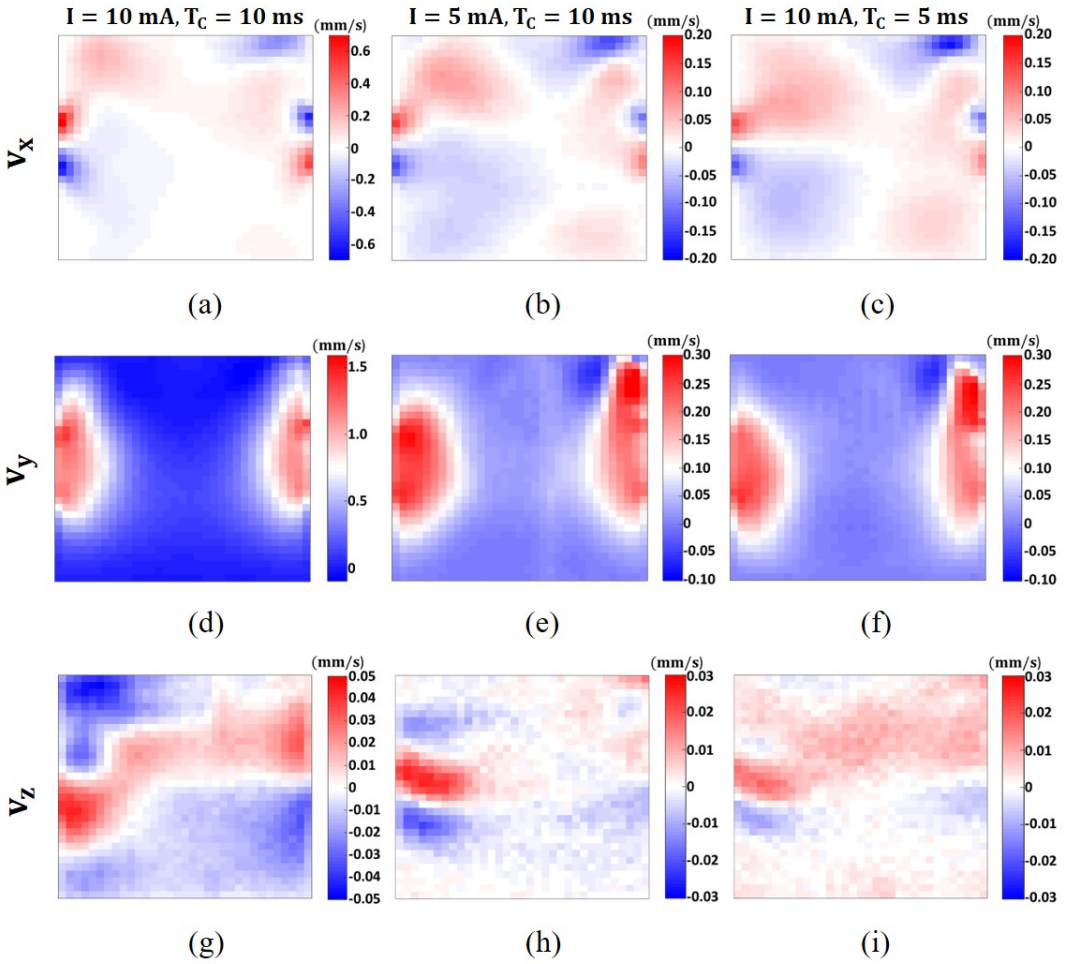

Figure 4.2: Experimentally acquired MHD flow velocity distributions inside the homogeneous cubic phantom: x-component with current injection parameters (a) I=10 mA, T_C=10 ms, (b) I=5 mA, T_C=10 ms, and (c) I=10 mA, T_C=5 ms; y-component with current injection parameters (d) I=10 mA, T_C=10 ms, (e) I=5 mA, T_C=10 ms, and (f) I=10 mA, T_C=5 ms; and z-component with current injection parameters (g) I=10 mA, T_C=10 ms, (h) I=5 mA, T_C=10 ms, and (i) I=10 mA, T_C=5 ms.

As seen from Figures 4.1 and 4.2, the MHD flow velocity magnitudes are significantly larger in the y-direction than the other two orthogonal directions. This is expected since the Lorentz force is formed mainly in the y-direction by the interaction of the B_0 in the z-direction and the current density dominant in the x-direction. Still, in some voxels around the current injection electrodes, substantial v_x and v_z values are observed due to the current dispersion. In Figure 4.1, v_z distributions show a ro-

tational motion but the maximum values are relatively smaller due to the absence of the Lorentz force in this direction. In Figure 4.2, v_z images demonstrate a very small range and are mostly dominated by non-ideal effects.

In fluid dynamics, the discriminator that determines if a flow is either laminar or turbulent is the characteristic dimensionless number called Reynolds number (Re) defined as:

$$Re = \frac{\rho v L}{\mu} \tag{4.1}$$

where ρ is the density, v is the velocity, and μ is the dynamic viscosity of the fluid. L is the characteristic linear dimension or the characteristic length. Conventionally, Re values smaller than 2300 suggest that viscous forces are dominant and the flow is characterized by smooth, constant fluid motion. This is called laminar flow. On the other hand, when Re is larger than 2900, inertial forces become dominant and the flow is classified to be turbulent [69, 70].

The velocity values observed in Figure 4.2 inside the homogeneous cubic phantom with dimension 80×80×80 mm^3 indicates Re values in the order of 10. Hence, the observed flow in Figure 4.2 is clearly laminar which was the assumption during the preparation of the numerical model. The visual consistency between the results in Figures 4.1 and 4.2 also supports this. However, the maximum velocity values are smaller in most of the experimentally acquired distributions. This discrepancy may arise from the inadequacy in the modeling of the complete flow dynamics related to the MHD. For instance, the Lorentz force acts on the ions in the solution, and the solvent shells are affected indirectly [1,8,71]. The cause of the experimentally measured values being lower than the values obtained from the simulations may be attributed to the sensitivity of the MR acquisition to the movement of water molecules alone not to the movement of the ions. These observations put forward that an FE-based numerical model is not optimal to simulate the MHD flow. A computation environment with strong computation capability which can compute the intermolecular interactions between the ions and the water molecules realistically may provide better estimations of the MHD flow under different current injection scenarios.

Another qualitative validation strategy of the MHD flow velocimetry theory is to reconstruct Lorentz force density distribution from the experimentally acquired B_z dis-

tribution. The B_z distribution inside the homogeneous cubic phantom for the I = 10 mA and T_C = 10 ms case is shown in Figure 4.3(a). Moreover, the Lorentz force density distribution obtained from the acquired B_z images with (2.48-2.50) is also demonstrated in Figure 4.3(b-c).

The Lorentz force density distribution in 4.3(b,c) and the MHD flow velocity distribution in Figure 4.2(a,d) visually verifies the claim that the MHD flow inside the medium is caused by the Lorentz force density distribution formed due to the orthogonal current injection and static magnetic field as given in (2.6) and (2.8). In other words, the directions of the MHD flow velocity and Lorentz force density vectors

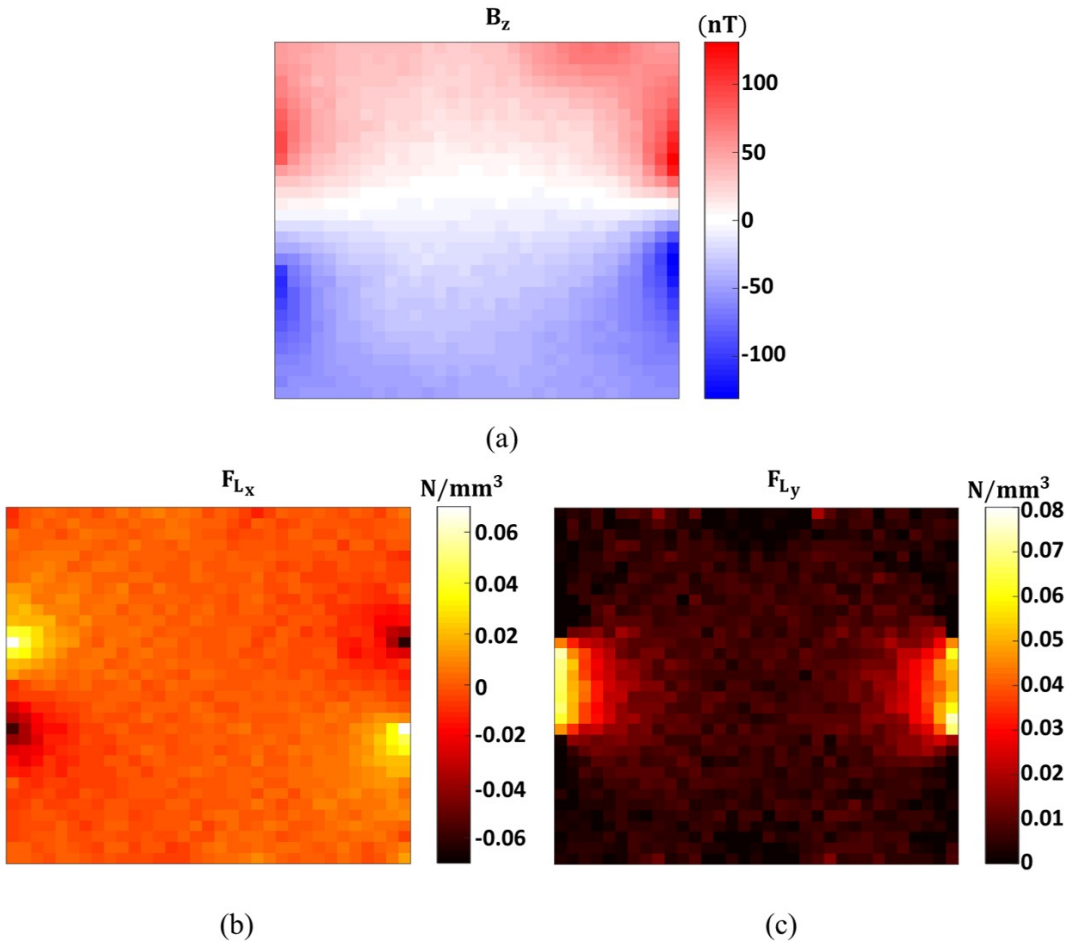

Figure 4.3: (a) Experimentally acquired B_z distribution inside the homogeneous cubic phantom with I = 10 mA, T_C = 10 ms. Corresponding Lorentz force density distribution obtained using (2.50): (b) The x-component, and (c) the y-component.

are similar in all the regions of the imaging slice. Thus, it can be said that the main mechanism that creates a macroscopic flow inside the phantom is the Lorentz force which is the result of the interaction between the orthogonal electrical and magnetic fields. This was claimed before with the insertion of the Lorentz force equation in (2.8) into the Navier-Stokes equations in (2.6) as the main external force component.

4.3 Comparison of the Single and Double Current Pulse Schemes with Horizontal and Vertical Current Injection Patterns

To compare the single and double current pulse schemes described in Section 3.5, MHD flow velocity data is collected both with horizontal and vertical current injections into the homogeneous cylindrical phantom shown in Figure 3.3. During these experiments, the imaging parameters given in Table 3.2 are utilized. Moreover, the image acquisition is conducted both with $\boldsymbol{G}_f^k$ and flow encoding gradient set $\boldsymbol{G}_f^{k^*}$ given in (2.61) and (2.62), respectively.

Figures 4.4 and 4.5 show the MHD velocity distributions of the horizontal current injection case. Similarly, Figures 4.6 and 4.7 show the MHD velocity distributions of the vertical current injection case.

As can be seen from Figures 4.4-4.7, in the homogeneous cylindrical phantom too, the dominant MHD flow is observed in the transversal direction perpendicular to the current injection direction. Furthermore, the most dominant flow is formed near the current injection electrodes where the current density values are highest.

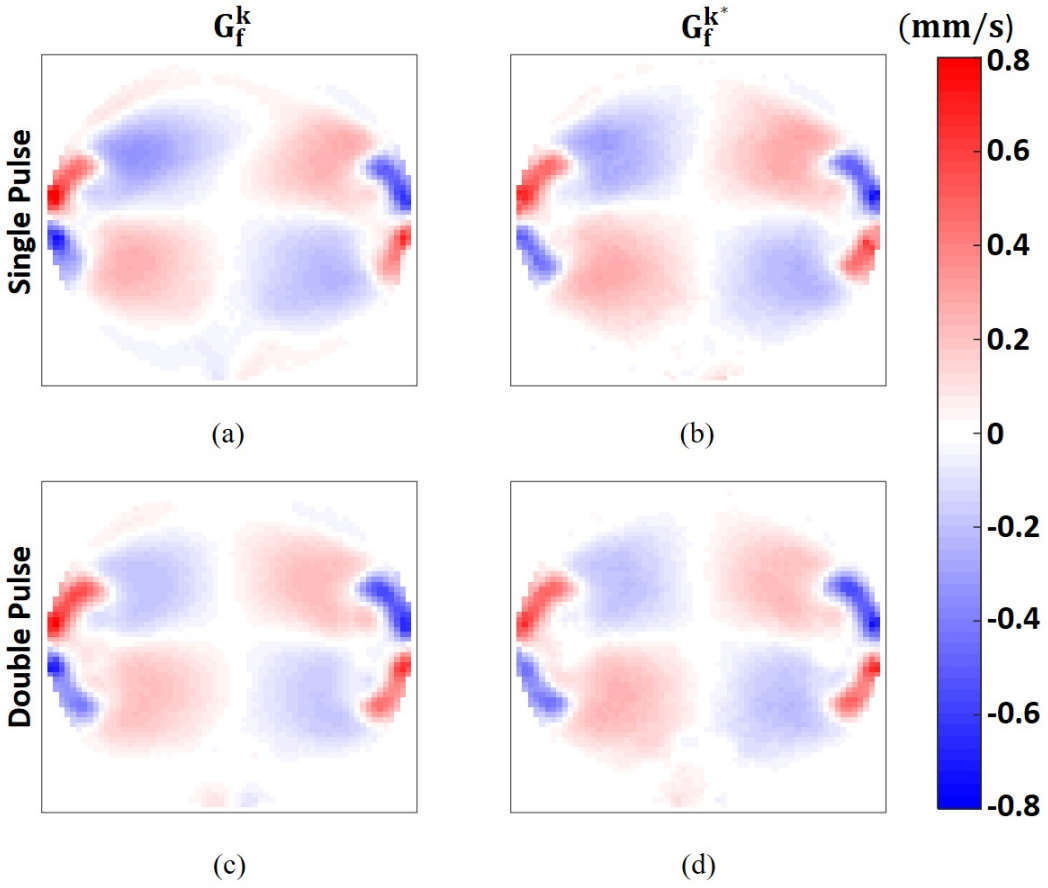

Figure 4.4: Experimentally acquired MHD flow velocity distributions inside the homogeneous cylindrical phantom in the **x**-direction with **horizontal** current injection. (a) With single current pulse and flow encoding gradient set $\boldsymbol{G}_f^k$, (b) with a single current pulse and flow encoding gradient set $\boldsymbol{G}_f^{k^*}$, (c) with double current pulse and flow encoding gradient set $\boldsymbol{G}_f^k$, (d) with double current pulse and flow encoding gradient set $\boldsymbol{G}_f^{k^*}$.

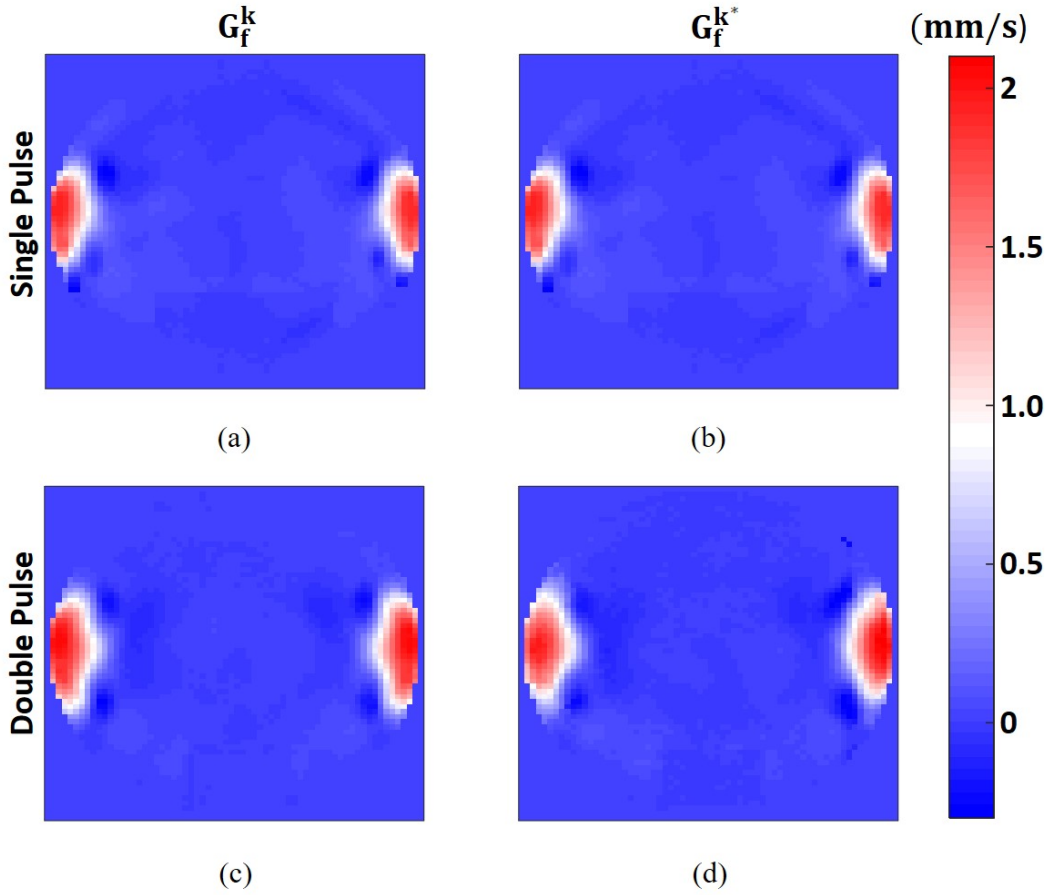

Figure 4.5: Experimentally acquired MHD flow velocity distributions inside the homogeneous cylindrical phantom in the **y**-direction with **horizontal** current injection. (a) With single current pulse and flow encoding gradient set $\boldsymbol{G}_f^k$, (b) with a single current pulse and flow encoding gradient set $\boldsymbol{G}_f^{k^*}$, (c) with double current pulse and flow encoding gradient set $\boldsymbol{G}_f^k$, (d) with double current pulse and flow encoding gradient set $\boldsymbol{G}_f^{k^*}$.

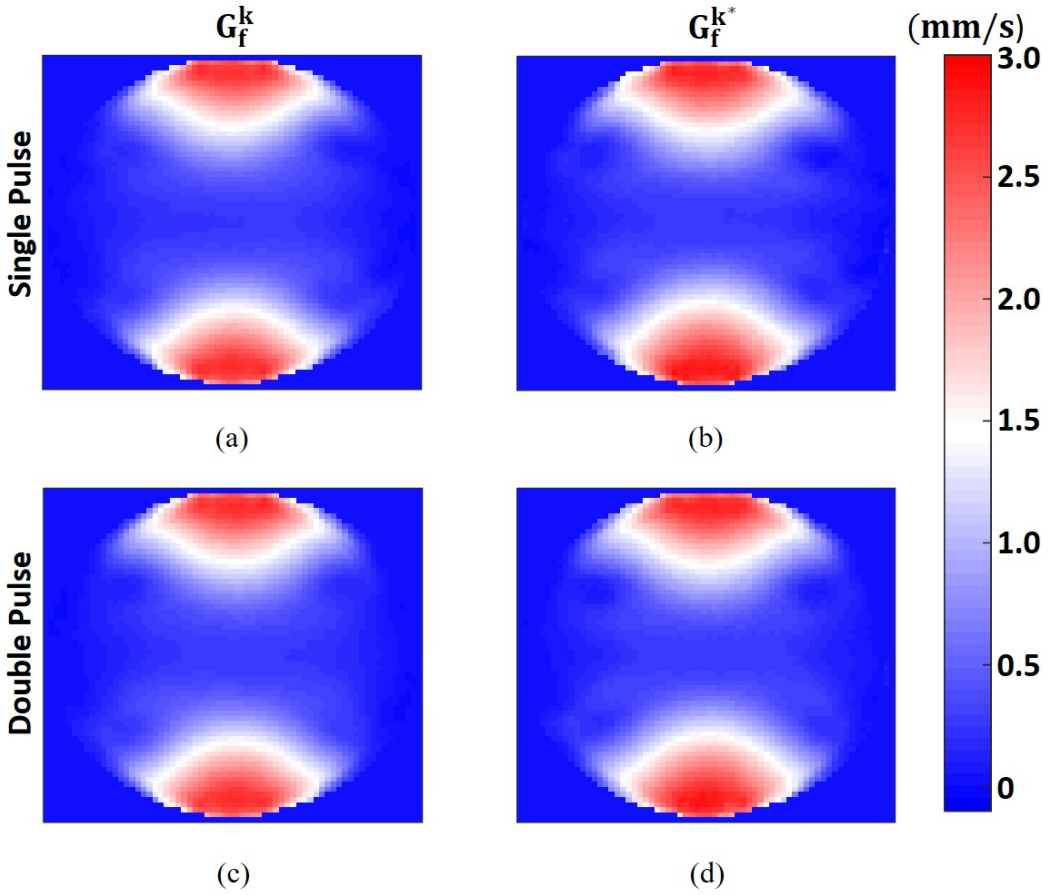

Figure 4.6: Experimentally acquired MHD flow velocity distributions inside the homogeneous cylindrical phantom in the **x**-direction with **vertical** current injection. (a) With single current pulse and flow encoding gradient set $\boldsymbol{G}_f^k$, (b) with a single current pulse and flow encoding gradient set $\boldsymbol{G}_f^{k^*}$, (c) with double current pulse and flow encoding gradient set $\boldsymbol{G}_f^k$, (d) with double current pulse and flow encoding gradient set $\boldsymbol{G}_f^{k^*}$.

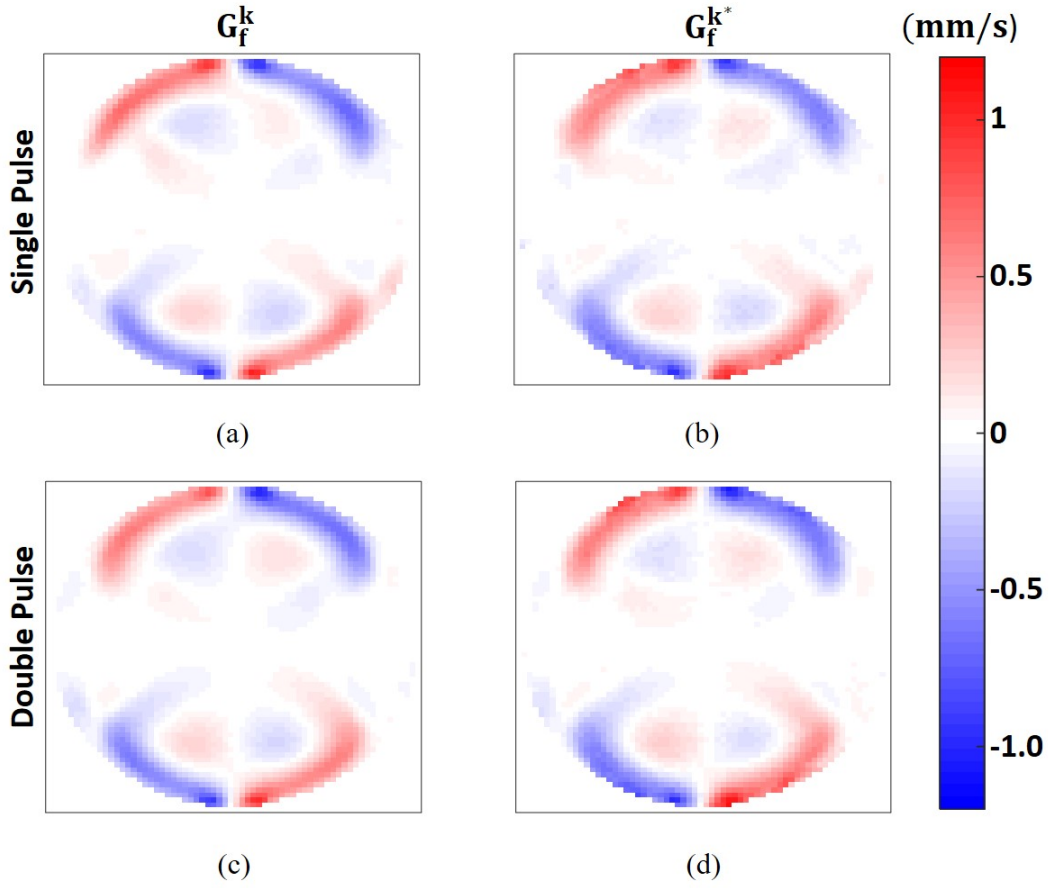

Figure 4.7: Experimentally acquired MHD flow velocity distributions inside the homogeneous cylindrical phantom in the **y**-direction with **vertical** current injection. (a) With single current pulse and flow encoding gradient set $\boldsymbol{G}_f^k$, (b) with a single current pulse and flow encoding gradient set $\boldsymbol{G}_f^{k^*}$, (c) with double current pulse and flow encoding gradient set $\boldsymbol{G}_f^k$, (d) with double current pulse and flow encoding gradient set $\boldsymbol{G}_f^{k^*}$.

To show the numerical similarity of two MHD flow velocity distributions (v_1 and v_2) obtained with the flow encoding gradient sets $\boldsymbol{G}_f^k$ and $\boldsymbol{G}_f^{k^*}$, and single and double pulse schemes, Root Mean Square Error (RMSE) between the two images is computed as:

$$RMSE\ (mm/s) = \sqrt{\frac{1}{N}\sum_{j=1}^{N}(v_1 - v_2)^2} \tag{4.2}$$

where N is the total number of image pixels. The computed values are presented in Tables 4.1-4.4 for different combinations.

Table 4.1: RMSE values between different velocity distributions shown in Figure 4.4 in the **x**-direction obtained with different current injection (single and double pulse) schemes and flow encoding gradient sets ($\boldsymbol{G}_f^k$ and $\boldsymbol{G}_f^{k^*}$) with **horizontal** current injection. Note that half of the table is given since it is a symmetric table by definition.

RMSE (mm/s)	**Single +** $\boldsymbol{G}_f^k$	**Single +** $\boldsymbol{G}_f^{k^*}$	**Double +** $\boldsymbol{G}_f^k$	**Double +** $\boldsymbol{G}_f^{k^*}$
Single + $\boldsymbol{G}_f^k$	0	0.048	0.069	0.075
Single + $\boldsymbol{G}_f^{k^*}$	-	0	0.060	0.056
Double + $\boldsymbol{G}_f^k$	-	-	0	0.033
Double + $\boldsymbol{G}_f^{k^*}$	-	-	-	0

Table 4.2: RMSE values between different velocity distributions shown in Figure 4.5 in the **y**-direction obtained with different current injection (single and double pulse) schemes and flow encoding gradient sets ($\boldsymbol{G}_f^k$ and $\boldsymbol{G}_f^{k^*}$) with **horizontal** current injection. Note that half of the table is given since it is a symmetric table by definition.

RMSE (mm/s)	**Single +** $\boldsymbol{G}_f^k$	**Single +** $\boldsymbol{G}_f^{k^*}$	**Double +** $\boldsymbol{G}_f^k$	**Double +** $\boldsymbol{G}_f^{k^*}$
Single + $\boldsymbol{G}_f^k$	0	0.056	0.130	0.123
Single + $\boldsymbol{G}_f^{k^*}$	-	0	0.112	0.092
Double + $\boldsymbol{G}_f^k$	-	-	0	0.076
Double + $\boldsymbol{G}_f^{k^*}$	-	-	-	0

Table 4.3: RMSE values between different velocity distributions shown in Figure 4.6 in the **x**-direction obtained with different current injection (single and double pulse) schemes and flow encoding gradient sets ($\boldsymbol{G}_f^k$ and $\boldsymbol{G}_f^{k^*}$) with **vertical** current injection. Note that half of the table is given since it is a symmetric table by definition.

RMSE (mm/s)	**Single +** $\boldsymbol{G}_f^k$	**Single +** $\boldsymbol{G}_f^{k^*}$	**Double +** $\boldsymbol{G}_f^k$	**Double +** $\boldsymbol{G}_f^{k^*}$
Single + $\boldsymbol{G}_f^k$	0	0.092	0.044	0.099
Single + $\boldsymbol{G}_f^{k^*}$	-	0	0.084	0.048
Double + $\boldsymbol{G}_f^k$	-	-	0	0.081
Double + $\boldsymbol{G}_f^{k^*}$	-	-	-	0

Table 4.4: RMSE values between different velocity distributions shown in Figure 4.7 in the **y**-direction obtained with different current injection (single and double pulse) schemes and flow encoding gradient sets ($\boldsymbol{G}_f^k$ and $\boldsymbol{G}_f^{k^*}$) with **vertical** current injection. Note that half of the table is given since it is a symmetric table by definition.

RMSE (mm/s)	**Single +** $\boldsymbol{G}_f^k$	**Single +** $\boldsymbol{G}_f^{k^*}$	**Double +** $\boldsymbol{G}_f^k$	**Double +** $\boldsymbol{G}_f^{k^*}$
Single + $\boldsymbol{G}_f^k$	0	0.053	0.054	0.067
Single + $\boldsymbol{G}_f^{k^*}$	-	0	0.059	0.046
Double + $\boldsymbol{G}_f^k$	-	-	0	0.053
Double + $\boldsymbol{G}_f^{k^*}$	-	-	-	0

With the qualitative evaluation of Figures 4.4-4.7 and quantitative analysis of Tables 4.1-4.4, one can see that the utilization of double current injection pulses instead of one or employing flow encoding gradient set $\boldsymbol{G}_f^{k^*}$ instead of $\boldsymbol{G}_f^k$ cause no significant change at the measured MHD velocity distributions.

On the other hand, the MHD flow velocity distributions inside the homogeneous cylindrical phantom for horizontal and vertical current injections are quite different. There is approximately a 1.5 times higher flow in both directions when the vertical current injection is applied. This is an interesting observation since everything is symmetric inside the phantom and exactly the same current is injected for both cases. As can be observed from the Navier-Stokes equations given in (2.6) and (2.7), the dependence of the fluid flow on the external forces is highly nonlinear and most of the time very difficult to foresee. The only possible major difference between the two current injection patterns is the effect of gravity. The major component of the MHD flow is in the vertical direction for horizontal current injection. The gravity itself (or the frictional forces between fluid and phantom such as adhesion) may be acting as an opponent to the Lorentz force for the horizontal current injection. Since the major component of the MHD flow is in the horizontal direction for vertical current injection, these forces may not be so effective.

In Figures 4.8 and 4.9, the velocity distributions in Figures 4.4-4.7 are demonstrated as vector plots. To increase the intelligibility, the spatial resolution of the images is

increased to 4 mm $\times$ 4 mm.

Figures 4.8 and 4.9 shows the main MHD flow directions inside the phantom. As can be inferred from these Figures, two fundamental conditions that determine the MHD flow directions are the geometry of the medium and the current injection patterns. Hence, any inhomogeneity inside the medium would disturb these flow patterns because of the fact that MHD flow velocity distribution has zero divergence which means the continuity equation must be satisfied everywhere. Moreover, each current injection pattern would create its own unique MHD flow patterns.

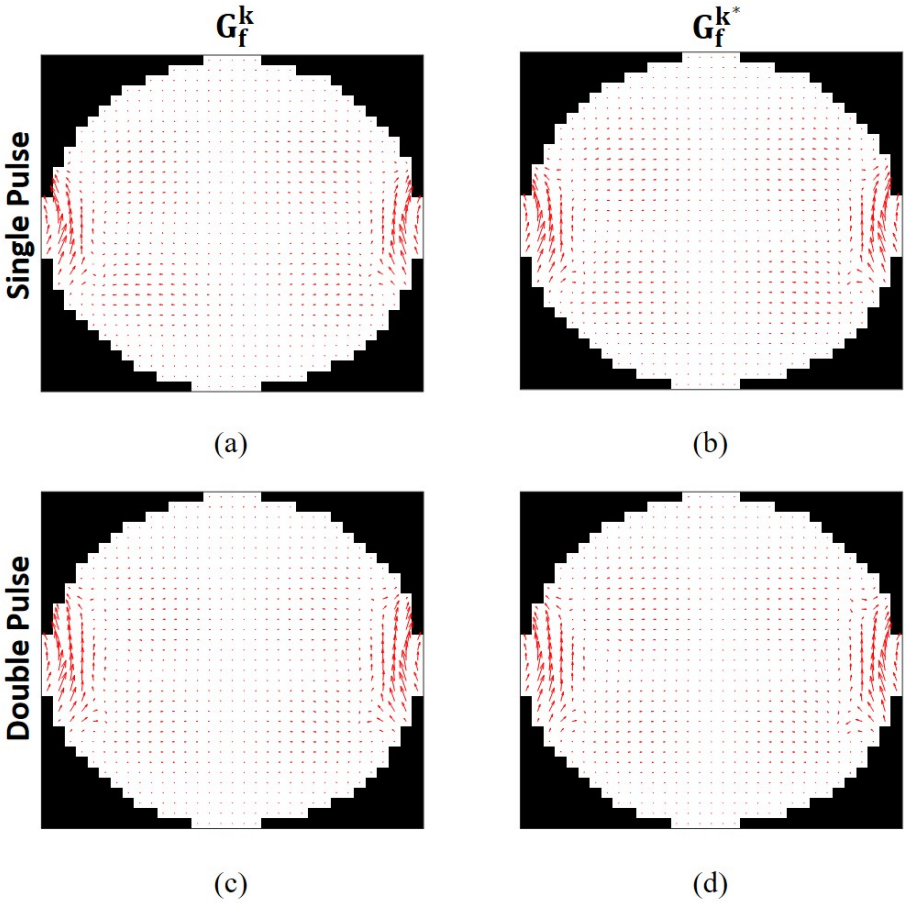

Figure 4.8: Vector plot distributions of the MHD flow velocity distributions presented in Figures 4.4 and 4.5 for **horizontal** current injection. (a) With single current pulse and flow encoding gradient set $\boldsymbol{G}_f^k$, (b) with a **single** current pulse and flow encoding gradient set $\boldsymbol{G}_f^{k^*}$, (c) with double current pulse and flow encoding gradient set $\boldsymbol{G}_f^k$, (d) with **double** current pulse and flow encoding gradient set $\boldsymbol{G}_f^{k^*}$.

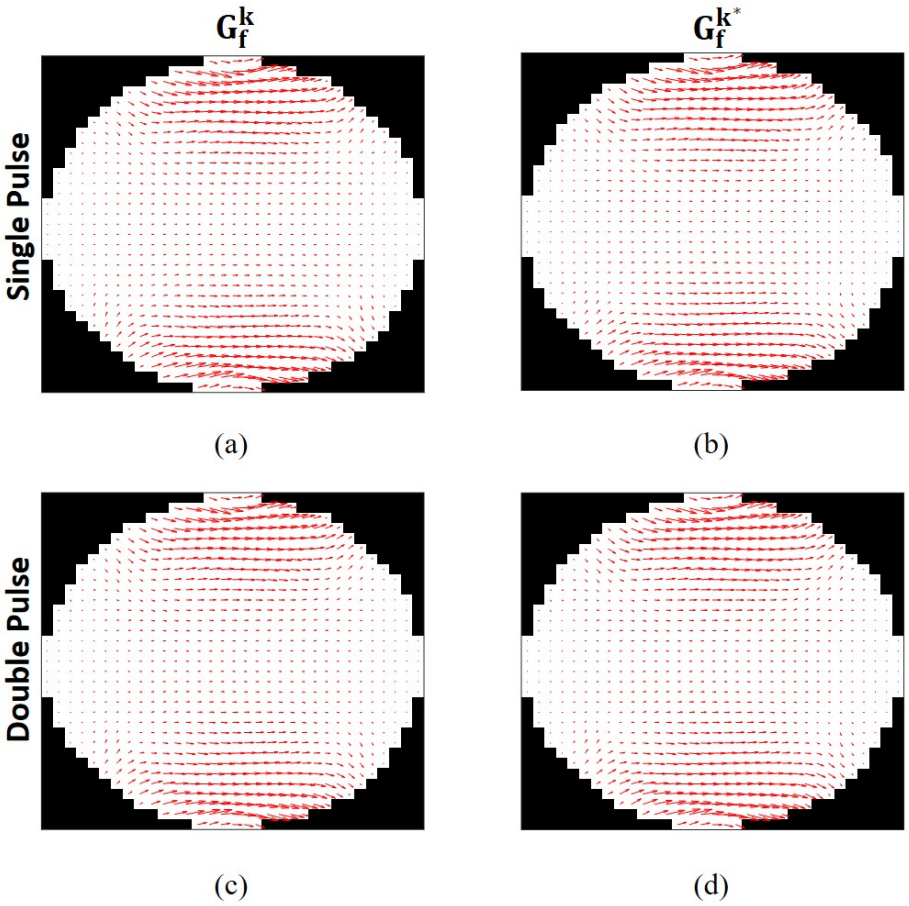

Figure 4.9: Vector plot distributions of the MHD flow velocity distributions presented in Figures 4.6 and 4.7 for **vertical** current injection. (a) With single current pulse and flow encoding gradient set $\boldsymbol{G}_f^k$, (b) with a **single** current pulse and flow encoding gradient set $\boldsymbol{G}_f^{k^*}$, (c) with double current pulse and flow encoding gradient set $\boldsymbol{G}_f^k$, (d) with **double** current pulse and flow encoding gradient set $\boldsymbol{G}_f^{k^*}$.

4.4 Experimental and Analytical Results of the MHD Flow Sensitivity Analysis

To evaluate the methods developed in Section 2.3, experimental data is acquired with the homogeneous cylindrical phantom. Moreover, analytical results are produced to discuss the effectiveness of the developed strategies.

4.4.1 Empirical Estimation of the Relations between the Current Injection Parameters and SNR of the MHD Flow Velocity Images

In order to empirically estimate the dependency of the MHD flow formation on the current injection parameters, MHD flow data is collected with either sweeping I or T_C. The experiments are conducted with the homogeneous cylindrical phantom shown in Figure 3.3 and the imaging parameters given in Table 3.2. Since B_z data is not required in this analysis, the double current pulse scheme is employed for current injection to decrease T_E to 65 ms. Moreover, all experiments are conducted with the horizontal current injection pattern. Later, empirically estimated SNR values of the MHD flow velocity images are fitted into analytical functions as explained in (2.32), (2.37), and (2.40).

Note that during the image reconstruction of the experimental results obtained with the flow encoding gradient set $\boldsymbol{G}_f^{k^*}$ presented in this section, only the difference based components in (2.64) are utilized. For example, v_x distribution is obtained from the difference of the phase images acquired by applying $\boldsymbol{G}_f^{k^1}$ and $\boldsymbol{G}_f^{k^2}$. As mentioned before, v_x distribution can also be obtained from the summation of the phase images acquired by applying $\boldsymbol{G}_f^{k^3}$ and $\boldsymbol{G}_f^{k^4}$. Therefore, the SNR of the v_x distribution can be increased by a factor of $\sqrt{2}$ by averaging these two independent reconstructions. However, this property of the flow encoding gradient set $\boldsymbol{G}_f^{k^*}$ is not utilized here. The purpose is to examine the effect of the b-value on the MHD flow velocity images by comparing the SNR values of the same distributions obtained with the flow encoding gradient sets $\boldsymbol{G}_f^{k}$ and $\boldsymbol{G}_f^{k^*}$ by identical image reconstruction.

4.4.1.1 Empirical Estimation of the dependency of the MHD Flow on I

To observe the sole effect of changing I on the SNR of the MHD flow velocity images, I is swept between 2-10 mA amplitudes with 2 mA steps while keeping T_C = 10 ms, and the other imaging parameters as given in Table 3.2. The obtained MHD flow velocity distributions in x- and y-directions are shown in Figures 4.10 and 4.11, respectively. Moreover, for more detailed examination, some profiles of these distributions are presented in Figures 4.12 and 4.13.

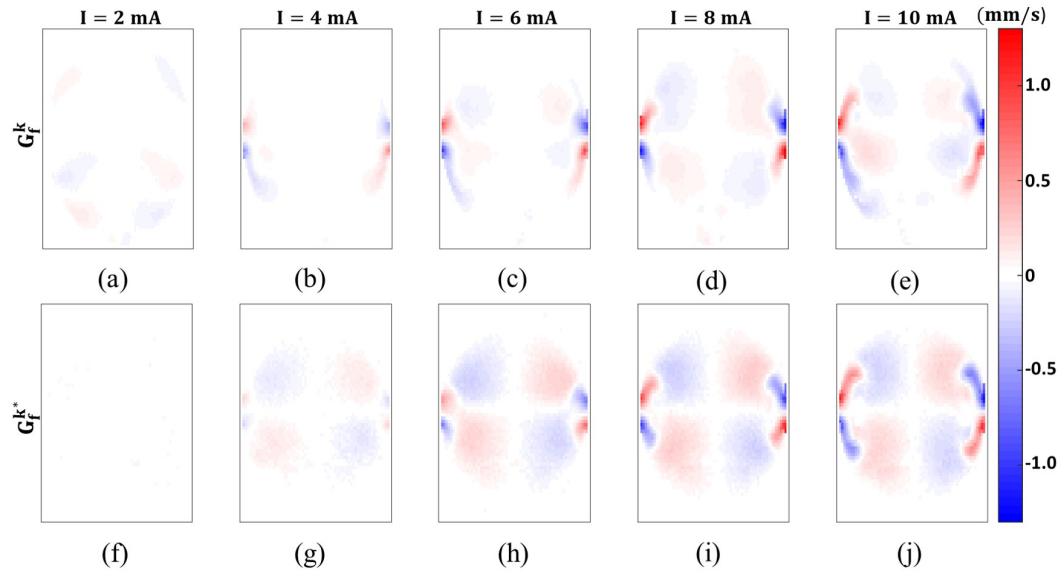

Figure 4.10: Experimentally acquired MHD flow velocity distributions in the **x**-direction. Obtained with the flow encoding gradient set $\boldsymbol{G}_f^k$ with I = (a) 2 mA, (b) 4 mA, (c) 6 mA, (d) 8 mA, (e) 10 mA; and obtained with the flow encoding gradient set $\boldsymbol{G}_f^{k^*}$ with I = (f) 2 mA, (g) 4 mA, (h) 6 mA, (i) 8 mA, (j) 10 mA.

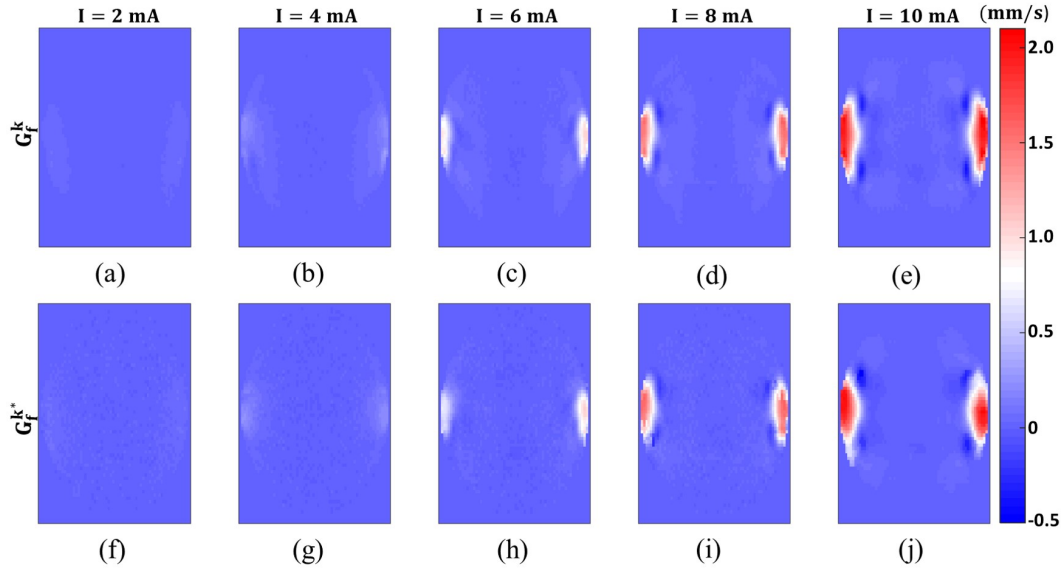

Figure 4.11: Experimentally acquired MHD flow velocity distributions in the **y**-direction. Obtained with the flow encoding gradient set $\boldsymbol{G}_f^k$ with I = (a) 2 mA, (b) 4 mA, (c) 6 mA, (d) 8 mA, (e) 10 mA; and obtained with the flow encoding gradient set $\boldsymbol{G}_f^{k^*}$ with I = (f) 2 mA, (g) 4 mA, (h) 6 mA, (i) 8 mA, (j) 10 mA.

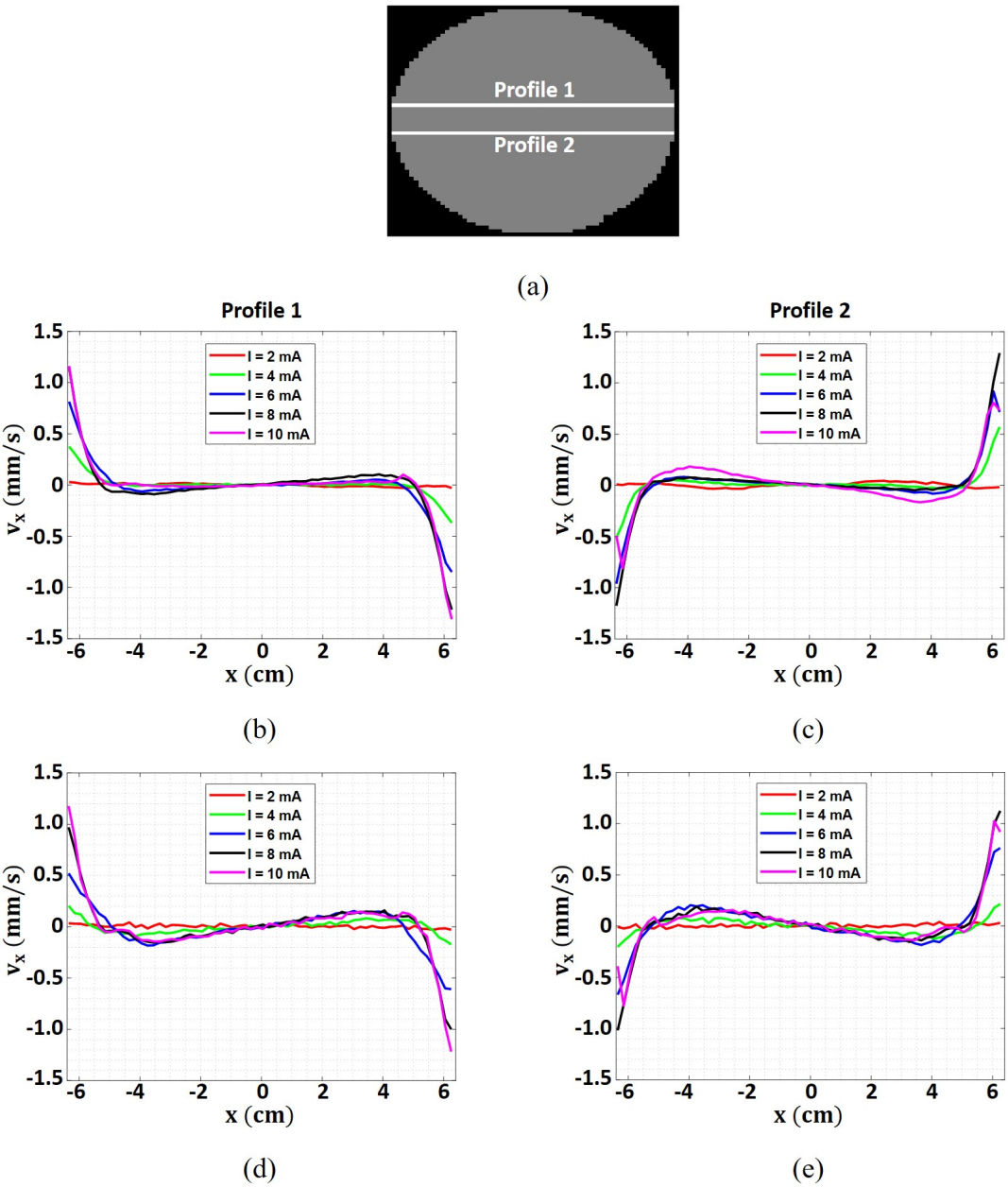

Figure 4.12: (a) The profile locations inside the homogeneous cylindrical phantom. Experimentally acquired MHD flow velocity distributions in **x**-direction obtained with the flow encoding gradient set $\boldsymbol{G}_f^k$ along the (b) Profile 1 and (c) Profile 2; obtained with the flow encoding gradient set $\boldsymbol{G}_f^{k*}$ along the (d) Profile 1 and (e) Profile 2.

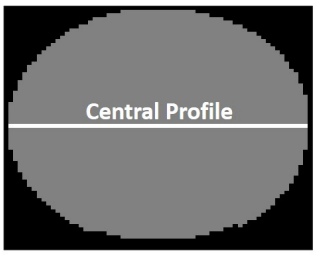

(a)

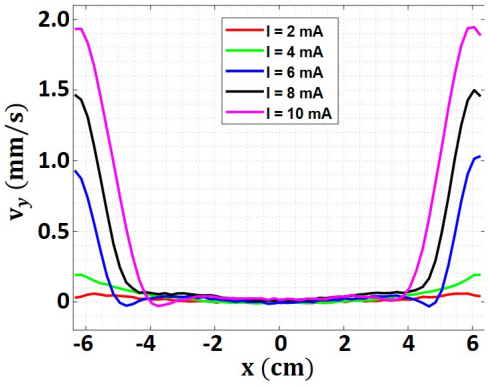

(b)

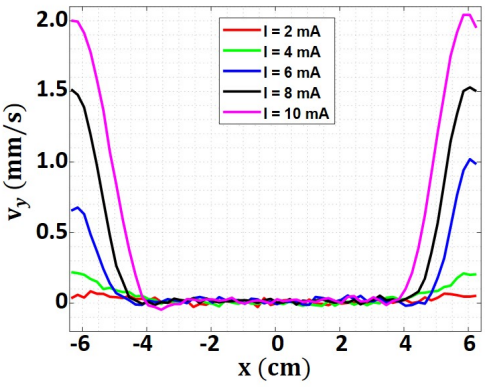

(c)

Figure 4.13: (a) The profile location inside the homogeneous cylindrical phantom. Experimentally acquired MHD flow velocity distributions in **y**-direction obtained with (b) the flow encoding gradient set $\boldsymbol{G}_f^k$ and (c) the flow encoding gradient set $\boldsymbol{G}_f^{k*}$ along the Central Profile.

Finally, the empirically estimated MHD flow velocity signal RMS, noise level, and corresponding SNR values as explained in Section 2.3.3 are demonstrated in Figure 4.14 as a function of I.

One important observation related to Figure 4.14 is that MHD flow velocity increases with the injected current amplitude as expected. Moreover, noise levels of different distributions under different injected current amplitudes do not change and stay approximately flat. This was expected by (2.19) with the assumption of the noise level of the MHD flow velocity images depends on the magnitude image SNR values. Since current injection does not affect the magnitude images, this result is meaningful. Moreover, the noise levels in the MHD flow in x- and y-directions are the same

for the same flow encoding gradient sets. This shows that noise is independent of the signal distribution which validates the previous SNR derivation in Section 2.3.3.

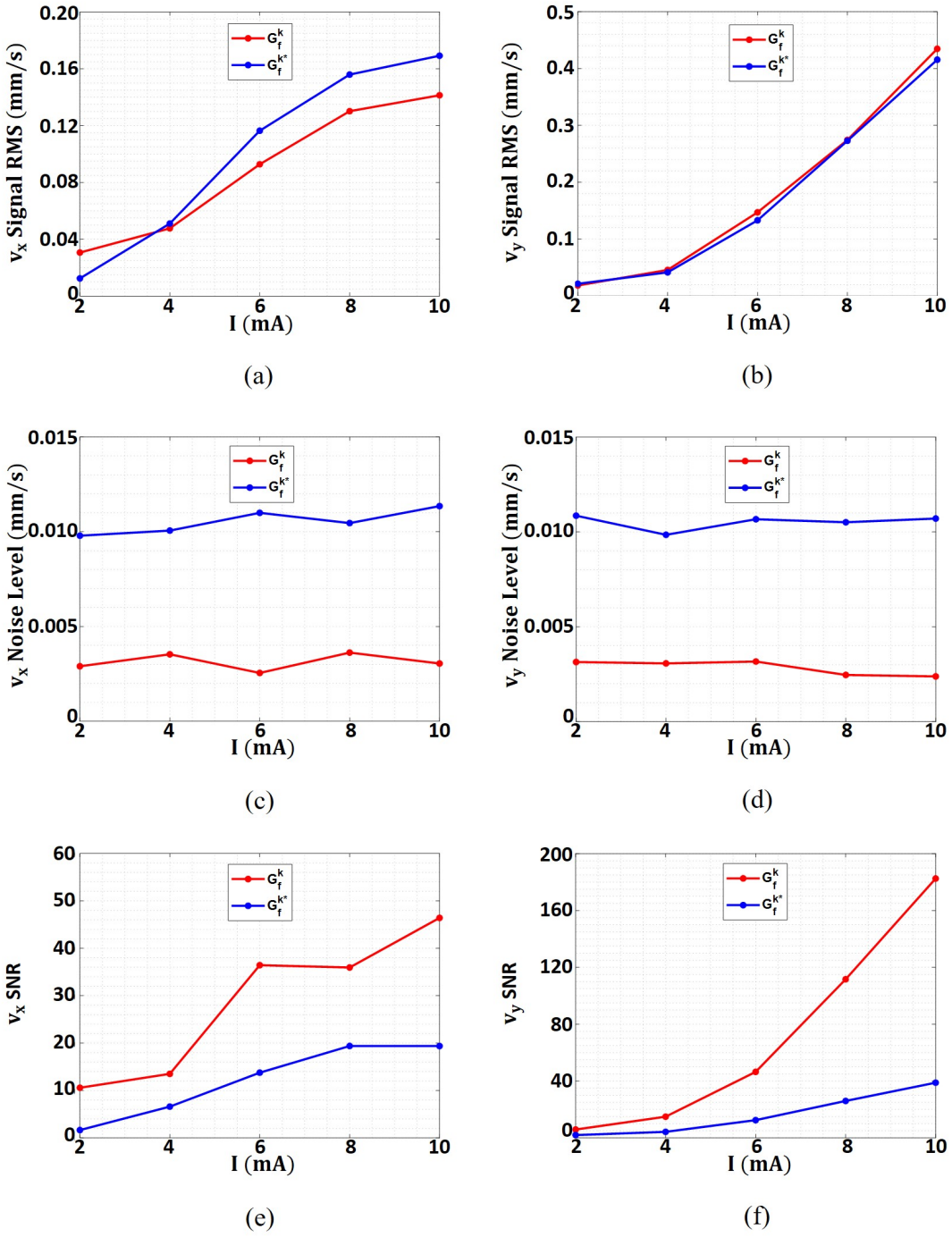

Figure 4.14: The RMS values of the experimentally acquired MHD flow velocity distributions in (a) **x**-direction, (b) **y**-direction; noise levels in (c) **x**-direction, (d) **y**-direction; SNR in (e) **x**-direction, (f) **y**-direction.

Another observation is that the MHD flow velocity signals increase in both x- and y-direction directions but with different dependencies on the injected current amplitude. In general, the flow velocity in the y-direction increases more rapidly. Note that with horizontal current injection, the most dominant component of the Lorentz force and consequently the MHD flow appears in the y-direction. Such a drastic increase in the dominant direction is very important and as expected it is highly nonlinear.

The signal values obtained with the two flow encoding gradient sets are approximately the same, consistent with the results of the previous chapter. However, the noise levels of the MHD flow velocity images obtained with the flow encoding gradient set $\boldsymbol{G}_f^{k*}$ are approximately 3 times higher than the ones obtained with the flow encoding gradient set $\boldsymbol{G}_f^k$. This can be explained via (2.19). To estimate the SNR value of the images using (2.19), it is necessary to substitute $\boldsymbol{g}_f^k = \boldsymbol{G}_f^k$ for the flow encoding gradient set $\boldsymbol{G}_f^k$ or $\boldsymbol{g}_f^k = \frac{\boldsymbol{G}_f^{k*}}{\sqrt{2}}$ for the flow encoding gradient set $\boldsymbol{G}_f^{k*}$ (Note that $\boldsymbol{G}_f^{k*}$ are not normalized). Hence, the $\frac{1}{\sqrt{2}}$ coefficients of the gradients are absorbed by the b-value and the effective b-value of the flow encoding gradient set $\boldsymbol{G}_f^{k*}$ becomes twice the b-value of the flow encoding gradient set $\boldsymbol{G}_f^k$. With isotropic medium, the diffusion tensor becomes a scalar diffusion coefficient, and $\boldsymbol{g}_f^{kT}\boldsymbol{g}_f^k$ becomes 1. Thus, the ratio of the SNR of the MHD flow velocity distributions obtained with different flow encoding gradient sets can be expressed as:

$$\frac{SNR_{\boldsymbol{v},MHD}(\boldsymbol{g}_f^k = \boldsymbol{G}_f^k)}{SNR_{\boldsymbol{v},MHD}(\boldsymbol{g}_f^k = \frac{\boldsymbol{G}_f^{k*}}{\sqrt{2}})} = e^{bD} \tag{4.3}$$

With the imaging parameters given in Table 3.2, the b-value can be computed as 504 s/mm^2 using (2.4). Moreover, if the diffusion coefficient of water at room temperature (2.23×10^{-3} mm^2/s) is inserted into D, e^{bD} becomes 3.07 which validates the difference in the noise levels.

Finally, to determine the dependence of $SNR_{\boldsymbol{v},MHD}$ on I analytically, a curve fitting algorithm is utilized to fit the SNR plots presented in Figure 4.14 to a curve in the form $a_2 I^n$ as mentioned in (2.37) by estimating the fitting parameters a_2 and n. For the fitting, the Levenberg–Marquardt algorithm [72] is utilized to minimize the least absolute residuals and the results are presented in Table 4.5.

Table 4.5: Estimated fitting parameters for the Sensitivity Analysis of the MHD flow velocity distributions on I.

	v_x with $\boldsymbol{G}_f^k$	v_x with $\boldsymbol{G}_f^{k*}$	v_y with $\boldsymbol{G}_f^k$	v_y with $\boldsymbol{G}_f^{k*}$
a_2	5.60	1.29	0.38	0.23
n	0.91	1.18	2.68	2.22

As can be seen from Table 4.5, the SNR of the MHD flow velocity images depends on the increasing I almost linearly ($n \approx 1.05$) in the non-dominant (x-) flow direction while increases with an approximate power of 2.45 ($n \approx 2.45$) in the dominant (y-) direction. The main focus of this study is the dominant flow direction, consequently, further analysis will be based on the parameters estimated for the dominant direction. The a_2-coefficients are not important when the interest is to find the ratio of the SNR values of the two MHD flow velocity distributions obtained with different injected current amplitudes. The difference of these a_2-coefficients is related to the previously explained phenomenon of different noise levels obtained with the different flow encoding gradient sets which have different b-values.

4.4.1.2 Empirical Estimation of the dependency of the MHD Flow on T_C

To observe the sole effect of changing T_C on the SNR of the MHD flow velocity images, T_C is swept between 2-10 ms with 2 ms steps while keeping I = 10 mA, and the other imaging parameters as given in Table 3.2. The obtained MHD flow velocity distributions in x- and y-directions are shown in Figures 4.15 and 4.16, respectively.

Moreover, for more detailed examination, some profiles of these distributions are presented in Figures 4.17 and 4.18.

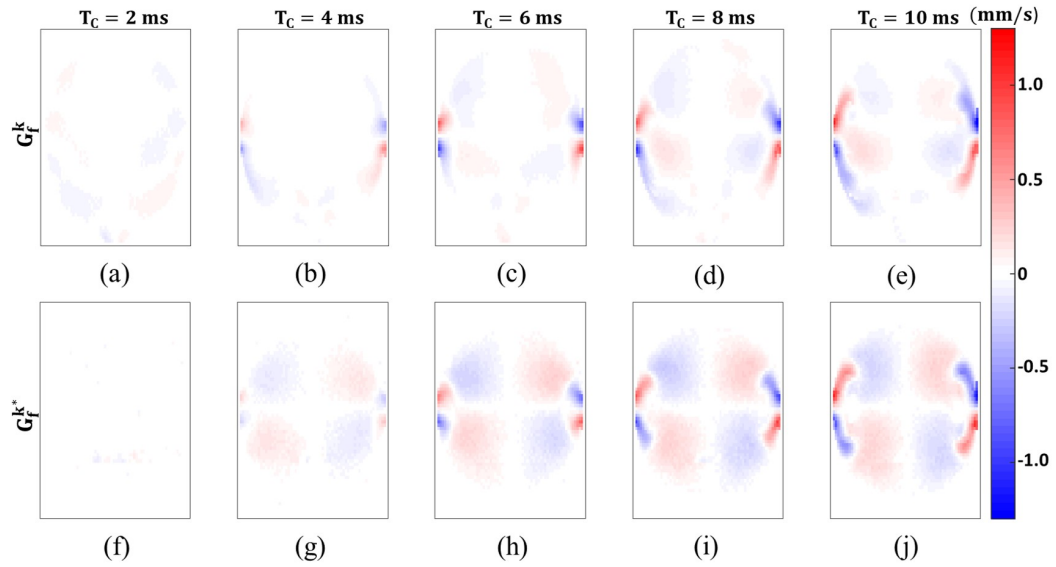

Figure 4.15: Experimentally acquired MHD flow velocity distributions in the **x**-direction. Obtained with the flow encoding gradient set $\boldsymbol{G}_f^k$ with T_C = (a) 2 ms, (b) 4 ms, (c) 6 ms, (d) 8 ms, (e) 10 ms; and obtained with the flow encoding gradient set $\boldsymbol{G}_f^{k^*}$ with T_C = (f) 2 ms, (g) 4 ms, (h) 6 ms, (i) 8 ms, (j) 10 ms.

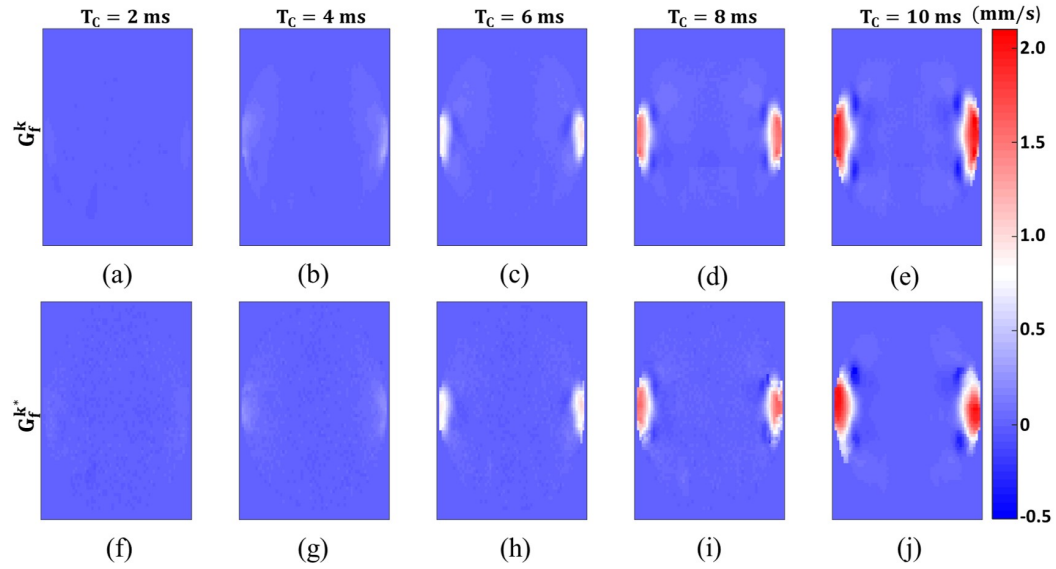

Figure 4.16: Experimentally acquired MHD flow velocity distributions in the **y**-direction. Obtained with the flow encoding gradient set $\boldsymbol{G}_f^k$ with T_C = (a) 2 ms, (b) 4 ms, (c) 6 ms, (d) 8 ms, (e) 10 ms; and obtained with the flow encoding gradient set $\boldsymbol{G}_f^{k^*}$ with T_C = (f) 2 ms, (g) 4 ms, (h) 6 ms, (i) 8 ms, (j) 10 ms.

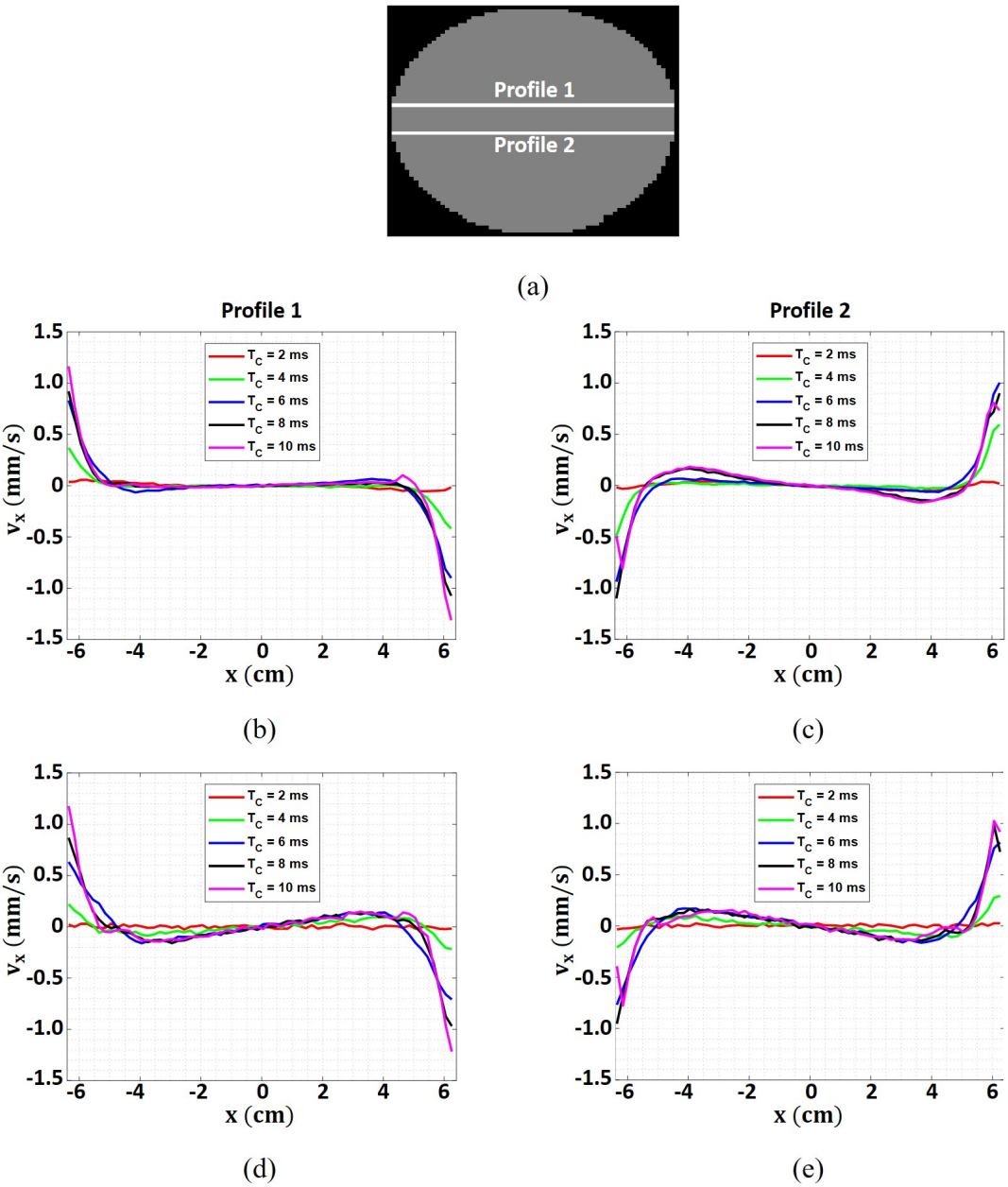

Figure 4.17: (a) The profile locations inside the homogeneous cylindrical phantom. Experimentally acquired MHD flow velocity distributions in **x**-direction obtained with the flow encoding gradient set $\boldsymbol{G}_f^k$ along the (b) Profile 1 and (c) Profile 2; obtained with the flow encoding gradient set $\boldsymbol{G}_f^{k*}$ along the (d) Profile 1 and (e) Profile 2.

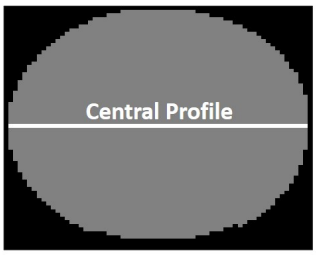

(a)

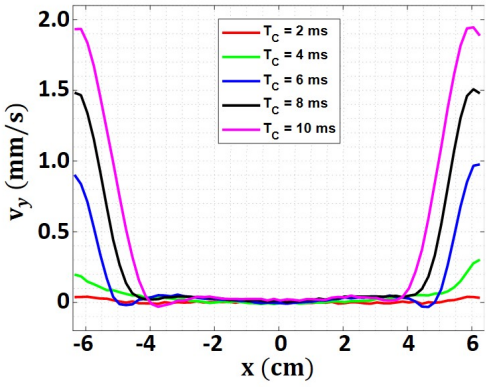

(b)

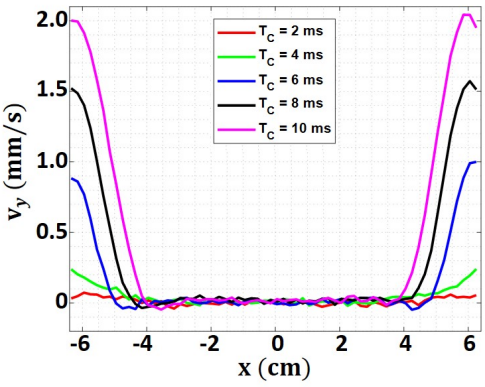

(c)

Figure 4.18: (a) The profile location inside the homogeneous cylindrical phantom. Experimentally acquired MHD flow velocity distributions in **y**-direction obtained with (b) the flow encoding gradient set $\boldsymbol{G}_f^k$ and (c) the flow encoding gradient set $\boldsymbol{G}_f^{k*}$ along the Central Profile.

The empirically estimated MHD flow velocity signal RMS, noise level, and corresponding SNR values as explained in Section 2.3.3 are demonstrated in Figure 4.19 as a function of T_C.

The dependency of the MHD flow velocity distributions on T_C is almost identical to the dependency on I. Hence, all the discussions made related to I dependency are also valid for T_C dependency as well.

Again, to determine the dependency of $SNR_{\boldsymbol{v},MHD}$ on I analytically, a curve fitting to a curve in the form $a_1 I^m$ as mentioned in (2.32) is conducted to estimate the fitting parameters a_1 and m. The results are presented in Table 4.6 for the SNR plots presented in Figure 4.19.

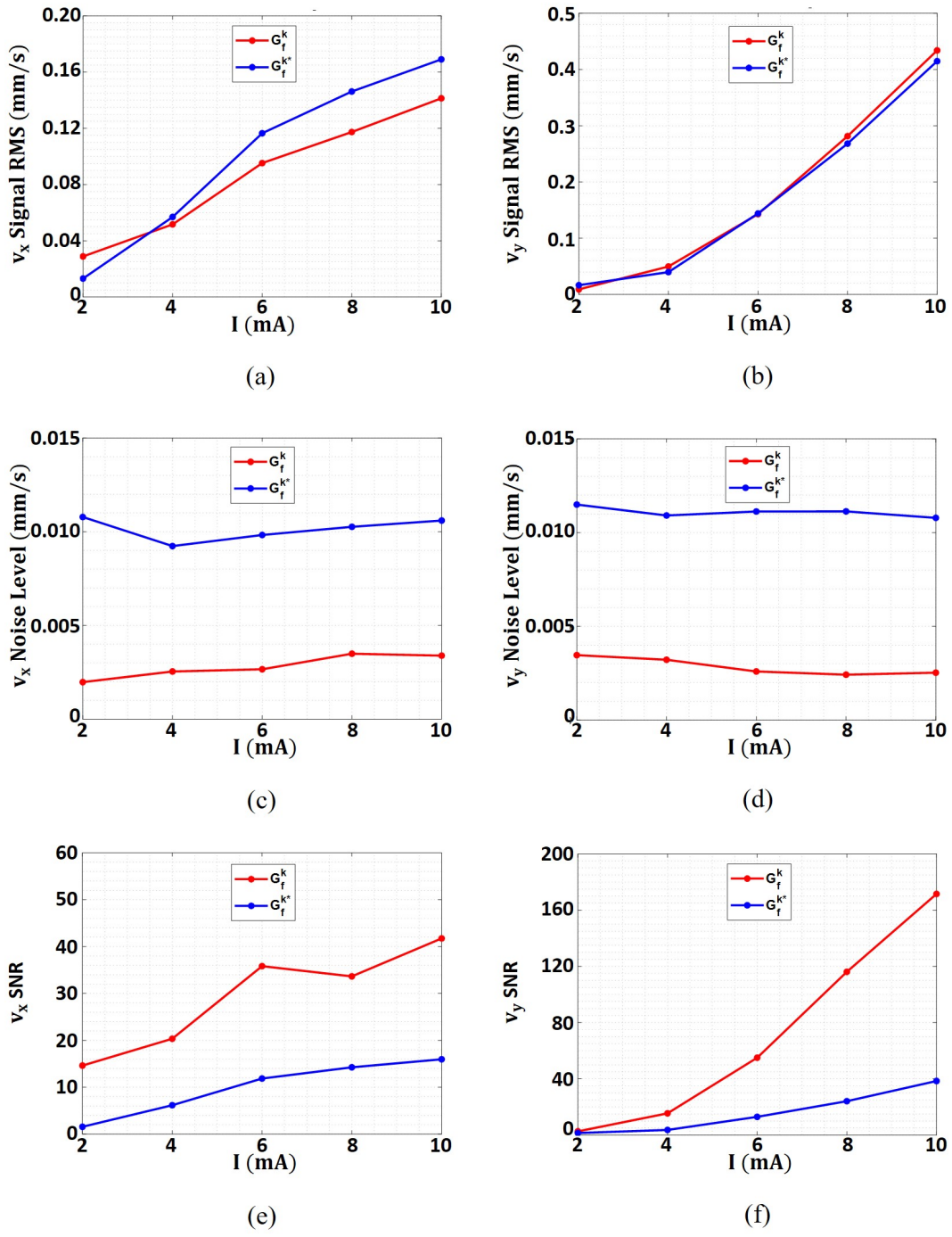

Figure 4.19: The RMS values of the experimentally acquired MHD flow velocity distributions in (a) **x**-direction, (b) **y**-direction; noise level in (c) **x**-direction, (d) **y**-direction; SNR in (e) **x**-direction, (f) **y**-direction.

Table 4.6: Estimated fitting parameters for the Sensitivity Analysis of the MHD flow velocity distributions on T_C.

	v_x with $\boldsymbol{G}_f^k$	v_x with $\boldsymbol{G}_f^{k*}$	v_y with $\boldsymbol{G}_f^k$	v_y with $\boldsymbol{G}_f^{k*}$
a_1	9.30	1.36	1.02	0.28
m	0.65	1.09	2.22	2.13

The fitting parameters behave very similar to the fitting parameters in Table 4.5. Here, it is seen that the SNR of the MHD flow in the dominant (y-) direction depends on the injected current duration with an approximate power of 2.17 ($m \approx 2.17$).

As can be understood from the results above, the effect of I and T_C on the SNR of the MHD flow velocity distributions are almost identical. Hence, instead of treating them as two separate parameters, they can be merged into a single parameter that directly affects the SNR of the MHD flow velocity images with an approximate power of $m \approx 2.3$ for the flow in the dominant direction. Hence, $S_{\boldsymbol{v},MHD}(I, T_C)$ can be considered to be proportional to the following quantity:

$$S_{\boldsymbol{v},MHD}(I, T_C) \sim (IT_C)^{2.3} \tag{4.4}$$

It should be noted that this proportionality is valid for the MHD flow in the dominant flow direction which is the perpendicular direction to both the current injection direction and the static magnetic field of the MR scanner. If the information of the MHD flow in any direction is needed (perpendicular to z-direction), by the careful arrangement of the current injection pattern, the direction of interest can be made the dominant flow direction. Hence, the analysis conducted can be employed. Another important issue is that the analysis is conducted in a homogeneous fluid medium with cylindrical boundaries. With different boundary geometry and possible inhomogeneities, it is logical to expect variations from the analysis above.

One important observation here is that the relation between the current injection parameters and the MHD flow velocity signals is nonlinear. This nonlinearity can be better understood considering the Navier-Stokes equation in (2.6). If we think $\boldsymbol{F}_L$ in this equation as the input parameter which is dependent on the current injection pa-

rameters and $\boldsymbol{v}$ as the output parameter, the nonlinearity becomes obvious. However, the strength of the nonlinearity (the power in (4.4)) depends strongly on the medium and current injection geometry as mentioned.

The effective quantity in (4.4) is the area under the injected current curve. Hence, the analysis can be generalized to any pulse shape. As long as the area under the curve stays the same, the corresponding MHD flow formed inside the medium is expected to be the same as well.

Furthermore, in (3.4), it was derived that the optimum value of T_C can be found as mT_2 which is approximately 2.2$\times$500 ms = 1.1 s. This is an inapplicable value because of the constraint in (2.20). The reason such a high value is suggested by (3.4) is that it was derived assuming the function fitted in (2.32) will be valid for the T_C interval that (3.4) outputs. However, the fitting interval (2-10 ms) is much smaller than 1.1 s, and most probably the MHD flow velocity magnitude would saturate much before T_C reaches that value. Hence, it can be concluded that (3.4) is a much more suitable strategy for media with low T_2.

On the other hand, instead of utilizing (3.4), if available, choosing the T_C value where MHD flow velocity saturates is much more practical for media with high T_2. If it is not available, T_C can be chosen empirically based on the T_2 value of the medium.

4.4.2 Analytical and Experimental Validations of the Derived Relations between the Flow Encoding Parameters and the SNR of the MHD Flow Velocity Images

As stated in Section 2.3.2.1, the flow encoding parameters affect the SNR of the MHD flow velocity images with two different mechanisms. Firstly, they affect the noise level of the measured phase images since the measured MR signal magnitude is weighted by the diffusion with the tuning parameter b-value which is purely dependent on the flow encoding parameters as given in (2.3) and (2.4). Hence, the noise level of the MHD flow velocity images is non-linearly and positively proportional to the b-value. This phenomenon is also shown experimentally in (4.3).

Secondly, the MR phase that accumulates due to the MHD flow is linearly propor-

tional to the product of the flow encoding parameters as given in (2.11). Since the MHD flow velocity images are reconstructed using (2.12), the noise level of the reconstructed images is inversely proportional to the product of the flow encoding parameters. For instance, if the same velocity distribution is measured with two different flow encoding gradient sets with the ratio of the products of the two sets is k and the corresponding b-values are equal, the SNR levels of the two reconstructed images will have the ratio k. In fact, the signal levels of the two images will be the same since the same velocity distribution is measured. On the other hand, the noise levels will have the ratio k. The reason is that the same signal is measured in one of the cases by accumulating k times more phase which acts as a temporal averaging mechanism. This second effect of the flow encoding parameters on the reconstructed MHD flow velocity images is the same as the effect of T_C on the reconstructed B_z images [16].

To investigate the derivation made in Section 2.3.2.1 in detail, 2D plots of the function F defined in (2.24) are obtained. Note that F is the multiplicative part of $SNR_{\boldsymbol{v},MHD}$ that is purely dependent on the flow encoding parameters. In Figure 4.20, F is given as the function of each flow encoding parameter while keeping the other two flow encoding parameters constant. In each row, a different flow encoding parameter is swept. The results in the first column are showing the results as the function of the corresponding flow encoding parameter that is swept while the results in the second column show the same plots as the function of corresponding b-values. Note that due to the constraint $\Delta > \delta$, the minimum value of Δ in Figure 4.20(c) is 10 ms, and consequently the plots in Figure 4.20(d) start from arbitrary points.

The first observation from Figure 4.20 is that in each plot in the right column, the red plots are e^{bD} times larger than the blue plots as expected. Moreover, both red and blue plots have the peak around b = 224 ($\approx \frac{1}{2D}$) s/mm^2 in Figures 4.20(b,f) whereas they have the peak around b = 448 s/mm^2 ($\approx \frac{1}{D}$) in Figure 4.20(d) as expected from (2.31).

Furthermore, experimental data are also acquired with the same flow encoding parameters to validate the analytical results using the homogeneous cylindrical phantom, and the image acquisition parameters given in Table 3.2 except T_E is modified as 85 ms. 30 different MHD flow velocity distributions are obtained with 5 different

values of each flow encoding parameter for 2 flow encoding gradient sets. All the data are acquired in the x-direction with the vertical current injection pattern. Note that for vertical current injection pattern, x-component of the MHD flow velocity distribution is dominant and the noise levels of the distributions in each direction are the same as shown in Figures 4.14 and 4.19. Hence, the experimental validation in a single direction is sufficient. Moreover, vertical current injection pattern is preferred due to higher MHD flow velocity formation as presented in Section 4.3.

The noise levels of the obtained MHD flow velocity distributions are estimated as explained in Section 2.3.3, and the reciprocals of the noise levels are also presented in Figure 4.20 as data points. Lastly, the y-axis that shows the numerical values of the function F is scaled with the experimentally estimated values to allow the comparison of analytical and experimental results. As seen, the experimental results validate the analytical estimations related to the dependence of the SNR levels of the MHD flow velocity images on different flow encoding parameters.

In Figures 4.21, 4.22, and 4.23 the obtained MHD flow velocity distributions are shown for changing δ, Δ, and G_f, respectively. These distributions also validate the claim about that the signal levels of the MHD flow velocity images do not change with flow encoding parameters, only the noise levels in the distributions change.

All in all, the flow encoding parameters provide quite smooth SNR functions for the MHD flow imaging and provide optimal values that can be analytically estimated. Hence, the utilization of the parameter selection procedure formed in Section 2.3.2.1 has the potential to increase the practicality of the MHD flow imaging procedure.

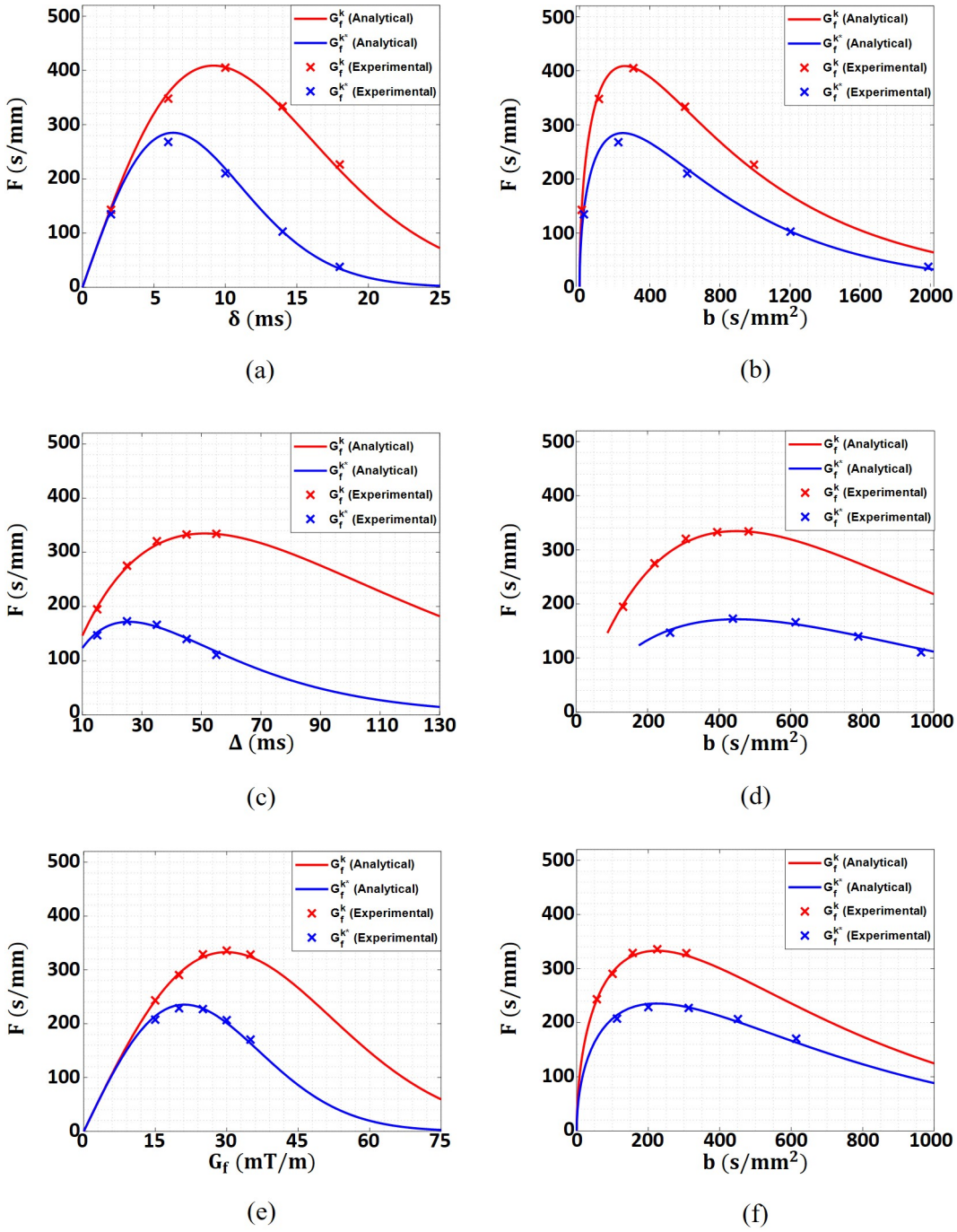

Figure 4.20: Analytical plots of (2.22) demonstrating F as a function of (a) δ, (b) b-value (sweeping δ) with Δ = 35 ms, G_f = 35 mT/m; as a function of (c) Δ, (d) b-value (sweeping Δ) with δ = 10 ms, G_f = 35 mT/m; as a function of (c) G_f, (d) b-value (sweeping G_f) with δ = 10 ms, Δ = 35 ms. The y-axis is scaled using the experimental measurements. Solid lines show analytical estimations and data points show experimental measurements.

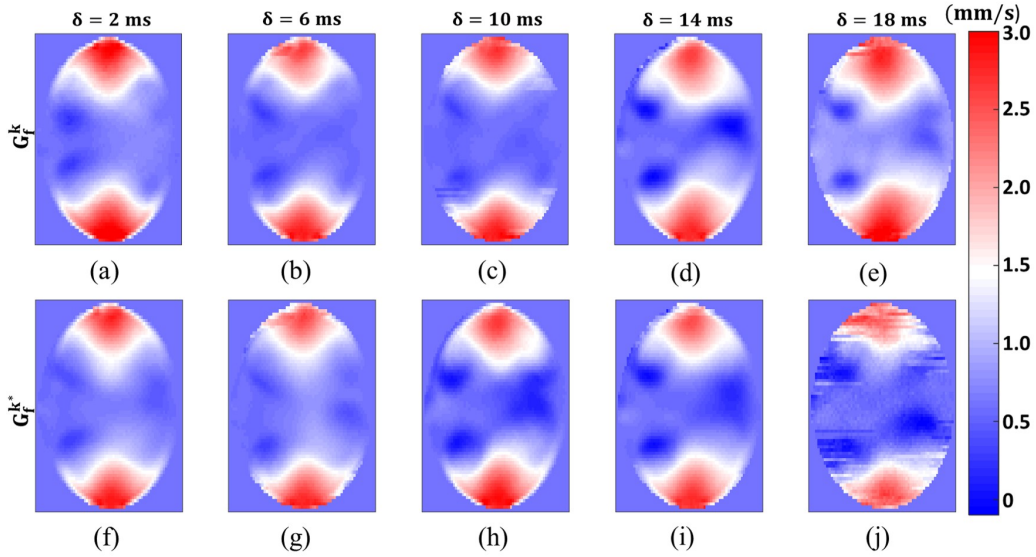

Figure 4.21: Experimentally acquired MHD flow velocity distributions in the **x**-direction. Obtained with the flow encoding gradient set $\boldsymbol{G}_f^k$ with δ = (a) 2 ms, (b) 6 ms, (c) 10 ms, (d) 14 ms, (e) 18 ms; and obtained with the flow encoding gradient set $\boldsymbol{G}_f^{k*}$ with δ = (f) 2 ms, (g) 6 ms, (h) 10 ms, (i) 14 ms, (j) 18 ms.

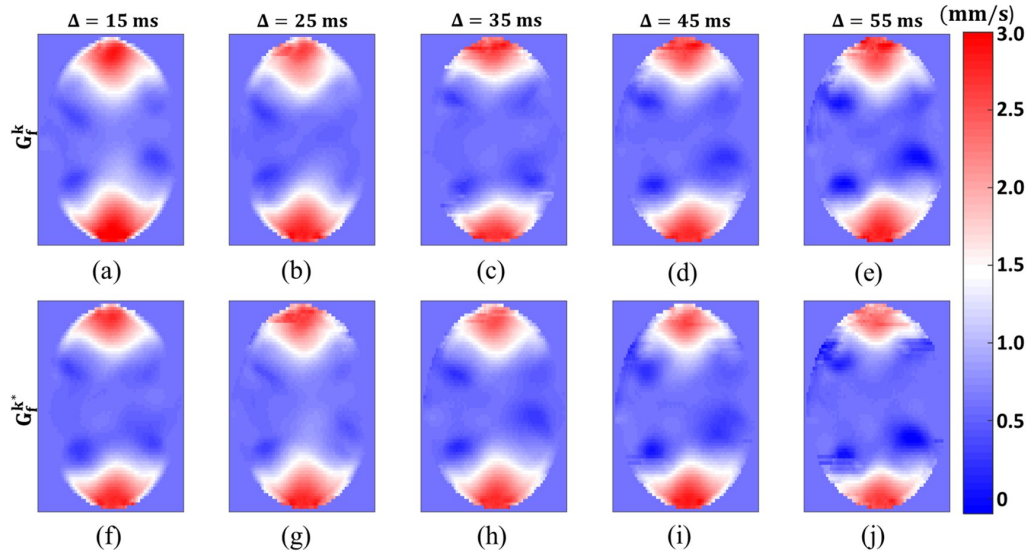

Figure 4.22: Experimentally acquired MHD flow velocity distributions in the **x**-direction. Obtained with the flow encoding gradient set $\boldsymbol{G}_f^k$ with δ = (a) 2 ms, (b) 6 ms, (c) 10 ms, (d) 14 ms, (e) 18 ms; and obtained with the flow encoding gradient set $\boldsymbol{G}_f^{k*}$ with δ = (f) 2 ms, (g) 6 ms, (h) 10 ms, (i) 14 ms, (j) 18 ms.

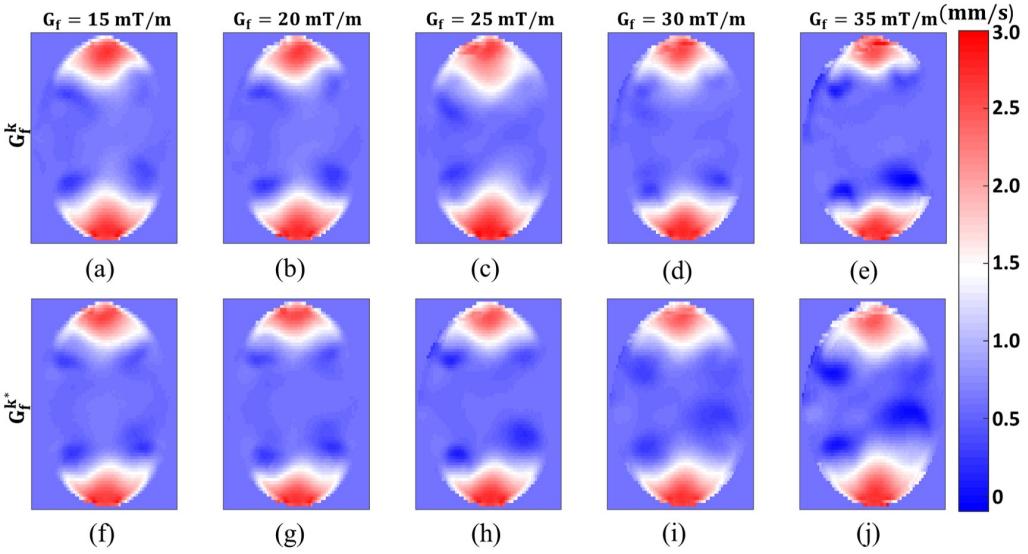

Figure 4.23: Experimentally acquired MHD flow velocity distributions in the **x**-direction. Obtained with the flow encoding gradient set $\boldsymbol{G}_f^k$ with G_f = (a) 15 mT/m, (b) 20 mT/m, (c) 25 mT/m, (d) 30 mT/m, (e) 35 mT/m; and obtained with the flow encoding gradient set $\boldsymbol{G}_f^{k^*}$ with G_f = (f) 15 mT/m, (g) 20 mT/m, (h) 25 mT/m, (i) 30 mT/m, (j) 35 mT/m.

4.4.3 The Relation between T_R and the SNR of the MHD Flow Velocity Images

As can be seen from (2.19), T_R affects the measured MR signal magnitude by T_1 weighting as expected. Consequently, the noise level of the MHD flow velocity images is also dependent on T_R with the T_1 weighting. However, with the utilization of either of the current injection schemes presented in Section 3.5, the MHD flow velocity distribution also becomes dependent on T_R since T_R is also the period of the current injection. In other words, the current pulses are injected into the medium with higher frequency when T_R is lower. Hence, it can be concluded that the MHD flow velocity distribution is not only determined by the current injection parameters I and T_C, but also by T_R as well.

Nevertheless, this situation is the result of the choice of injecting current between the 90° RF pulse and the readout. The reason for this choice in this thesis study is to develop image acquisition and reconstruction techniques for multi-contrast imaging

of the MRCDI, DTI, and MHD flow velocity imaging. In order to obtain the B_z distribution during the MRCDI experiments from the accumulated MR phase, the current must be injected in this interval. On the other hand, such a constraint does not exist for the MHD flow velocity imaging because the purpose of the current injection is to create MHD flow by forming a Lorentz force density distribution inside the medium. During the MHD flow imaging, the current can be injected before the pulse sequence or even after each readout until the next 90° RF pulse because the MHD flow will be formed inside the medium with all of these current injection strategies.

Moreover, with the utilization of different pulse sequences, the current injection schemes in Section 3.5 may not be applicable. For instance, if an EPI-based pulse sequence is utilized, injecting current only between the 90° RF pulse and the readout will not be sufficient to create a measurable MHD flow since the pulse sequence will end in only one (or a couple based on the number of shots employed in the EPI pulse sequence) T_R interval. In such a case, a current pulse should be applied before the image acquisition to form the MHD flow, and then with an EPI-based pulse sequence with flow encoding, the created MHD flow can be measured.

Still, to show the dependency of the signal and noise levels of the MHD flow velocity distributions on T_R, MHD flow velocity distributions are obtained with different T_R values using the homogeneous cylindrical phantom and the image acquisition parameters in Table 3.2 for 2 different flow encoding gradient sets and only for vertical current injection pattern. The obtained MHD flow velocity distributions in x- and y-directions are shown in Figures 4.24 and 4.25, respectively. Finally, the empirically estimated MHD flow velocity signal RMS, noise level, and corresponding SNR values as explained in Section 2.3.3 are demonstrated in Figure 4.26 as a function of T_R.

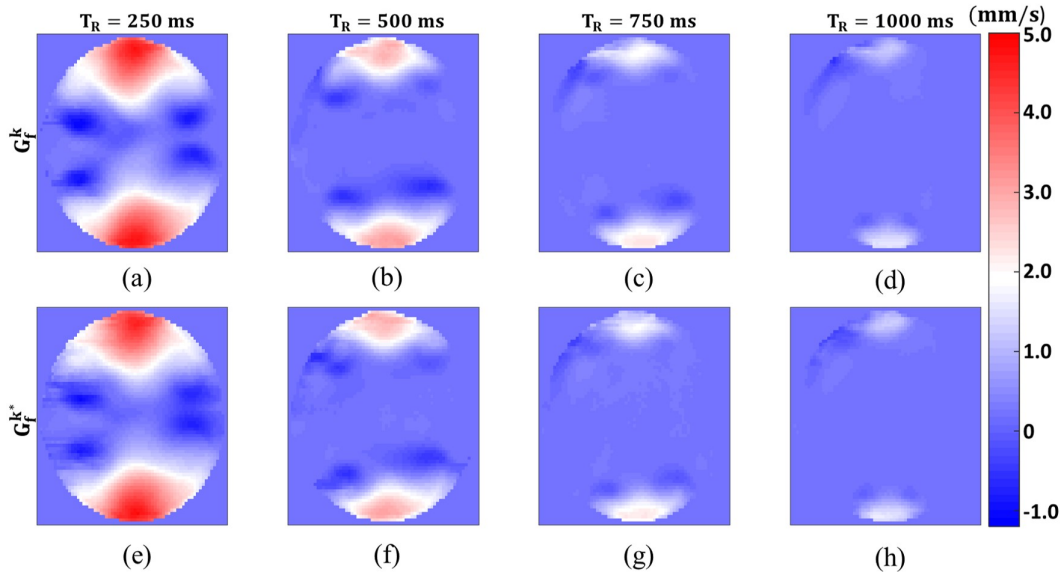

Figure 4.24: Experimentally acquired MHD flow velocity distributions in the **x**-direction. Obtained with the flow encoding gradient set $\boldsymbol{G}_f^k$ with T_R = (a) 250 ms, (b) 500 ms, (c) 750 ms, (d) 1000 ms; and obtained with the flow encoding gradient set $\boldsymbol{G}_f^{k*}$ with T_R = (e) 250 ms, (f) 500 ms, (g) 750 ms, (h) 1000 ms.

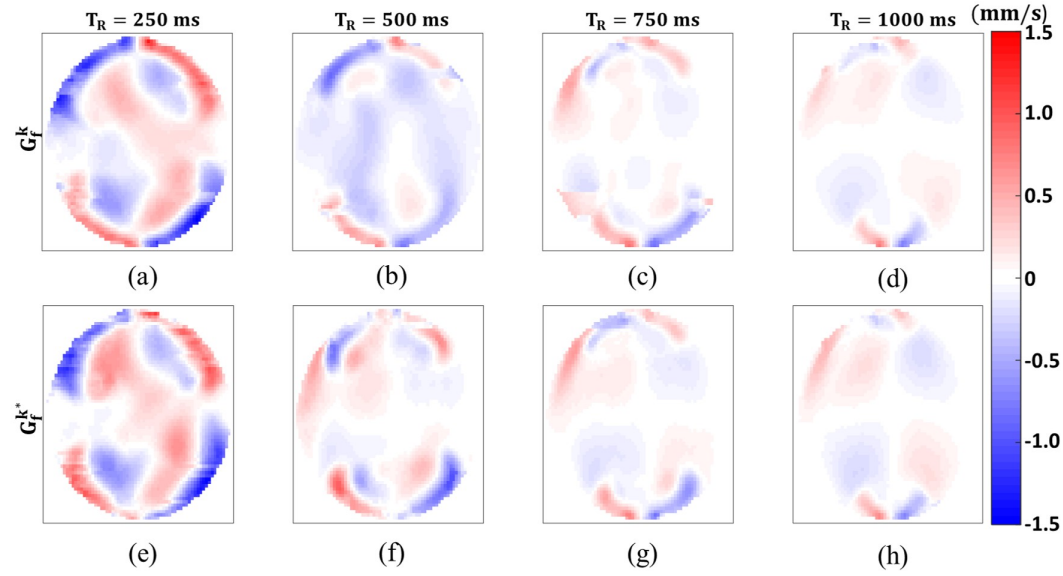

Figure 4.25: Experimentally acquired MHD flow velocity distributions in the **y**-direction. Obtained with the flow encoding gradient set $\boldsymbol{G}_f^k$ with T_R = (a) 250 ms, (b) 500 ms, (c) 750 ms, (d) 1000 ms; and obtained with the flow encoding gradient set $\boldsymbol{G}_f^{k*}$ with T_R = (e) 250 ms, (f) 500 ms, (g) 750 ms, (h) 1000 ms.

Figures 4.24 and 4.25 show that the MHD flow velocity values in both directions increase with decreasing T_R due to the increase in the current injection frequency as explained. Figures 4.26(a-b) also validates this observation. The noise levels, on the other hand, change in accordance with the T_1 recovery in the magnitude signal as can be seen from 4.26(c-d). This validates not only the claim about the relation between the noise levels of the MR phase images and the signal levels of the MR magnitude images but also the claim that with changing T_R the noise level of the MHD flow velocity images only changes due to the T_1 effect. Besides, the noise levels in the two directions are the same as explained and shown in Section 4.4.1.1.

However, that unlike I and T_C, the dependency of the MHD flow velocity distribution on T_R is not generalizable, hence, the empirically estimated SNR levels of the obtained MHD flow velocity images are not fitted into a function of T_R. As discussed, with a different choice of the MR pulse sequence or current injection scheme, this dependency may change. Moreover, because of the same reason, the $S_{\boldsymbol{v},MHD}$ term in (2.19) is defined as a function of I and T_C only.

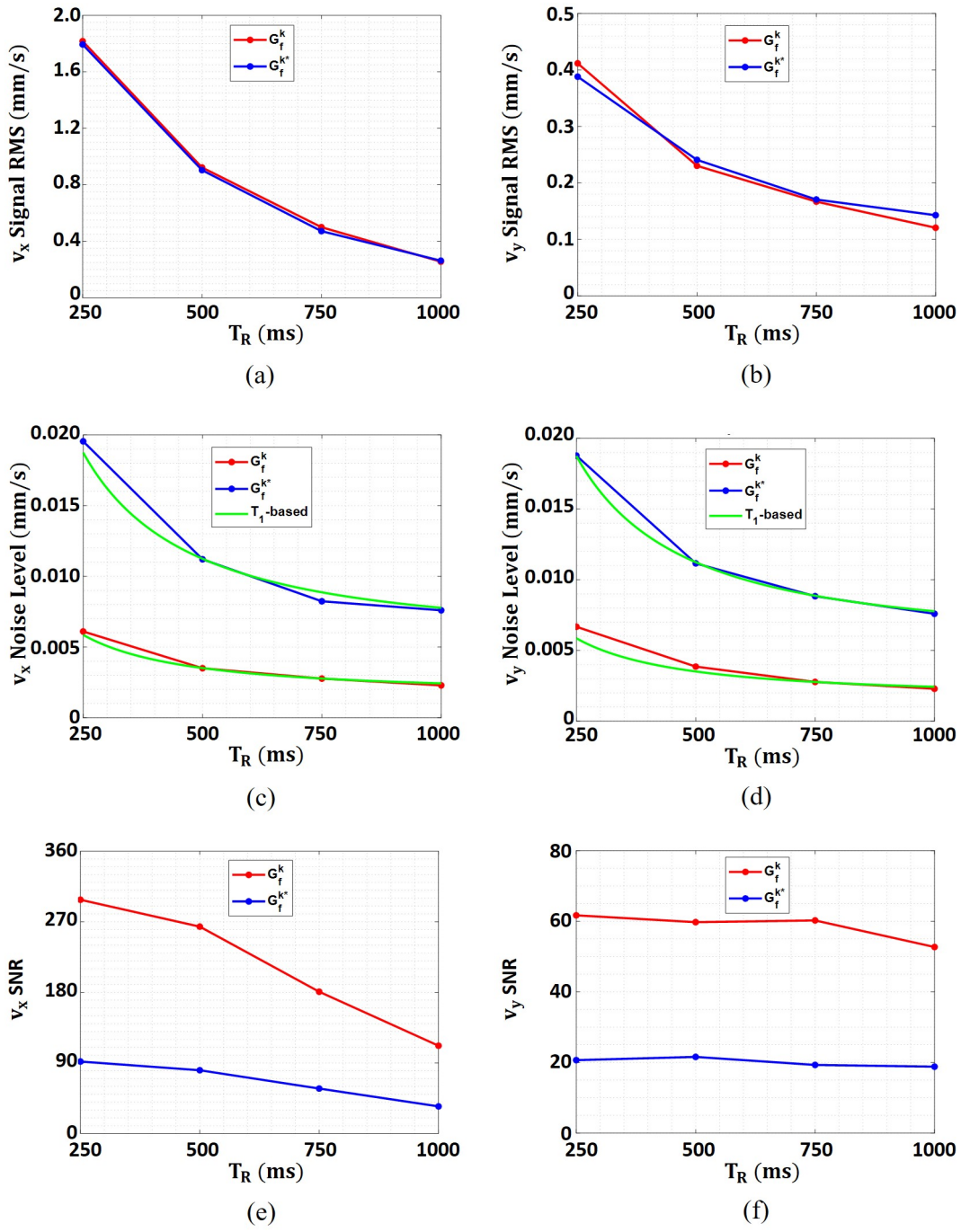

Figure 4.26: The RMS values of the experimentally acquired MHD flow velocity distributions in (a) **x**-direction, (b) **y**-direction; noise level in (c) **x**-direction, (d) **y**-direction; SNR in (e) **x**-direction, (f) **y**-direction. The green solid lines in the noise level plots show the analytically estimated (and scaled with the experimental measurements) noise levels due to the T_1 recovery.

4.4.4 Classification of the MR Image Acquisition and Current Injection Parameters based on their Effect on the SNR of the MHD Flow Velocity Images

In (2.19), it is seen that the effects of most of the current injection and MR image acquisition parameters on the SNR of the MHD flow velocity images are analytically described. However, other MR image acquisition parameters also affect the SNR of the MHD flow velocity images with different mechanisms.

First of all, FOV, matrix size, and slice thickness determine the voxel size. With increasing voxel size, the number of the proton spins that contribute to the measured MR signal from a signal voxel also increases, consequently, the noise level of the MHD flow velocity images decreases. Hence, increasing FOV and the slice thickness increases the SNR of the MHD flow velocity images whereas increasing matrix size decreases it.

Secondly, the bandwidth (BW) of the readout gradient is well known to determine the noise level of the measured MR signal. With increasing BW, the noise level of the measured signal increases since the noise in the higher frequencies is sampled as well. Furthermore, the magnitude of the static magnetic field of the MR scanner affects both the signal amplitude and the noise level of the measured MR signal. Increasing B_0 excites more proton spins and as a result, the measured signal amplitude increases. On the other hand, the existence of a relation between the noise level of the measured signal amplitude and B_0 is shown as well [73]. Finally, the increasing number of excitations (N_{EX}) increases the SNR of the acquired images due to averaging. The combined effect of the BW, B_0, and N_{EX} on the SNR of the measured MR signal can be expressed as [73, 74]:

$$SNR_M \sim \sqrt{\frac{B_0^3 N_{EX}}{BW}} \tag{4.5}$$

In addition, B_0 also affects the MHD flow velocity distribution since the Lorentz force density distribution is created by the externally injected current density distribution and B_0 as given in (2.8). However, it is difficult to estimate the exact relation between B_0 and the MHD flow velocity distribution because of the nature of the Navier-Stokes equations in (2.6) as discussed before.

In Table 4.7, all the current injection and MR image acquisition parameters whose effects on the SNR of the MHD flow velocity images are discussed are given classified based on their effect on the signal level, the noise level, or both.

Table 4.7: The current injection and MR image acquisition parameters classified based on their effect on the signal and the noise levels of the MHD flow velocity images.

Signal	**Noise Level**	**Signal + Noise Level**
I, T_C	δ, Δ, G_f, T_E, FOV, Matrix Size, Slice Thickness, BW, N_{EX}	T_R, B_0

Note that T_R is classified as a parameter that affects both the signal and noise levels of the MHD flow velocity images due to the current injection schemes employed in this thesis study as discussed in Section 4.4.3. With a different choice of current injection scheme, it may be classified as a parameter that only affects the noise level.

4.5 Evaluation of the Effect of the Diffusion and MHD on the MR Magnitude Images

In Section 2.4, it is claimed that MHD does not affect the MR magnitude images since it can be considered as a coherent (zero-variance) motion. This is an important claim because the simultaneous image reconstruction in multi-contrast imaging theory is based on the assumption that the magnitude images carry information related only to diffusion. The information is encoded into the magnitude images as space-dependent decays in the measured signals. Hence, in order to evaluate any possible effect of the MHD on the MR magnitude images, several data sets are collected with /without current injection and flow encoding using the homogeneous cubic phantom shown in Figure 3.2 and the image acquisition parameters given in Table 3.1. The average values of these magnitude images are demonstrated in Figure 4.27.

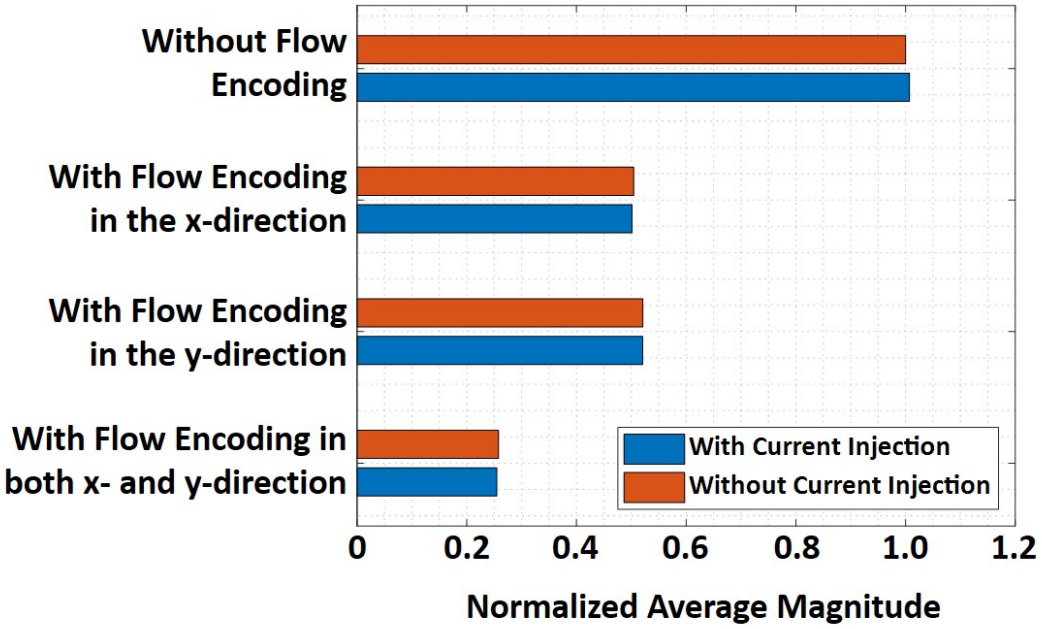

Figure 4.27: The normalized average values of the magnitude images obtained with /without current injection and flow encoding. The average magnitude values are normalized with the average value of the magnitude image obtained without current injection and flow encoding.

In Figure 4.27, it is seen that neither the induced magnetic fields by the externally injected currents nor the MHD flow formed due to these currents affect the magnitude images. The only factor that affects the average magnitude values is the application of the flow encoding gradients and resulting diffusion weighting in the magnitude signal. This can be proven considering the b-value that the flow encoding parameters in Table 3.1 corresponds (b $\approx$300 s/mm$_2$) and the diffusion coefficient of the water in the room temperature (D = 2.23$\times$10^{-3} mm^2/s). Hence, 51% (e^{-bD}) and 26% (e^{-2bD}) decay of the magnitude signal is theoretically expected, and in Figure 4.27, the amount of decays observed for the magnitude images obtained with a single flow encoding direction and double flow encoding directions correspond these expected values, respectively. Hence, it can be concluded that MHD does not affect the magnitude images and the magnitude images obtained during simultaneous multi-contrast image acquisition can be utilized to reconstruct the diffusion tensor images.

4.6 Experimental Results of the Simultaneous Multi-Contrast Imaging Data Acquisition

In order to validate the methods developed in Section 2.4, experimental data is acquired with the inhomogeneous cubic phantom shown in Figure 3.4 and the image acquisition parameters given in Table 3.3. During the multi-contrast imaging data acquisition procedure, a single current pulse scheme described in Section 3.5 is employed in order to be able to measure the B_z and MHD flow velocity distributions simultaneously. The reconstructed images of different contrasts via simultaneous multi-contrast imaging are presented in the following sections.

The results presented in this section are presented in [75].

4.6.1 Reconstructed Current Density Images

The B_z images obtained using (2.48) from the phase images of the data acquired with current injection but without flow encoding gradient application are presented in Figures 4.28(a,d) for the vertical and horizontal current injection patterns, respectively. Moreover, the projected current density ($\boldsymbol{J}_P$) distributions obtained with (2.49) are also shown in Figure 4.28.

In Figures 4.28(a,d), it is seen that the SNR levels in the regions corresponding to bovine muscle pieces are lower. The reason is that lower MR signal is received from those regions because of lower water densities. Hence, this situation reflects itself on the phase images as higher noise levels in those regions. Due to the derivative operation in (2.49), the SNR levels decrease even further in the $\boldsymbol{J}_P$ images.

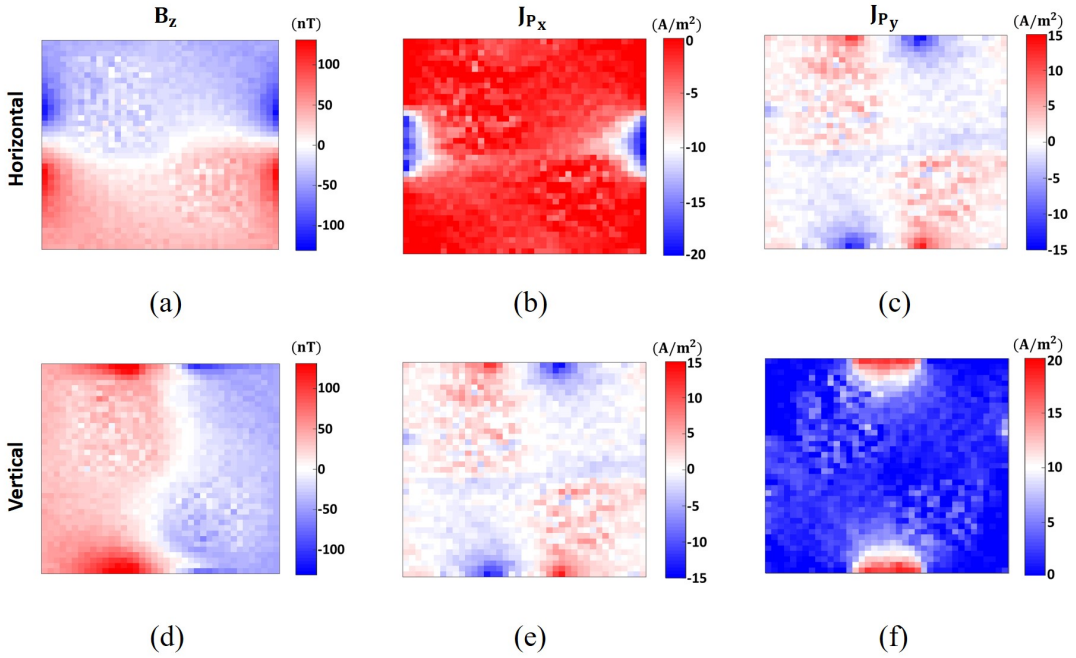

Figure 4.28: (a) Experimentally acquired B_z distribution, (b) reconstructed J_{P_x} and (c) J_{P_y} distributions with the horizontal current injection. (d) Experimentally measured B_z distribution, (e) reconstructed J_{P_x} and (f) J_{P_y} distributions with the vertical current injection.

4.6.2 Reconstructed Diffusion Tensor Images

As explained in Section 2.4.2, the diffusion tensor of an imaging slice can be reconstructed using at least 7 different magnitude images (6 with diffusion encoding, and 1 without diffusion encoding). Hence, the magnitudes of 6 complex images acquired with positive current injection and diffusion encoding gradient application and 1 complex image acquired with positive current injection but without diffusion encoding gradient application are employed for the diffusion tensor image reconstruction using (2.57). Naturally, the magnitudes of the 7 complex images acquired with negative current injection (again 6 with diffusion encoding gradient application and 1 without) can also be utilized to solve for the same diffusion tensor distribution. Hence, the diffusion tensor of the medium can be solved twice from the magnitude images acquired during the simultaneous multi-contrast imaging procedure, and these two tensor distributions can be averaged to increase the image SNR by a factor of $\sqrt{2}$. The diffusion

tensor distributions reconstructed with the explained strategy are demonstrated in the second and third rows of the Figure 4.29 for vertical and horizontal current injection patterns, respectively. Besides, the diffusion tensor of the same imaging slice is also reconstructed from the magnitude images of the 7 complex images acquired without current injection are presented in the first row of the Figure 4.29.

To begin with, in Figure 4.29, it is seen that the diffusion tensor distribution obtained

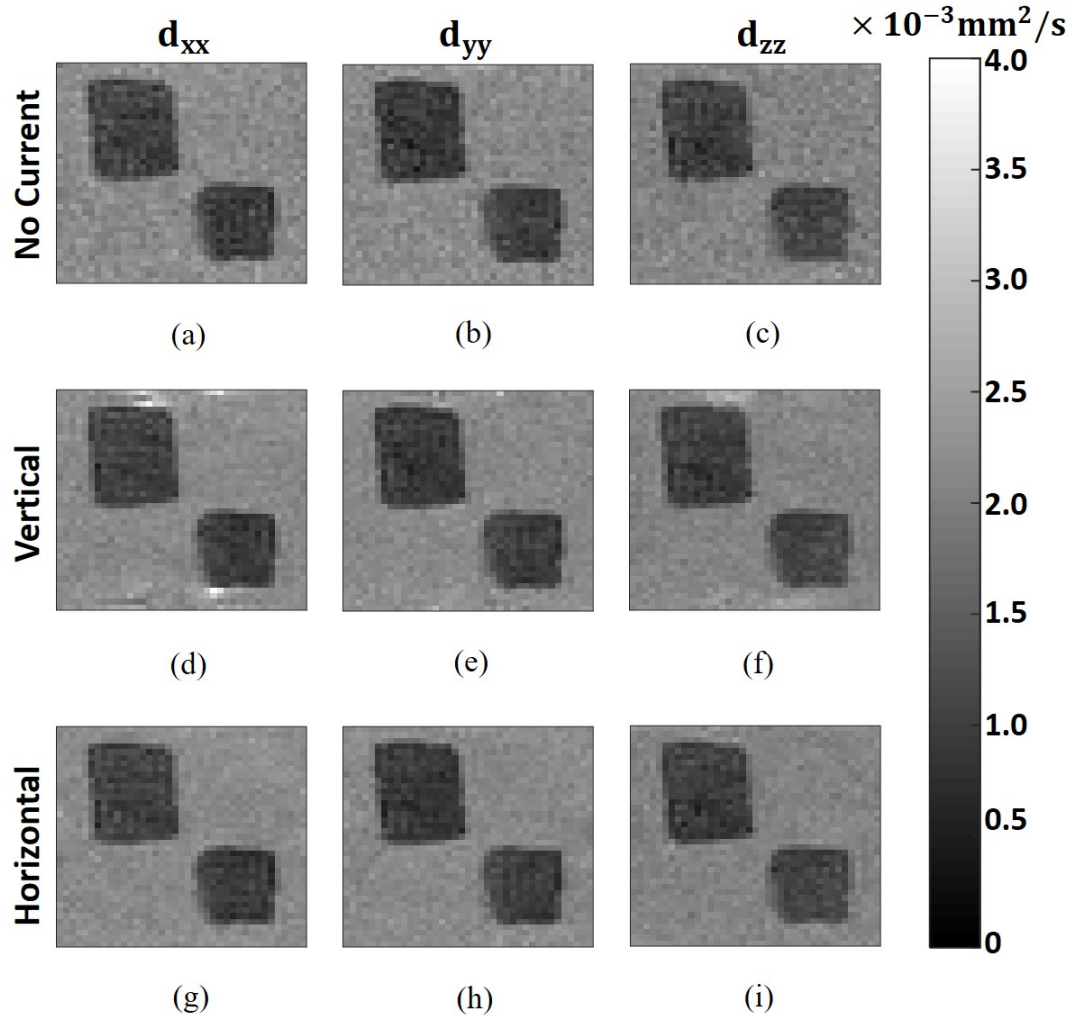

Figure 4.29: Diffusion tensor images obtained from simultaneous DTI and MHD imaging. Diffusion tensor distributions obtained without current injection: (a) d_{xx}, (b) d_{yy}, and (c) d_{zz}; with vertical current injection: (d) d_{xx}, (e) d_{yy}, and (f) d_{zz}; with horizontal current injection: (g) d_{xx}, (h) d_{yy}, and (i) d_{zz}.

using the data sets with and without current injection are almost identical except for two differences. Firstly, there is a visible SNR difference in favor of the distribution obtained with the current injection because of the $\sqrt{2}$ SNR advantage due to averaging as explained. Secondly, some small artifacts are seen just nearside the bovine muscle pieces in the diffusion tensor distributions obtained with current injection, especially in the images with vertical current injection patterns. These artifacts are caused by the MHD flow because the coherency of the motion is disturbed due to the obstacles (muscle pieces) in the flow path. Since in these regions, the MHD flow velocity is very high as well, incoherent motion due to the MHD effect starts to affect the magnitude signal. However, even with such high current injection levels (10 mA) and very sharp obstacles, the artifacts are contained only in a couple of pixels just nearside the current injection electrodes.

In addition, it can be seen that the average isotropic diffusion coefficient seen in the background is very close to the diffusion coefficient of the water in the room temperature ($D = 2.23 \times 10^{-3}$ mm^2/s) which shows that the diffusion tensor is solved correctly using the data collected using the SE-based pulse sequence presented in Figure 3.6. Moreover, anisotropy is observed inside the bovine muscle pieces since they contain fiber structures that cause a dominant diffusion in the direction parallel to the fibers. For instance, the muscle pieces in the upper left and lower right corners have larger diffusion values in the x- and z-directions, respectively.

4.6.3 Reconstructed MHD Flow Velocity Images

The MHD flow velocity images are obtained using (2.60) from the phase images of the data acquired with current injection and flow encoding gradient set $\boldsymbol{G}_f^k$. Moreover, they are obtained using (2.64) from the phase images of the data acquired with current injection and flow encoding gradient set $\boldsymbol{G}_f^{k^*}$, as well. The results are presented in Figures 4.30 and 4.31 for the vertical and horizontal current injection patterns, respectively. The results obtained using the flow encoding gradient set $\boldsymbol{G}_f^k$ cannot be included in the multi-contrast imaging results since $\boldsymbol{G}_f^k$ is not a valid gradient set for the DTI image reconstruction. However, they are presented here to compare and justify the results obtained using the flow encoding gradient set $\boldsymbol{G}_f^{k^*}$. In addition, the

RMSE values computed as (4.2) between the images obtained with the flow encoding gradient sets $\boldsymbol{G}_f^k$ and $\boldsymbol{G}_f^{k^*}$ are given in Table 4.8.

The results presented in Figures 4.30 and 4.31 and Table 4.8 justify that the MHD flow velocity distributions obtained using the flow encoding gradient sets $\boldsymbol{G}_f^k$ and $\boldsymbol{G}_f^{k^*}$ show significant qualitative and quantitative similarity. Hence, the utilization of the flow encoding gradient set $\boldsymbol{G}_f^{k^*}$ not only makes the multi-contrast imaging of the diffusion tensor and MHD flow velocity distributions possible but also does not create any discrepancy or artifacts in the reconstructed images. One difference observed between the MHD flow velocity distributions obtained using the flow encoding gradient sets $\boldsymbol{G}_f^k$ and $\boldsymbol{G}_f^{k^*}$ is in the SNR levels. There is an SNR level difference with the ratio of $\frac{e^{-bD}}{\sqrt{2}} \approx 2.17$ between them in favor of the flow encoding gradient set $\boldsymbol{G}_f^k$. $\sqrt{2}$ term is the result of the averaging of the MHD flow velocity distributions obtained with the difference and summation operations from the phase images of the data acquired with current injection and flow encoding gradient set $\boldsymbol{G}_f^{k^*}$ as explained in Section 2.4.3.

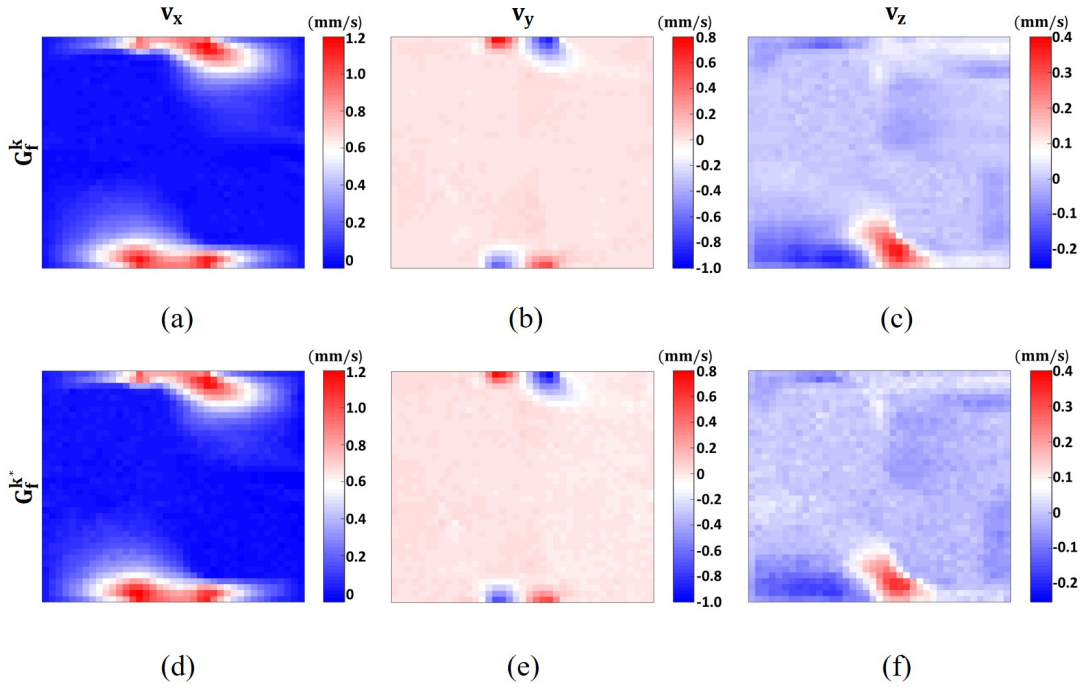

Figure 4.30: Experimentally acquired MHD flow velocity distributions inside the inhomogeneous cubic phantom obtained with vertical current injection and the flow encoding gradient set $\boldsymbol{G}_f^k$ (a) v_x, (b) v_y, and (c) v_z; with the flow encoding gradient set $\boldsymbol{G}_f^{k^*}$ (d) v_x, (e) v_y, and (f) v_z.

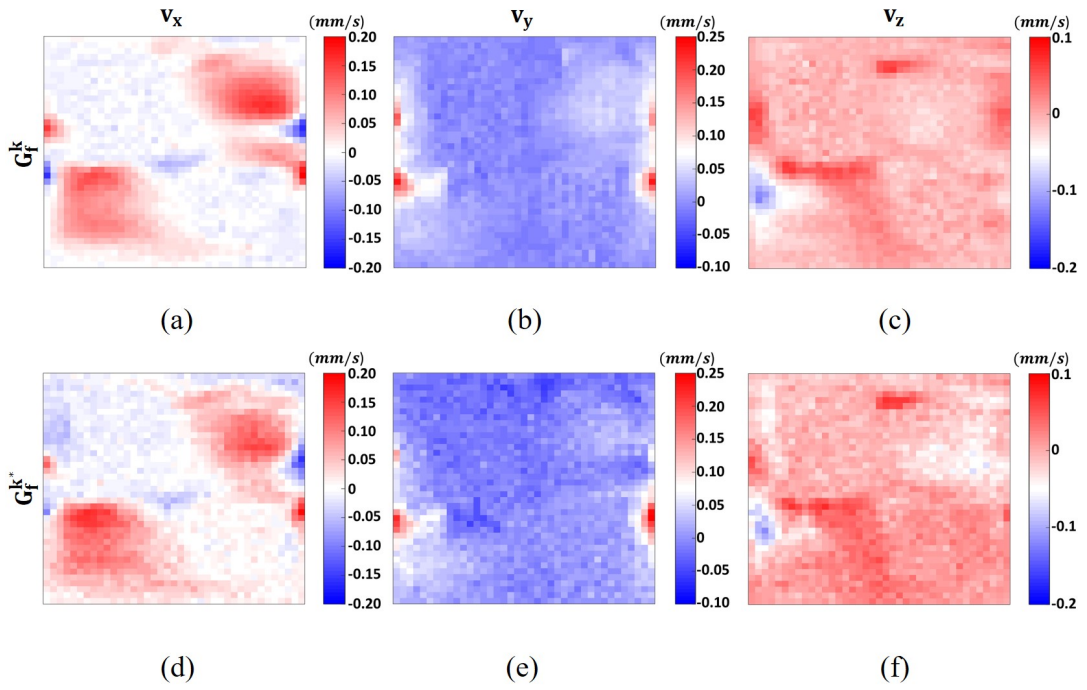

Figure 4.31: Experimentally acquired MHD flow velocity distributions inside the inhomogeneous cubic phantom obtained with horizontal current injection and the flow encoding gradient set $\boldsymbol{G}_f^k$ (a) v_x, (b) v_y, and (c) v_z; with the flow encoding gradient set $\boldsymbol{G}_f^{k*}$ (d) v_x, (e) v_y, and (f) v_z.

Table 4.8: RMSE values between the velocity distributions obtained with the flow encoding gradient sets $\boldsymbol{G}_f^k$ and $\boldsymbol{G}_f^{k*}$ shown in Figures 4.30 and 4.31.

RMSE (mm/s)	v_x	v_y	v_z
Vertical	0.021	0.020	0.018
Horizontal	0.021	0.021	0.020

Another important observation is that the maximum values of the velocity distributions in Figure 4.30 are almost four times larger than those in Figure 4.31, although the injected current pulses for two cases have the same magnitude and duration. One factor that causing this difference is the positioning of the two bovine muscle pieces. Hence, the flow dynamics in two different current injection cases get affected differently. In Figure 4.29, it is seen that there is a gap between the muscle pieces in the

vertical current injection pattern. This gap ensures a direct path between the current injection electrodes where the current can flow directly without forming significant components in the z-direction. As can be inferred from (2.8), current density components that flow in the z-direction will not produce Lorentz force and cause a decrease in the MHD flow velocity distribution. Such a scenario occurs for the horizontal current injection pattern as can be seen from Figure 4.29. Since there is no apparent gap between the muscle pieces in the horizontal current injection pattern, significant current density components travel in the z-direction that significantly decreases the MHD flow velocity distribution that is formed. Another factor that causes this difference is gravity as discussed in Section 4.3. With the vertical current injection, dominant MHD flow is created in the horizontal direction whereas, with the horizontal current injection, dominant MHD flow is created in the vertical direction. The MHD flow in the vertical direction needs to cope with gravitational force, while the MHD flow in the horizontal direction can reach higher magnitudes more easily.

In Figure 4.32, vector plots showing MHD flow velocity distributions in Figures 4.30 and 4.31, and $\boldsymbol{J}_P$ distributions in Figure 4.28 are displayed. As can be seen, MHD flow velocity and $\boldsymbol{J}_P$ distributions are almost perpendicular to each other everywhere. Due to (2.50), it is expected that Lorentz force density and $\boldsymbol{J}_P$ distributions should be orthogonal. Consequently, the MHD flow velocity distribution also becomes orthogonal to the $\boldsymbol{J}_P$ distribution, generally.

To summarize the advantages of multi-contrast imaging, the following can be considered: Using multi-contrast imaging techniques explained in Section 2.4, the data required to reconstruct three contrast distributions (current density, MHD flow velocity, and diffusion tensor) 14 complex image acquisitions are required. On the other hand, without multi-contrast imaging, 2 image acquisitions required for the MRCDI, 12 image acquisitions are required for the MHD flow velocity imaging, and 14 image acquisitions are required for the DTI with the same SNR level. Hence, the multi-contrast imaging provides a 50% decrease in the total imaging time and 100% efficiency in the utilization of the acquired data (all the magnitude and phase images are employed for image reconstruction).

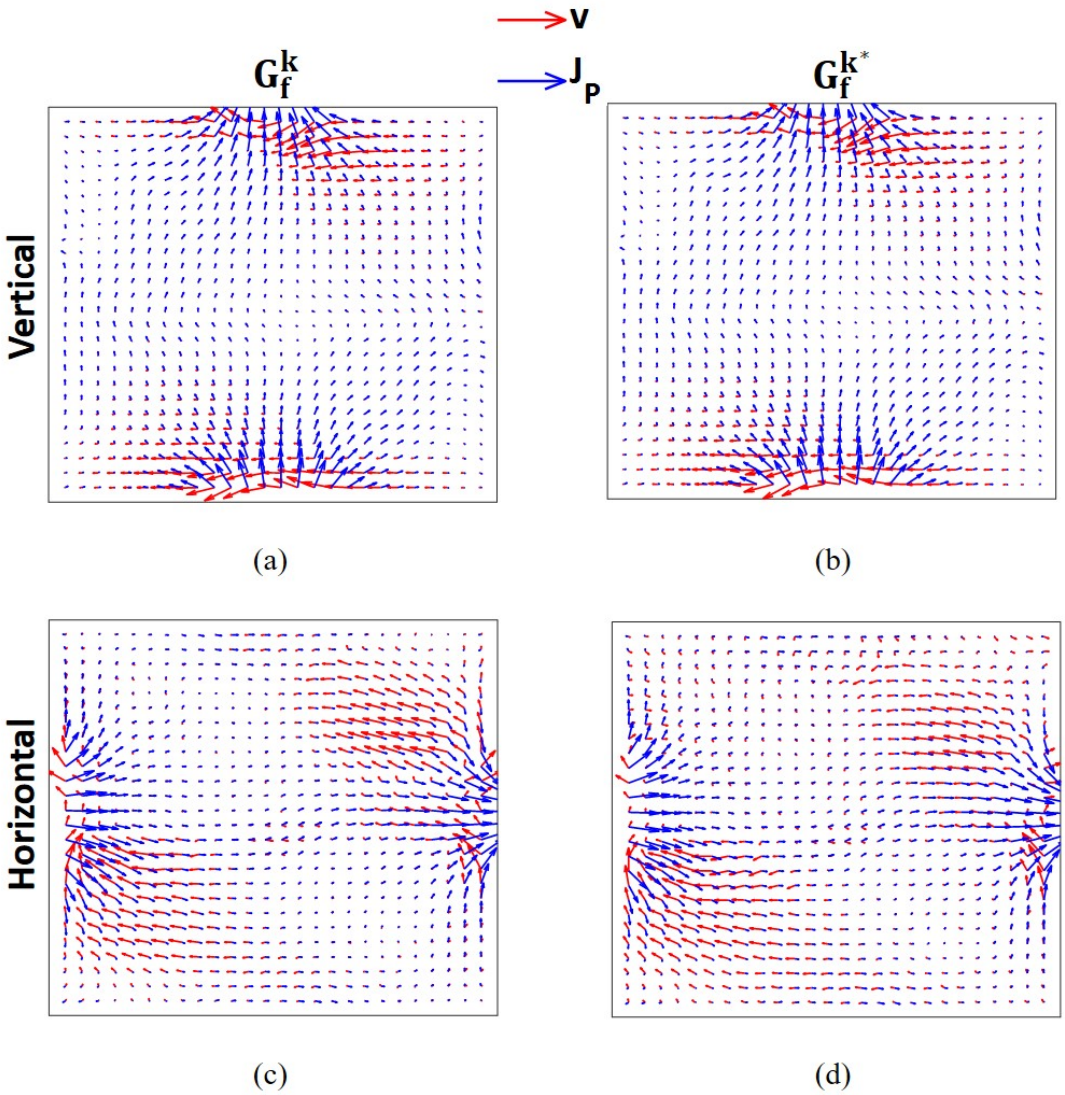

Figure 4.32: Vector plot distributions of the MHD flow velocity distributions presented in Figures 4.30 and 4.31 (red), and projected current density distributions presented in Figure 4.28 (blue). (a) For **vertical** current injection and flow encoding gradient set $\boldsymbol{G}_f^k$, (b) for **vertical** current injection and flow encoding gradient set $\boldsymbol{G}_f^{k^*}$, (c) for **horizontal** current injection and flow encoding gradient set $\boldsymbol{G}_f^k$, (d) for **horizontal** current injection and flow encoding gradient set $\boldsymbol{G}_f^{k^*}$.

4.7 Evaluation of the Minimum Current Amplitude required for the MHD Flow Velocity Imaging

As mentioned before, the amplitude of the externally injected current is limited with a few mAs in clinical applications [54]. Hence, it is important to evaluate the lower limit of the injected current amplitude (I_{min}) that will produce detectable MHD flow velocity signals. In Section 4.4.1.1, the dependency of the SNR level of the MHD flow velocity images on the injected current amplitude has been determined empirically for the homogeneous cylindrical phantom. Using the fitting parameters in Table 4.5, it is possible to obtain the current amplitude that will correspond to the SNR level that the signal level is equal to the noise level and the signal is not detectable. Moreover, utilizing (2.19) and (4.5), it is also possible to obtain the relation between other imaging parameters and I_{min}.

In Tables 4.9 and 4.10, I_{min} values are given for different B_0 and A values for the flow encoding gradient sets $\boldsymbol{G}_f^k$ and $\boldsymbol{G}_f^{k*}$, respectively. Note that B_0 is the magnitude of the static magnetic field of the MR scanner, and A is the area under the flow encoding gradient pulse defined as (2.23). These parameters are chosen since they are the most nonlinear parameters that strongly affect the SNR of the MHD flow velocity images. Note that other MR image acquisition parameters are kept constant as given in Table 3.2 and T_C is 10 ms.

As stated in (4.4), the important parameter for the MHD flow formation is not the current pulse amplitude itself but the area underneath. Hence, any value given in Tables 4.9 and 4.10 can be decreased by a scale as long as T_C = 10 ms is increased by the same scale. Besides, the SNR level of the MHD flow velocity images also increases by a factor of $\sqrt{N_{EX}}$ when a number of excitations N_{EX} is employed during image acquisition as stated in (4.5). As a result, I_{min} values for different T_C and N_{EX} values can easily be derived from the information given in Tables 4.9 and 4.10.

With the image acquisition paramaters utilized in the physical experiments using the homogeneous cylindrical phantom (B_0 = 3T, A = 490 mT/m$\times$ms, and T_C = 10 ms), I_{min} values are 1.43 mA and 1.94 mA for the flow encoding gradient sets $\boldsymbol{G}_f^k$ and $\boldsymbol{G}_f^{k*}$, respectively.

Table 4.9: Minimum current amplitude (I_{min} (mA)) required for the MHD flow velocity imaging for different B_0 and A values utilizing the flow encoding gradient set $\boldsymbol{G}_f^k$.

$\mathbf{I_{min}}$ **(mA)**	$\boldsymbol{B_0}$ **= 1.5T**	$\boldsymbol{B_0}$ **= 3T**	$\boldsymbol{B_0}$ **= 7T**	$\boldsymbol{B_0}$ **= 11.7T**	$\boldsymbol{B_0}$ **= 18.8T**
$\boldsymbol{A}$ **= 200 (mT/m×ms)**	5.91	2.00	0.53	0.24	0.11
$\boldsymbol{A}$ **= 400 (mT/m×ms)**	4.56	1.55	0.41	0.19	0.09
$\boldsymbol{A}$ **= 600 (mT/m×ms)**	3.92	1.33	0.35	0.16	0.08
$\boldsymbol{A}$ **= 800 (mT/m×ms)**	3.52	1.20	0.32	0.14	0.07
$\boldsymbol{A}$ **= 1000 (mT/m×ms)**	3.24	1.10	0.29	0.13	0.06

Table 4.10: Minimum current amplitude (I_{min} (mA)) required for the MHD flow velocity imaging for different B_0 and A values utilizing the flow encoding gradient set $\boldsymbol{G}_f^{k*}$.

$\mathbf{I_{min}}$ **(mA)**	$\boldsymbol{B_0}$ **= 1.5T**	$\boldsymbol{B_0}$ **= 3T**	$\boldsymbol{B_0}$ **= 7T**	$\boldsymbol{B_0}$ **= 11.7T**	$\boldsymbol{B_0}$ **= 18.8T**
$\boldsymbol{A}$ **= 200 (mT/m×ms)**	9.27	2.90	0.70	0.30	0.13
$\boldsymbol{A}$ **= 400 (mT/m×ms)**	6.79	2.12	0.51	0.22	0.10
$\boldsymbol{A}$ **= 600 (mT/m×ms)**	5.65	1.77	0.43	0.18	0.08
$\boldsymbol{A}$ **= 800 (mT/m×ms)**	4.97	1.55	0.38	0.16	0.07
$\boldsymbol{A}$ **= 1000 (mT/m×ms)**	4.49	1.41	0.34	0.14	0.06

One important remark here is that the analysis in this section is conducted using the data collected via a single-channel RF body coil as stated in Section 3.4. However, it is known that the utilization of phased array coils can significantly increase the sensitivity and the SNR level of the acquired signal. Ideally, using N independent phase array coils can increase the SNR level of the acquired signal by a factor of $\sqrt{N}$. In practice, such an increase is not usually achieved but it can still be significant [76, 77]. Consequently, if phased-array coils are utilized during the data acquisition procedure of the MHD flow velocity imaging, the minimum current amplitude can be decreased further.

CHAPTER 5

CONCLUSION

Magnetohydrodynamic flow is a phenomenon that takes place inside low viscosity media under the effect of orthogonal electric and magnetic fields. The measurement of the velocity of the MHD flow using MRI techniques is a novel approach in the literature and its possible applications in the clinics are promising. Especially, combining the MHD flow velocity imaging with the imaging modalities where external current injection already utilized such as the MRCDI and MREIT is very feasible since no additional effort would be needed except a pulse sequence that contains motion-sensitizing gradients to obtain the MHD flow velocity distribution as well. Moreover, there is an important opportunity such that combining image acquisition procedures of the MHD flow velocity imaging and DTI since both imaging modalities require image acquisitions via a pulse sequence that contains motion-sensitizing gradients. The image reconstruction procedure of the DTI utilizes the acquired magnitude images while the acquired phase images can be employed to solve for the MHD flow velocity distribution inside the medium. Thus, combining the image acquisition procedures of these three different imaging modalities (MRCDI, DTI, and MHD flow imaging) that provide three unique contrast distributions is possible. These three different contrast distributions provide different information based on different physical phenomena and laws. In other words, medically important information related to three different physical phenomena can be extracted from the simultaneously acquired data.

In this thesis study, firstly, the MHD flow velocimetry is implemented utilizing an SE-based pulse sequence with motion-sensitizing gradients. The relation between the MHD flow velocity distribution, the parameters of the flow encoding gradients that are utilized for the encoding of the MHD flow into MR phase images, and the cor-

responding flow-encoded phase images is constructed for SE-based pulse sequences. Then, a FE model is designed in COMSOL Multiphysics® software and MHD flow velocity inside the medium is obtained using the time-dependent solver. An experimental phantom which is identical to the designed FE model is prepared using a 3D plexiglass container and a saline solution. The MHD flow velocity distribution formed inside the experimental phantom is extracted from the acquired phase images using the constructed relation. Although the FE-based numerical simulation and physical experiments provide similar distributions, the scales of the obtained distributions differed up to 2 times in favor of the simulation results. It is concluded that FE-based simulation is not optimal for the MHD flow velocity estimations since it is not able to model intermolecular forces such as dipole-ion interactions that are the physical mechanisms that create MHD flow in practice.

Secondly, a semi-analytical analysis of the sensitivity of the MHD flow velocity images on different current injection and MR image acquisition parameters is conducted. An equation that contains these parameters and is proportional to the SNR level of the experimentally acquired MHD flow velocity images is derived. The dependency of the created MHD flow velocity distribution on the current injection amplitude and duration is empirically determined from the experimental measurements obtained by sweeping parameters. As a result of these experiments, it is observed that the magnitude of the MHD flow velocity is increasing with the increasing area of the current injection pulse with an approximate power of 2.3 inside a homogeneous cylindrical medium. Furthermore, it is observed that the behavior of the MHD flow is altering depending on the current injection pattern because of the gravity. An identical current injection creates larger MHD flow velocity values when the vertical current injection pattern is utilized instead of the horizontal. The reason is that the vertical current injection creates MHD flow dominantly in the horizontal direction whereas the horizontal current injection causes dominant MHD flow to be formed in the vertical direction. Since the vertical flow needs to struggle with the gravitational force, it ends up with smaller flow velocities. In addition, as a result of the analysis conducted on the effect of the flow encoding parameters on the SNR level of the MHD flow velocity images, it is derived that a b-value of 224 s/mm^2 is optimal for the water at room temperature to maximize the SNR level of the obtained images. This thesis

study carries the significance of being the first study that a relation between the SNR level of the acquired MHD flow velocity images and the b-value of the acquisition is constructed. Moreover, a strategy to choose a b-value that will provide optimum SNR level for the MHD flow velocity images is proposed.

Lastly, the image acquisition and reconstruction techniques for the multi-contrast imaging of the MRCDI, DTI, and MHD flow velocity imaging using simultaneous data acquisition are proposed. It is experimentally validated that by employing a suitable flow encoding gradient set, each three contrast distributions can be reconstructed from the complex data obtained in 14 acquisitions. Half of these 14 acquisitions should be realized with positive current injection and the other half with negative current injection. Moreover, 1 of each acquisition should contain no flow encoding gradient application. Hence, from the phase images of the acquisitions with and without flow encoding gradient application B_z and MHD flow velocity distributions can be extracted, respectively. B_z distribution, then, can be utilized to solve for the current density distribution. Moreover, the diffusion tensor distribution of the medium can be reconstructed twice with the magnitude images of all 14 acquisitions. These two reconstructions can be averaged to increase the SNR by a factor of $\sqrt{2}$. It is notable to state that without multi-contrast imaging, the separate reconstruction of these three contrast distributions (including diffusion tensor distribution with the same SNR) would require 28 acquisitions. Therefore, the multi-contrast imaging provides a 50% gain from the total image acquisition duration which is very important for the clinical applications of the MRI in general. In addition, multi-contrast imaging can be considered as a 100% efficient technique since all the acquired magnitude and phase images are utilized for image reconstruction. Finally, the minimum current injection levels required to obtain detectable MHD flow velocity images are determined using the empirically determined relations. For two different flow encoding sets 1.43 mA and 1.94 mA current injection levels are computed as the minimum values for the homogeneous cylindrical experimental phantom with the MR image acquisition parameters utilized during the experiments.

As can be inferred from the Lorentz force definition in (2.8), the magnitude of the MHD flow velocity distribution depends significantly on the magnitude of the static magnetic field of the MR scanner. Assuming the B_0 dependency of the MHD flow

velocity distribution is the same as the I dependency (since the Lorentz Force density distribution is the product of these two distributions), from the results in Section 4.4.1.1, it can be claimed that the MHD flow velocity distribution increases with increasing B_0 with an approximate power of 2.45. Combining this claim with the B_0 dependency of the system SNR of the MR scanner given in (4.5), a dependency of the SNR levels of the MHD flow velocity distributions on B_0 with an approximate power of 4 is expected. This crucial observation suggests that there is a huge potential for the MHD flow velocity imaging in high field MRI studies.

Another possible application of the MHD flow velocity imaging is temporal imaging via fast imaging pulse sequences such as EPI. For instance, using single-shot EPI, it is possible to obtain the time evolution of the MHD flow inside the medium due to externally injected currents. The current injection schemes presented in Section 3.5 can be utilized with single-shot EPI as well. However, this time the whole k-space can be filled in each T_R to obtain the MHD flow velocity distribution after each current injection. Hence, the formation of the MHD flow can be measured in the time domain as well.

Furthermore, as mentioned before, in [7], it is proposed that MHD-driven CSF flow may be a novel fMRI contrast mechanism which is the flow of CSF in response to the neural activity instead of externally injected currents. It is argued that if MHD-driven CSF flow-based fMRI can successfully be realized, it can be utilized in the presurgical evaluation process of epilepsy patients.

All in all, MHD flow velocity imaging is an emerging MRI modality and promising research questions that can be utilized in clinical applications are available. In this thesis study, an analysis of the SNR levels of the MHD flow velocity images on current injection and flow encoding parameters is conducted and a flow encoding gradient set is proposed for the simultaneous data acquisition for DTI and MHD flow velocimetry for the first time.

5.1 Publications During M.Sc. Study

5.1.1 Journal Articles

1. M. Sadighi, **M. Şişman**, B. C. Açıkgöz, H. H. Eroğlu, and B. M. Eyüboğlu, "Low-frequency conductivity tensor imaging with a single current injection using DT-MREIT," Physics in Medicine & Biology, vol. 66, no. 5, p. 055011, 2021.

5.1.2 Conference Abstracts

1. **M. Şişman**, M. Sadighi, H. H. Eroğlu, and B. M. Eyüboğlu, "Experimental evaluation of spin echo based magnetic resonance magnetohydrodynamic flow velocimetry," in ISMRM & SMRT Virtual Conference & Exhibition, p. 1256, ISMRM, 2021.

2. **M. Şişman**, M. Sadighi, and B. M. Eyüboğlu, "Simultaneous magnetic resonance magnetohydrodynamic flow velocity and diffusion tensor imaging," in ISMRM & SMRT Virtual Conference & Exhibition, p. 1257, ISMRM, 2021.

3. M. Sadighi, **M. Şişman**, and B. M. Eyüboğlu, "Multi-physics multi-contrast magnetic resonance imaging," in ISMRM & SMRT Virtual Conference & Exhibition, p. 1239, ISMRM, 2021.

4. M. Sadighi, **M. Şişman**, and B. M. Eyüboğlu, "Optimization of SNR and the total acquisition time in MRCDI," in ISMRM & SMRT Virtual Conference & Exhibition, p. 3789, ISMRM, 2021.

5. M. Sadighi, **M. Şişman**, B. C. Açıkgöz, and B. M. Eyüboğlu, "Single current diffusion tensor magnetic resonance electrical impedance tomography: A simulation study," in ISMRM & SMRT Virtual Conference & Exhibition, p. 3233, ISMRM, 2020.

6. M. Sadighi, **M. Şişman**, B. C. Açıkgöz, and B. M. Eyüboğlu, "Experimental realization of single current diffusion tensor magnetic resonance electrical

impedance tomography," in ISMRM & SMRT Virtual Conference & Exhibition, p. 0179, ISMRM, 2020. (Received the Magna Cum Laude Merit Award.)

REFERENCES

[1] S. Benders, B. F. Gomes, M. Carmo, L. A. Colnago, and B. Blümich, "In-situ mri velocimetry of the magnetohydrodynamic effect in electrochemical cells," *Journal of Magnetic Resonance*, vol. 312, p. 106692, 2020.

[2] G. Scott, M. Joy, R. Armstrong, and R. Henkelman, "Measurement of nonuniform current density by magnetic resonance," *IEEE transactions on medical imaging*, vol. 10, no. 3, pp. 362–374, 1991.

[3] T. S. Tenforde, "Magnetically induced electric fields and currents in the circulatory system," *Progress in Biophysics and Molecular Biology*, vol. 87, no. 2-3, pp. 279–288, 2005.

[4] J. W. Krug and G. Rose, "Magnetohydrodynamic distortions of the ECG in different MR scanner configurations," in *2011 Computing in Cardiology*, pp. 769–772, IEEE, 2011.

[5] D. Abi-Abdallah, V. Robin, A. Drochon, and O. Fokapu, "Alterations in human ECG due to the magnetohydrodynamic effect: a method for accurate R peak detection in the presence of high MHD artifacts," in *2007 29th Annual International Conference of the IEEE Engineering in Medicine and Biology Society*, pp. 1842–1845, IEEE, 2007.

[6] D. Stäb, J. Roessler, K. O'Brien, C. Hamilton-Craig, and M. Barth, "ECG triggering in ultra-high field cardiovascular MRI," *Tomography*, vol. 2, no. 3, p. 167, 2016.

[7] M. Balasubramanian, R. V. Mulkern, W. M. Wells, P. Sundaram, and D. B. Orbach, "Magnetic resonance imaging of ionic currents in solution: the effect of magnetohydrodynamic flow," *Magnetic resonance in medicine*, vol. 74, no. 4, pp. 1145–1155, 2015.

[8] A. S. Minhas, M. Chauhan, F. Fu, and R. Sadleir, "Evaluation of magnetohydrodynamic effects in magnetic resonance electrical impedance tomography at ultra-high magnetic fields," *Magnetic resonance in medicine*, vol. 81, no. 4, pp. 2264–2276, 2019.

[9] H. H. Eroğlu, M. Sadighi, and B. M. Eyüboğlu, "Magnetohydrodynamic flow imaging of ionic solutions using electrical current injection and MR phase measurements," *Journal of Magnetic Resonance*, vol. 303, pp. 128–137, 2019.

[10] H. H. Eroğlu, M. Sadighi, and B. M. Eyüboğlu, "Magnetohydrodynamic flow imaging using spin-echo pulse sequence," in *2019 27th Signal Processing and Communications Applications Conference (SIU)*, pp. 1–4, IEEE, 2019.

[11] B. M. Eyüboğlu, *Magnetic Resonance Current Density Imaging*. Wiley Online Library, 2006.

[12] T. Neuling, S. Wagner, C. H. Wolters, T. Zaehle, and C. S. Herrmann, "Finite-element model predicts current density distribution for clinical applications of tdcs and tacs," *Frontiers in psychiatry*, vol. 3, p. 83, 2012.

[13] A. Roy, B. Baxter, and B. He, "High-definition transcranial direct current stimulation induces both acute and persistent changes in broadband cortical synchronization: a simultaneous tDCS–EEG study," *IEEE Transactions on Biomedical Engineering*, vol. 61, no. 7, pp. 1967–1978, 2014.

[14] J. C. Mosher, R. M. Leahy, and P. S. Lewis, "EEG and MEG: forward solutions for inverse methods," *IEEE Transactions on Biomedical Engineering*, vol. 46, no. 3, pp. 245–259, 1999.

[15] M. Joy, G. Scott, and M. Henkelman, "In vivo detection of applied electric currents by magnetic resonance imaging," *Magnetic resonance imaging*, vol. 7, no. 1, pp. 89–94, 1989.

[16] G. Scott, M. Joy, R. Armstrong, and R. Henkelman, "Sensitivity of magnetic-resonance current-density imaging," *Journal of Magnetic Resonance (1969)*, vol. 97, no. 2, pp. 235–254, 1992.

[17] B. M. Eyüboğlu, R. Reddy, and J. S. Leigh, "Imaging electrical current density using nuclear magnetic resonance," *TURKISH JOURNAL OF ELECTRICAL ENGINEERING & COMPUTER SCIENCES*, vol. 6, no. 3, pp. 201–214, 2000.

[18] G. Scott, M. Joy, R. Armstrong, and R. Henkelman, "RF current density imaging in homogeneous media," *Magnetic resonance in medicine*, vol. 28, no. 2, pp. 186–201, 1992.

[19] G. C. Scott, M. L. Joy, R. L. Armstrong, and R. M. Henkelman, "Electromagnetic considerations for rf current density imaging [MRI technique]," *IEEE transactions on medical imaging*, vol. 14, no. 3, pp. 515–524, 1995.

[20] G. C. Scott, M. L. Joy, R. L. Armstrong, and R. Mark Henkelman, "Rotating frame RF current density imaging," *Magnetic resonance in medicine*, vol. 33, no. 3, pp. 355–369, 1995.

[21] U. Mikac, F. Demšar, K. Beravs, and I. Serša, "Magnetic resonance imaging of alternating electric currents," *Magnetic resonance imaging*, vol. 19, no. 6, pp. 845–856, 2001.

[22] L. T. Muftuler, M. Hamamura, O. Birgul, and O. Nalcioglu, "Resolution and contrast in magnetic resonance electrical impedance tomography (MREIT) and its application to cancer imaging," *Technology in cancer research & treatment*, vol. 3, no. 6, pp. 599–609, 2004.

[23] C. Park, B. I. Lee, and O. I. Kwon, "Analysis of recoverable current from one component of magnetic flux density in MREIT and MRCDI," *Physics in Medicine & Biology*, vol. 52, no. 11, p. 3001, 2007.

[24] C. Park, B. I. Lee, O. Kwon, and E. J. Woo, "Measurement of induced magnetic flux density using injection current nonlinear encoding (ICNE) in MREIT," *Physiological measurement*, vol. 28, no. 2, p. 117, 2006.

[25] T. I. Oh, W. C. Jeong, J. E. Kim, S. Z. Sajib, H. J. Kim, O. I. Kwon, and E. J. Woo, "Noise analysis in fast magnetic resonance electrical impedance tomography (MREIT) based on spoiled multi gradient echo (SPMGE) pulse sequence," *Physics in Medicine & Biology*, vol. 59, no. 16, p. 4723, 2014.

[26] C. Göksu, L. G. Hanson, H. R. Siebner, P. Ehses, K. Scheffler, and A. Thielscher, "Human in-vivo brain magnetic resonance current density imaging (MRCDI)," *NeuroImage*, vol. 171, pp. 26–39, 2018.

[27] H. C. Torrey, "Bloch equations with diffusion terms," *Physical review*, vol. 104, no. 3, p. 563, 1956.

[28] E. Stejskal, "Use of spin echoes in a pulsed magnetic-field gradient to study anisotropic, restricted diffusion and flow," *The Journal of Chemical Physics*, vol. 43, no. 10, pp. 3597–3603, 1965.

[29] D. Le Bihan, E. Breton, D. Lallemand, P. Grenier, E. Cabanis, and M. Laval-Jeantet, "MR imaging of intravoxel incoherent motions: application to diffusion and perfusion in neurologic disorders.," *Radiology*, vol. 161, no. 2, pp. 401–407, 1986.

[30] M. A. Bernstein, K. F. King, and X. J. Zhou, *Handbook of MRI pulse sequences*. Elsevier, 2004.

[31] S. Warach, D. Chien, W. Li, M. Ronthal, and R. Edelman, "Fast magnetic resonance diffusion-weighted imaging of acute human stroke," *Neurology*, vol. 42, no. 9, pp. 1717–1717, 1992.

[32] M. E. Moseley, Y. Cohen, J. Mintorovitch, L. Chileuitt, H. Shimizu, J. Kucharczyk, M. Wendland, and P. Weinstein, "Early detection of regional cerebral ischemia in cats: comparison of diffusion-and t2-weighted MRI and spectroscopy," *Magnetic resonance in medicine*, vol. 14, no. 2, pp. 330–346, 1990.

[33] Y. Ohba, H. Nomori, T. Mori, K. Ikeda, H. Shibata, H. Kobayashi, S. Shiraishi, and K. Katahira, "Is diffusion-weighted magnetic resonance imaging superior to positron emission tomography with fludeoxyglucose F 18 in imaging non–small cell lung cancer?," *The Journal of thoracic and cardiovascular surgery*, vol. 138, no. 2, pp. 439–445, 2009.

[34] D. Le Bihan, J.-F. Mangin, C. Poupon, C. A. Clark, S. Pappata, N. Molko, and H. Chabriat, "Diffusion tensor imaging: concepts and applications," *Journal of Magnetic Resonance Imaging: An Official Journal of the International Society for Magnetic Resonance in Medicine*, vol. 13, no. 4, pp. 534–546, 2001.

[35] K. Kantarci, R. Avula, M. Senjem, A. Samikoglu, B. Zhang, S. Weigand, S. Przybelski, H. Edmonson, P. Vemuri, D. S. Knopman, *et al.*, "Dementia with lewy bodies and alzheimer disease: neurodegenerative patterns characterized by DTI," *Neurology*, vol. 74, no. 22, pp. 1814–1821, 2010.

[36] M. Kubicki, H. Park, C.-F. Westin, P. G. Nestor, R. V. Mulkern, S. E. Maier, M. Niznikiewicz, E. E. Connor, J. J. Levitt, M. Frumin, *et al.*, "DTI and MTR abnormalities in schizophrenia: analysis of white matter integrity," *Neuroimage*, vol. 26, no. 4, pp. 1109–1118, 2005.

[37] T.-K. Truong, A. Avram, and A. W. Song, "Lorentz effect imaging of ionic currents in solution," *Journal of Magnetic Resonance*, vol. 191, no. 1, pp. 93–99, 2008.

[38] R. S. Wijesinghe and B. J. Roth, "Lorentz effect imaging of ionic currents in solution using correct values for ion mobility," *Journal of magnetic resonance*, vol. 204, no. 2, pp. 225–227, 2010.

[39] N. Pourtaheri, T.-K. Truong, and C. S. Henriquez, "Electromagnetohydrodynamic modeling of lorentz effect imaging," *Journal of Magnetic Resonance*, vol. 236, pp. 57–65, 2013.

[40] S. H. Oh, B. I. Lee, E. J. Woo, S. Y. Lee, M. H. Cho, O. Kwon, and J. K. Seo, "Conductivity and current density image reconstruction using harmonic Bz algorithm in magnetic resonance electrical impedance tomography," *Physics in Medicine & Biology*, vol. 48, no. 19, p. 3101, 2003.

[41] J. K. Seo, S. W. Kim, S. Kim, J. J. Liu, E. J. Woo, K. Jeon, and C.-O. Lee, "Local harmonic Bz algorithm with domain decomposition in MREIT: computer simulation study," *IEEE Transactions on medical imaging*, vol. 27, no. 12, pp. 1754–1761, 2008.

[42] J. K. Seo, K. Jeon, C.-O. Lee, and E. J. Woo, "Non-iterative harmonic Bz algorithm in MREIT," *Inverse problems*, vol. 27, no. 8, p. 085003, 2011.

[43] K. Jeon, H. J. Kim, C.-O. Lee, J. K. Seo, and E. J. Woo, "Integration of the denoising, inpainting and local harmonic Bz algorithm for MREIT imaging of intact animals," *Physics in Medicine & Biology*, vol. 55, no. 24, p. 7541, 2010.

[44] H. S. Nam and O. I. Kwon, "Axial anisotropic conductivity imaging based on projected current density in MREIT," *IEEE transactions on medical imaging*, vol. 29, no. 3, pp. 781–789, 2010.

[45] W. Ma, T. P. DeMonte, A. I. Nachman, N. M. Elsaid, and M. L. Joy, "Experimental implementation of a new method of imaging anisotropic electric conductivities," in *2013 35th Annual International Conference of the IEEE Engineering in Medicine and Biology Society (EMBC)*, pp. 6437–6440, IEEE, 2013.

[46] O. I. Kwon, W. C. Jeong, S. Z. Sajib, H. J. Kim, and E. J. Woo, "Anisotropic conductivity tensor imaging in MREIT using directional diffusion rate of water molecules," *Physics in Medicine & Biology*, vol. 59, no. 12, p. 2955, 2014.

[47] W. C. Jeong, S. Z. Sajib, N. Katoch, H. J. Kim, O. I. Kwon, and E. J. Woo, "Anisotropic conductivity tensor imaging of in vivo canine brain using DT-MREIT," *IEEE transactions on medical imaging*, vol. 36, no. 1, pp. 124–131, 2016.

[48] M. Chauhan, A. Indahlastari, A. K. Kasinadhuni, M. Schär, T. H. Mareci, and R. J. Sadleir, "Low-frequency conductivity tensor imaging of the human head in vivo using DT-MREIT: first study," *IEEE transactions on medical imaging*, vol. 37, no. 4, pp. 966–976, 2017.

[49] M. Sadighi, M. Şişman, B. C. Açıkgöz, H. H. Eroğlu, and B. M. Eyüboğlu, "Low-frequency conductivity tensor imaging with a single current injection using DT-MREIT," *Physics in Medicine & Biology*, vol. 66, no. 5, p. 055011, 2021.

[50] M. Sadighi, M. Şişman, and B. M. Eyüboğlu, "Multi-physics multi-contrast magnetic resonance imaging," in *ISMRM & SMRT Virtual Conference & Exhibition*, p. 1239, ISMRM, 2021.

[51] Y.-D. Zhang, S. Wang, G. Ji, and Z. Dong, "An improved quality guided phase unwrapping method and its applications to mri," *Progress In Electromagnetics Research*, vol. 145, pp. 273–286, 2014.

[52] K. T. Gillen, D. Douglass, and M. Hoch, "Self-diffusion in liquid water to- 31 c," *The Journal of Chemical Physics*, vol. 57, no. 12, pp. 5117–5119, 1972.

[53] K. R. Harris and L. A. Woolf, "Pressure and temperature dependence of the self diffusion coefficient of water and oxygen-18 water," *Journal of the Chemical Society, Faraday Transactions 1: Physical Chemistry in Condensed Phases*, vol. 76, pp. 377–385, 1980.

[54] K. S. Utz, V. Dimova, K. Oppenländer, and G. Kerkhoff, "Electrified minds: transcranial direct current stimulation (tDCS) and galvanic vestibular stimulation (GVS) as methods of non-invasive brain stimulation in neuropsychology—a review of current data and future implications," *Neuropsychologia*, vol. 48, no. 10, pp. 2789–2810, 2010.

[55] X. Liu, M. Tanaka, and M. Okutomi, "Noise level estimation using weak textured patches of a single noisy image," in *2012 19th IEEE International Conference on Image Processing*, pp. 665–668, IEEE, 2012.

[56] X. Liu, M. Tanaka, and M. Okutomi, "Single-image noise level estimation for blind denoising," *IEEE transactions on image processing*, vol. 22, no. 12, pp. 5226–5237, 2013.

[57] W. Rudin *et al.*, *Principles of mathematical analysis*, vol. 3. McGraw-hill New York, 1976.

[58] A. H. Poonawalla and X. J. Zhou, "Analytical error propagation in diffusion anisotropy calculations," *Journal of Magnetic Resonance Imaging: An Official Journal of the International Society for Magnetic Resonance in Medicine*, vol. 19, no. 4, pp. 489–498, 2004.

[59] K. Mardia, J. Kent, and J. Bibby, "Multivariate analysis," *Academic Press London*, vol. 15, p. 518, 1979.

[60] COMSOL Multiphysics® v. 5.1. www.comsol.com. COMSOL AB, Stockholm, Sweden.

[61] H. Eroğlu, B. Eyüboglu, and C. Göksu, "Design and implementation of a bipolar current source for MREIT applications," in *XIII Mediterranean Conference on Medical and Biological Engineering and Computing 2013*, pp. 161–164, Springer, 2014.

[62] K. Thangavel and E. Ü. Sarıtaş, "Aqueous paramagnetic solutions for MRI phantoms at 3 T: A detailed study on relaxivities," *Turkish Journal of Electrical Engineering & Computer Sciences*, vol. 25, no. 3, pp. 2108–2121, 2017.

[63] J. Latikka and H. Eskola, "The electrical conductivity of human cerebrospinal fluid in vivo," in *World Congress on Medical Physics and Biomedical Engineering 2018*, pp. 773–776, Springer, 2019.

[64] S. K. Piechnik, J. Evans, L. Bary, R. G. Wise, and P. Jezzard, "Functional changes in CSF volume estimated using measurement of water T2 relaxation," *Magnetic Resonance in Medicine: An Official Journal of the International Society for Magnetic Resonance in Medicine*, vol. 61, no. 3, pp. 579–586, 2009.

[65] C. Gabriel, A. Peyman, and E. H. Grant, "Electrical conductivity of tissue at frequencies below 1 MHz," *Physics in medicine & biology*, vol. 54, no. 16, p. 4863, 2009.

[66] D. P. Cistola and M. D. Robinson, "Compact NMR relaxometry of human blood and blood components," *TrAC Trends in Analytical Chemistry*, vol. 83, pp. 53–64, 2016.

[67] C. Göksu, K. Scheffler, P. Ehses, L. G. Hanson, and A. Thielscher, "Sensitivity analysis of magnetic field measurements for magnetic resonance electrical impedance tomography (MREIT)," *Magnetic resonance in medicine*, vol. 79, no. 2, pp. 748–760, 2018.

[68] M. Şişman, M. Sadighi, H. H. Eroğlu, and B. M. Eyüboğlu, "Experimental evaluation of spin echo based magnetic resonance magnetohydrodynamic flow velocimetry," in *ISMRM & SMRT Virtual Conference & Exhibition*, p. 1256, ISMRM, 2021.

[69] K. Gersten *et al.*, *Boundary-layer theory*. Springer, 2017.

[70] M. C. Potter, D. C. Wiggert, and B. H. Ramadan, *Mechanics of Fluids SI Version*. Nelson Education, 2012.

[71] R. De Luca, "Lorentz force on sodium and chlorine ions in a salt water solution flow under a transverse magnetic field," *European journal of physics*, vol. 30, no. 3, p. 459, 2009.

[72] K. Levenberg, “A method for the solution of certain non-linear problems in least squares,” *Quarterly of applied mathematics*, vol. 2, no. 2, pp. 164–168, 1944.

[73] J. P. Marques, F. F. Simonis, and A. G. Webb, “Low-field MRI: An MR physics perspective,” *Journal of magnetic resonance imaging*, vol. 49, no. 6, pp. 1528–1542, 2019.

[74] S. Vinitski, R. Griffey, M. Fuka, N. Matwiyoff, and R. Prost, “Effect of the sampling rate on magnetic resonance imaging,” *Magnetic resonance in medicine*, vol. 5, no. 3, pp. 278–285, 1987.

[75] M. Şişman, M. Sadighi, and B. M. Eyüboğlu, “Simultaneous magnetic resonance magnetohydrodynamic flow velocity and diffusion tensor imaging,” in *ISMRM & SMRT Virtual Conference & Exhibition*, p. 1257, ISMRM, 2021.

[76] P. B. Roemer, W. A. Edelstein, C. E. Hayes, S. P. Souza, and O. M. Mueller, “The NMR phased array,” *Magnetic resonance in medicine*, vol. 16, no. 2, pp. 192–225, 1990.

[77] B. Gruber, M. Froeling, T. Leiner, and D. W. Klomp, “RF coils: A practical guide for nonphysicists,” *Journal of magnetic resonance imaging*, vol. 48, no. 3, pp. 590–604, 2018.